SANDIA REPORT
SAND2023-10830
Printed October 2023

Sandia National Laboratories

MELCOR Accident Progression and Source Term Demonstration Calculations for a Sodium Fast Reactor (SFR)

Kenneth Wagner
Brad Beeny
David Luxat

Prepared by
Sandia National Laboratories
Albuquerque, New Mexico
87185 and Livermore,
California 94550

Issued by Sandia National Laboratories, operated for the United States Department of Energy by National Technology & Engineering Solutions of Sandia, LLC.

Available to DOE and DOE contractors from
U.S. Department of Energy
Office of Scientific and Technical Information
P.O. Box 62
Oak Ridge, TN 37831

Telephone: (865) 576-8401
Facsimile: (865) 576-5728
E-Mail: reports@osti.gov
Online ordering: http://www.osti.gov/scitech

Available to the public from
U.S. Department of Commerce
National Technical Information Service
5301 Shawnee Rd
Alexandria, VA 22312

Telephone: (800) 553-6847
Facsimile: (703) 605-6900
E-Mail: orders@ntis.gov
Online order: https://classic.ntis.gov/help/order-methods/

ABSTRACT

MELCOR is an integrated thermal hydraulics, accident progression, and source term code for reactor safety analysis that is being developed at Sandia National Laboratories for the United States Nuclear Regulatory Commission (NRC) since the early 1980s. Though MELCOR originated as a light water reactor (LWR) code, development and modernization efforts have expanded its application scope to include non-LWR concepts [1]. Current MELCOR development efforts include providing the NRC with the analytical capabilities to support regulatory readiness for licensing non-LWR technologies under Strategy 2 of the NRC's near-term Implementation Action Plans [2]. Beginning with the Next Generation Nuclear Project (NGNP), MELCOR has undergone multiple enhancements to provide analytical capabilities for modeling the spectrum of advanced non-LWR concepts [3]. This report describes the generic plant model developed to demonstrate the capabilities of MELCOR to perform sodium fast reactor (SFR) safety evaluations. The generic plant model is based on the Advanced Burner Test Reactor (ABTR) design by Argonne National Laboratory (ANL)[4]. The ABTR design was developed through the Global Nuclear Energy Partnership (GNEP) program as the first step to demonstrating transmutation technologies. The ABTR includes a large vessel that contains the primary to secondary heat exchanger. The molten sodium in the primary system is circulated using internal pumps. A sodium-to-sodium integral heat exchanger is located in the vessel that transfers heat to the secondary system. The reactor is surrounded by a guard vessel that contains any leaks from the vessel. The guard vessel connects to a steel dome above the reactor to form the containment boundary. MELCOR was used to perform example calculations to predict the plant response to an unprotected transient over-power (UTOP), an unprotected loss-of-flow (ULOF), and a blocked assembly.

ACKNOWLEDGEMENTS

This work was funded by the NRC as part of the development and demonstration activities defined in the NRC Non-Light Water Reactor Vision and Strategy Volume 3: Computer Code Development Plans for Severe Accident Progression, Source Term, and Consequence Analysis [5]. The authors gratefully acknowledge the contributions from Jason Schaperow, Shawn Campbell, and Hossein Esmaili of the US NRC for their valuable technical guidance. The authors thank Lindsay Gilkey for her detailed technical review and Mariah Smith for her support on editing and formatting.

Alex Shaw and Friederike Bostelmann of Oak Ridge National Laboratories (ORNL) performed the SFR SCALE analyses and provided the radionuclide decay heat power, radionuclide inventory, and the core axial and radial power profile for this analysis. Their analyses are documented in ORNL/TM-2022/2758 [6] and are part of the same NRC-sponsored effort.

CONTENTS

LIST OF FIGURES

LIST OF TABLES

ACRONYMS AND DEFINITIONS

Abbreviation	Definition
ABTR	Advanced Burn Test Reactor
ANL	Argonne National Laboratory
BOEC	Beginning of the equilibrium cycle
ASHRAE	American Society of Heating, Refrigerating and Air-Conditioning Engineers
CFD	Computational Fluid Dynamics
COR	Core
CsI	Cesium Iodine
CV	Control Volume
CVH	Control Volume Hydrodynamics
DCH	Decay Heat
DOE	United States Department of Energy
DRACS	Direct Reactor Auxiliary Cooling System
EBR-2	Experimental Breeder Reactor 2
FL	Flow Path
FLiBe	Li_2BeF_4
GNEP	Global Nuclear Energy Partnership
GRTR	Generalized Radionuclide Transport and Retention
HS	Heat Structure
iHX	Intermediate Heat Exchanger
LMTD	Log-Mean Temperature Difference
LWR	Light Water Reactor
NAC	Sodium Chemistry Model
Na-K	Sodium Potassium eutectic
NDHX	Natural Draft Heat Exchanger
NGNP	Next Generation Nuclear Project
NRC	United States Nuclear Regulatory Commission
ORNL	Oak Ridge National Laboratory
RN	Radionuclide
SFR	Sodium Fast Reactor
TRU	Transuranic
ULOF	Unprotected Loss-of-Flow
UTOP	Unprotected Transient Over-Power

This page left blank

1. INTRODUCTION

MELCOR is an integrated systems-level thermal hydraulics and source term code for reactor safety analysis [3]. It has been developed by Sandia National Laboratories for the United States Nuclear Regulatory Commission (NRC) since the early 1980s. Current MELCOR development efforts include providing the NRC with the accident analysis capabilities to support regulatory readiness for licensing non-light water reactor (non-LWR) technologies under Strategy 2 of the NRC's near-term Implementation Action Plans [1]. Beginning with the Department of Energy (DOE) Next Generation Nuclear Project (NGNP), MELCOR has undergone multiple enhancements to provide analytical capabilities for modeling the spectrum of advanced non-LWR concepts. A detailed description of the development process, including identification of technical gaps, is provided in NRC's "Non-Light Water Reactor (Non-LWR) Vision and Strategy, Volume 3 – Computer Code Development Plans for Severe Accident Progression, Source Term, and Consequence Analysis" (NRC ADAMS Accession No. ML20030A178) [5].

The scope of the source term demonstration project includes development and application of a MELCOR full-plant model using publicly available references and data. This report describes the generic plant model developed to demonstrate the capabilities of MELCOR to perform sodium fast reactor (SFR) safety evaluations. Previously, source term demonstration calculations were performed for other non-LWR designs (e.g., a heat pipe reactor), that are documented in separate reports [7][8][9][10].

MELCOR characterizes the evolution of an accident sequence from the early thermal-hydraulic response through the core heat up, including the release and transport of radionuclides from the primary system to the containment or confinement buildings and the environment. The code is a knowledge repository from decades of experiments and model development with a historical focus on LWR phenomenology. However, MELCOR has been extended with new models to address non-LWR technologies. The important MELCOR models for an SFR analysis are discussed in Section 2.

MELCOR relies on the SCALE code system to provide the radionuclide inventories, kinetics parameters, power distributions, and decay heat. SCALE is a multi-disciplinary tool developed by Oak Ridge National Laboratory (ORNL) for the NRC to combine nuclear system simulation tools into one cohesive package [11]. SCALE provides a comprehensive, verified and validated, user-friendly tool set for nuclear data, criticality safety, reactor physics, radiation shielding, radioactive source term characterization, activation, depletion and decay, and sensitivity and uncertainty analysis under a software quality assurance program. Since the 1970s, regulators, licensees, and research institutions around the world have used SCALE for safety analysis.

The MELCOR SFR input model used for the source term analysis is based on the Argonne National Laboratory (ANL) Advanced Burner Test Reactor (ABTR) [4]. The demonstration SFR input model development included (a) the MELCOR reactor vessel model, (b) the direct reactor auxiliary cooling system (DRACS), (c) incorporation of the SCALE inventory, axial and radial power profiles, decay heat tables, and reactivity feedback coefficients, (d) development of a containment based on the ABTR design information, and (e) plant control and radionuclide tracking algorithms. Section 3 describes the ABTR model used in the source term calculations.

The ABTR MELCOR plant model is used to simulate three types of accidents. The first is an unprotected transient over-power (UTOP) scenario, which is an inadvertent control assembly with

failure of the other safety control assembly to insert (i.e., the unprotected descriptor).[1] The second is an unprotected loss-of-flow (ULOF) scenario that simulates a trip of the primary and secondary system pumps. The UTOP and ULOF are identified in ABTR report as beyond design basis accidents. However, these sequences did not result in a radionuclide release. Consequently, a blocked flow assembly scenario was added, which did generate a radionuclide release. The accident progression and the source term results are described in Section 4. A summary is presented in Section 5.

This report describes the MELCOR ABTR full-plant deck and its application to the three accident scenarios. In addition, this work was presented at a public workshop on September 20, 2022. The video recording and presentation material are available at the following links:

- Video – https://www.youtube.com/watch?v=pinsryEwqC4
- Slides – https://www.nrc.gov/docs/ML2235/ML22353A109.pdf [12]

[1] Reference [4] terms the shutdown or control rods as a control assembly. To be consistent with the reference documentation, the unprotected accident is failure of the control assemblies to insert.

2. MELCOR SFR MODELING FEATURES

The MELCOR code is organized into "packages" that correspond to different groupings of reactor regions, physics, or other code functionalities [3]. The balance of the plant is modeled using the building block components of control volumes, heat structures, and flow paths. These basic components are used to represent the reactor vessel, the guard vessel and dome (i.e., the containment), and the secondary system, which will be described in Section 3. These fundamental modeling features are used for all reactor types. The level of modeling detail or discretization is user-specified based on the objectives of the analysis. An example for the SFR design [4] is described in Section 3 of this report.

In addition to the control volumes, heat structures, and flow paths, there are a few SFR-specific models. The following subsections describe some of the important MELCOR models used in the SFR demonstration calculations. Section 2.1 gives an overview of the SFR-specific models. Sections 2.2, 2.3, and 2.4 provide some additional details for the new SFR core model, the sodium equation of state, and the Generalized Radionuclide Transport and Retention (GRTR) model, respectively.

2.1. Overview of MELCOR SFR-specific models

Several new SFR-specific models were added to permit SFR accident analysis. First, MELCOR has been updated to support multiple fluids. For molten sodium fluid properties, the thermophysical properties were derived from the NACOM code [13]. The sodium fluid properties are used for the primary system and the secondary side. The ABTR design identifies sodium–potassium (NaK) as the Direct Reactor Auxiliary Cooling System (DRACS) secondary-side fluid, which was also modeled using sodium properties.

The ABTR core description and associated physics are modeled in MELCOR's "COR" package. Special models for SFR metal fuel modeling are superimposed in the reactor core portion of the vessel nodalization. The ABTR COR modeling includes representation of the fuel assemblies, the control assemblies, and the shield and reflector assemblies and their degradation.

A failure of the fuel cladding releases radionuclides to either sodium fluid or a gas space that formed around the fuel rods. The equilibrium radionuclide inventory in the ABTR fuel and the associated radionuclide decay heats are specified from the SCALE analysis. Any released radionuclides in the sodium fluid are tracked using the GRTR model, which is discussed in more detail in Section 2.4. The decay heat associated with the radionuclides is managed as groups of elements in radionuclide classes. The GRTR model is a subset of the MELCOR Radionuclide (RN) package, which manages the radionuclide transport and deposition physics. The Decay Heat (DCH) package provides the class-specific decay heat power to the RN package for every radionuclide in all locations.

MELCOR also includes a sodium chemistry model (NAC) for sodium spray and sodium pool fires as well as atmospheric chemistry. The NAC models are also based on the NACOM code. The NAC model has been used to model ex-vessel sodium leaks into the containment, primarily for comparisons to experiments [14][15]. The scope of the present calculations did not include an ex-vessel sodium spray or pool fire.

2.2. Sodium core model

MELCOR uses the COR package to model the SFR metal fuel behavior. The new COR model for the SFR calculates the thermal response of (a) the fuel rods in the core, (b) the control, reflector, and shield assemblies, (c) the core supporting structures, (d) the lower plenum internal structures, and (d) the vessel lower head below the core. The COR package also models the relocation of the core and supporting structures during melting, slumping, and formation of molten pool and debris,

including failure of the reactor vessel and ejection of debris into the reactor cavity. The COR package transfers energy to and from the surrounding liquid and vapor sodium and boundary structures, which are modeled by the Control Volume Hydrodynamics (CVH) package and the Heat Structure (HS) package, respectively. The physical models in the SFR COR package include the nodalization scheme and calculational framework of the package, the heat transfer models, the mass relocation models, and the lower head thermomechanical model.

The migration of fission product gases is tracked within the fuel, the sodium bond gap, and the fuel pin gas plenum, which is where the initial radionuclide inventory is assigned. Within the fuel, the fission gas is split between open and closed porosity locations. During the transient calculation, fission gas contained in the closed porosity area can migrate/coalesce into areas of open porosity, which is assumed to be in pressure equilibrium with the pin gas plenum. As fuel heats up, molten cavities can form and fission gas from both open and closed porosity locations can be subsumed by molten cavity. The fuel cladding failure is based on a thinning criterion where cladding is assumed to lose strength and collapse below some minimum thickness. The loss of clad thickness is primarily due to melting and candling as the fuel and clad overheat. Radionuclides release from the fuel leverages existing LWR gap and diffusion-based models following the cladding failure. A simplified schematic of the modeling is shown in Figure 2-1.

The melting temperature of the ABTR fuel is lower than the fuel cladding. During fuel heat-up and degradation, the fuel slug melts but is contained within an intact steel cladding. Next, the pressure boundary of the steel cladding fails when the cladding reaches its gap release temperature. The gap release corresponds to the release of both the sodium bond gap and pin plenum radionuclide inventories from the fuel pin. As the temperature rises further, the steel cladding begins to melt and subsequently candle and refreeze as conglomerate debris on the intact clad structure below. Clad melting thins the clad component thickness at the melt site and causes collapse once a minimum thickness threshold is crossed. Alternatively, the clad could also collapse when a threshold temperature is reached. In either case, when the cladding fails:

- the failed region of the cladding is transformed into debris and allowed to collapse,
- the fuel adjacent to the failed cladding is likewise transformed into molten and solid debris,
- radionuclides in the sodium bond gap and the pin gas plenum are released if they have not already been released according to a gap radionuclide release temperature criterion,
- radionuclides in open porosity of fuel at collapse are immediately released, and
- radionuclides in closed porosity of fuel at collapse have a delayed, diffusion-based release.

The debris formed by the failed cladding and fuel is tracked separately. The solid (i.e., non-molten) fuel and cladding debris collects in the location where the fuel rods previously existed but is supported by any intact fuel rod stubs below the failed location. Any molten relocating (candling) materials can freeze in cooler locations in the fuel assembly, which can create bridges across intact portions of the fuel rod to form flow blockages. Similar to MELCOR's LWR models, the molten and particulate debris above the blockage are supported. Debris is also supported by core support structures. The failure of the support structures is handled like the LWR model with options for alternate thermal-mechanical failure models. The SFR COR model also includes the vessel lower head structure. If the debris relocates to the lower head, then the vessel lower head could heat to fail and leak core debris to the guard vessel.

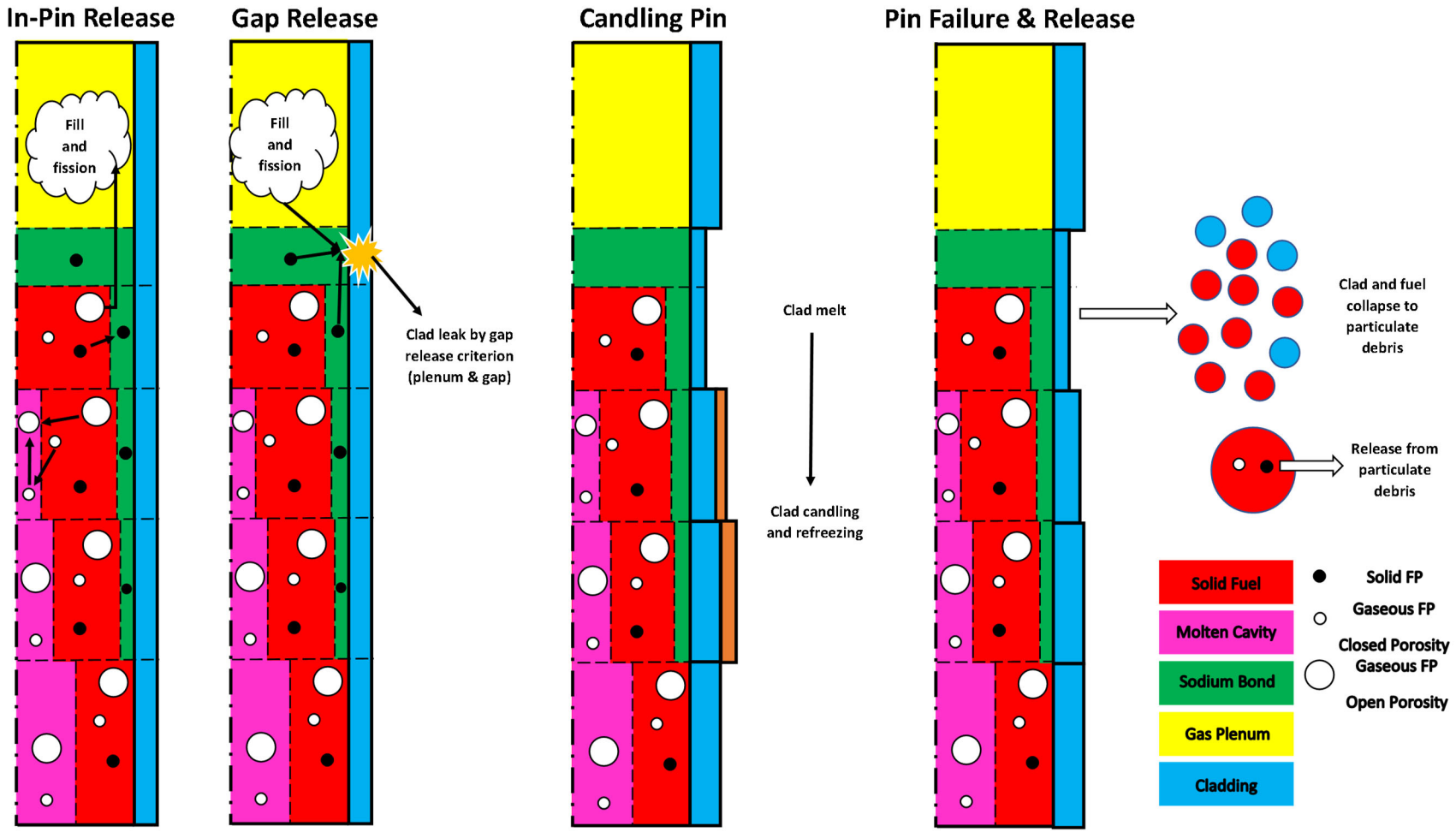

Figure 2-1 MELCOR SFR schematic porosity and radionuclide evolution.

2.3. MELCOR sodium equation of state

The SFR uses molten sodium as the primary and secondary fluid. For the demonstration calculation, the sodium thermophysical properties are also used for the NaK in the secondary loop of the DRACS. The sodium equation of state was obtained from the NACOM code [13] When simulating a SFR reactor, special input directives are used to identify sodium as primary fluid rather than water. MELCOR reads the sodium fluid properties database, which provides the specific volume (m^3/kg), the specific internal energy (J/kg), the specific heat capacity at constant pressure (J/kg-K), and the specific entropy (J/kg-K). The coefficient of thermal expansion (1/K) and isothermal compressibility (1/Pa) are also determined using these properties.

A key enhancement implemented in previous fluoride high-temperature reactor demonstration calculations was an equation of state extrapolation for frozen conditions [7], which is also active in SFR applications. Sodium solidifies at approximately 98°C. During the evolution of a transient, the temperature may reach the freezing point. To allow frozen conditions without significant architectural changes, a thermodynamic supercooling model was added to the equation of state, such that the liquid and vapor phases may exist below the freezing temperature. When the new modeling option is active by the user, the thermodynamic properties are extrapolated whenever the fluid drops below the freezing temperature.[2] The pressure is exponentially extrapolated as a function of temperature from the freezing values defined by the equation of state down to temperatures as low as 0°C . Internal energy is linearly extrapolated as a function of temperature from the freezing values, which is consistent with a constant specific heat model. The entropy is linearly extrapolated as a function of the natural logarithm of the temperature from the freezing values to 0°C, which is consistent with an incompressible substance model. The new extrapolations along with MELCOR's thermodynamic variables of density and temperature permit the calculation of all other needed values and derivatives to affect a solution.

2.4. MELCOR GRTR model

The MELCOR GRTR model is being developed for increased flexibility in modeling liquid field radionuclide behavior.[3] GRTR is a sub-model that is being integrated into the RN package. It adds capabilities to assess radionuclide behaviors such as solubility, soluble and insoluble (i.e., colloid) transport, deposition, and vaporization. Although the GRTR models were originally conceived for molten salt systems, GRTR is being updated with additional flexibility to model any reactor type, including SFRs. GRTR is being modified to calculate the radionuclide solubility using Antoine vapor pressure curves that can be varied based on the reactor design. The updated GRTR structure replaces the original molten salt models to allow application-specific specification of relevant physics and interactions.

Figure 2-2 shows the GRTR functions, which includes the physio-chemical dynamic models and the transport models. GRTR receives the mass of radionuclides entering the fluid from the fuel or the gas space by the COR and RN packages, respectively. The radionuclides in GRTR are tracked as soluble forms, insoluble forms (i.e., colloids), or non-condensable gases that advect with the liquid fluid between control volumes. The physio-chemical models include vaporization, mass transfer between soluble and insoluble forms, and deposition onto structures. The transfer between soluble

[2] The thermodynamic property routines would fail, which stopped the calculation prior to this modeling enhancement.

[3] The GRTR will eventually include capabilities for special physics in the vapor field.

and vapor forms is specified using solubility curves with an optional time-constant for dissolution. The colloid deposition onto structures includes the absorption of soluble radionuclides into porous structures (e.g., graphite in molten salt non-LWR reactor systems) and the colloid deposition onto any surface. GRTR is intended to be applicable for all reactor types with user flexibility on the number of forms and interacting physics (see Figure 2-3 as a detailed example for an MSR).

As noted above, the GRTR model was still under development at the time of the demonstration calculations. While the model structure is nearly complete, the review of the sodium thermochemical databases and example input structures for important physics has not been completed. Future work will incorporate available SFR thermochemical data into the GRTR model as appropriate. The simplest application of the GRTR model is to allow non-condensable gases to rise and exit at any fluid surface, which was used in these demonstration calculations. In the blocked assembly demonstration calculation, released noble gases migrate through the hot sodium pool to the argon blanket at the top of the reactor. Future applications will include the behavior of other released radionuclides.

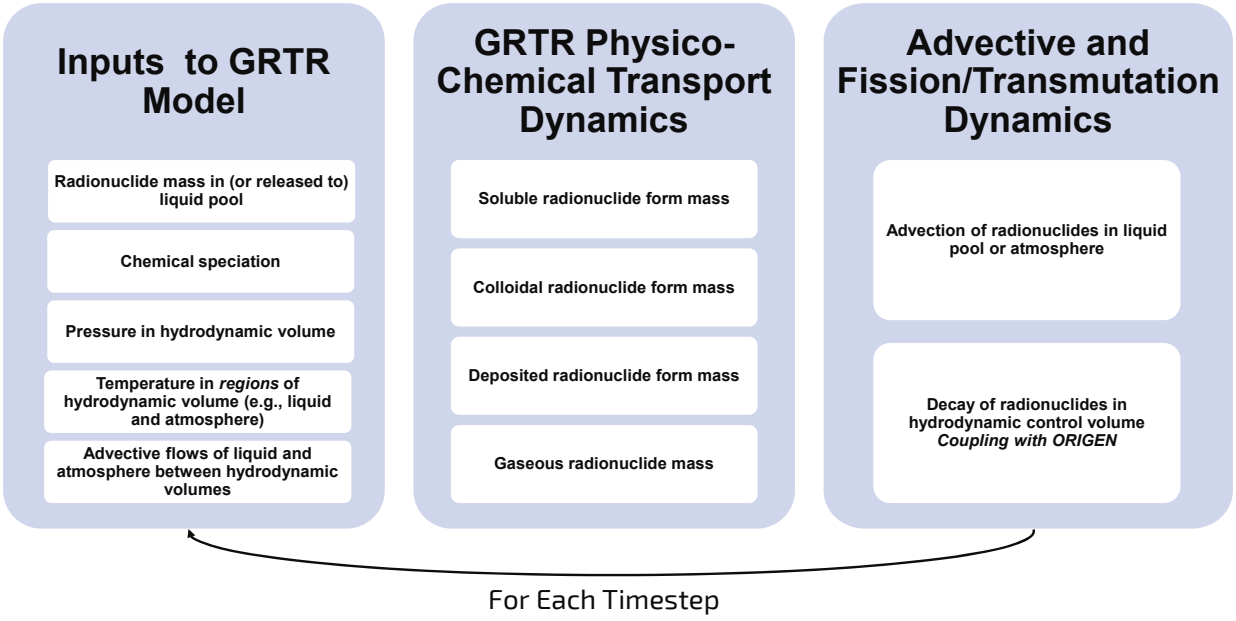

Figure 2-2 MELCOR GRTR inputs, models, and transport.

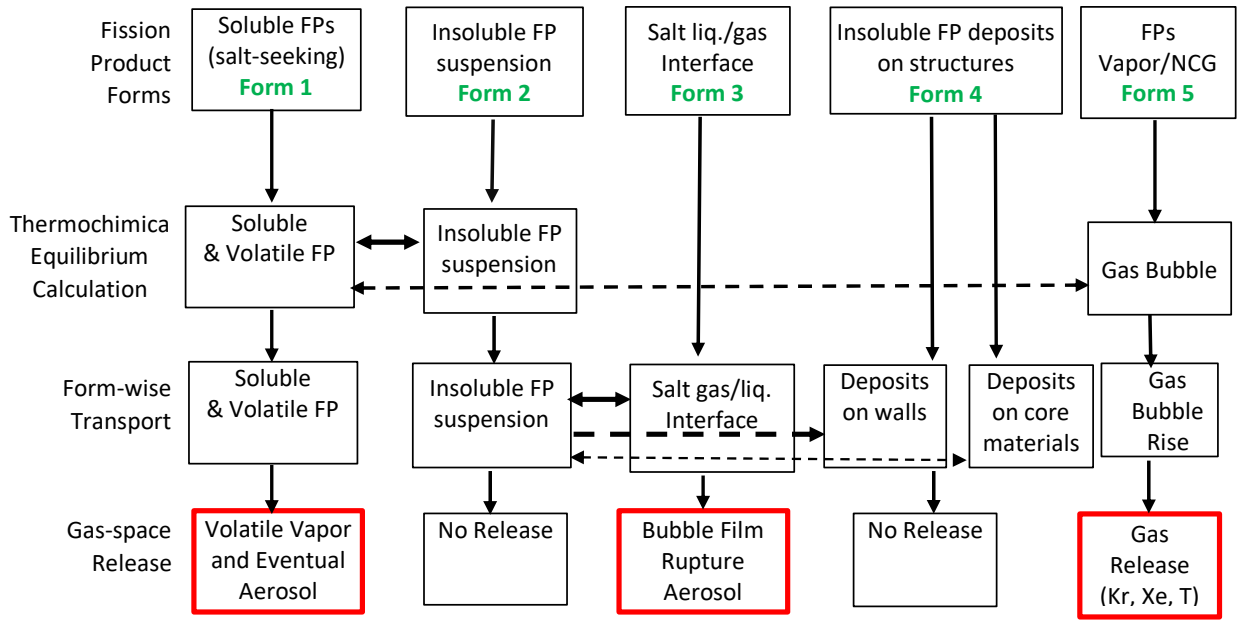

Figure 2-3 Example of a GRTR application for a molten salt system.[4]

[4] GRTR allows specification of the number of forms and their interactions. The example in Figure 2-3 was developed for a molten salt reactor. The horizontal arrows correspond to mass transfer processes between forms. . Masses of released species are given in the bottom row in red-bounded boxes.

3. MODEL DESCRIPTION

The development of the MELCOR SFR input model was based on the ABTR design report [4]. In particular, Reference [4] included a safety analysis section with some fundamental geometry of the ABTR and example SAS4A computer code calculations. Most of the information provided in the SAS4A section of Reference [4] could not be directly obtained from other sections of the report. Consequently, the SAS4A input was selected as the primary data source. However, the information in the SAS4A analysis section was conflicting or confusing with design information from the earlier sections in Reference [4]. Some of the differences in the SAS4A input descriptions versus other system description sections in Reference [4] may be attributed to an earlier or possibly later design description relative to the design input used for the SAS4A analysis.

The data presented in the ABTR design report [4] are incomplete for developing a highly accurate model. Attempts to confirm confusing or conflicting data with a ruler were not successful due to the unavailability of scaled drawings. Nevertheless, the available information with some assumptions was sufficient to develop a preliminary SFR demonstration model. These challenges are similar to those encountered for other demonstration non-LWR model development efforts.[5] Some assumptions were required to model the core inlet structure, the fuel inlet nosepiece and exit nozzle geometry and masses, the metal redan structure that separates the hot sodium in the core outlet region in the center of the vessel from the cooler sodium on the outer portion of the vessel, the geometry around the fuel storage racks, and locations of key vessel components. There were also assumptions about the lower containment geometry and the upper containment argon blanket system.

The radionuclide inventory and decay heat tables were obtained from a supporting SCALE analysis by ORNL [6]. SCALE was also used to generate the axial and radial power profiles and the reactivity feedbacks. Due to the small size of the reactor, the power profile from each assembly was calculated, which is not possible with large reactors due to the large number of assemblies For application in the MELCOR ABTR model, the assemblies were grouped by their power.

The remainder of Section 3 describes the MELCOR model of the ABTR. Section 3.1 provides an overview of the ABTR reactor design. Following the ABTR overview, the reactor vessel, the primary and secondary systems, and the containment building nodalizations are described in Section 3.2. As mentioned earlier, SCALE provided the radionuclide inventory and the decay heat, which is described in Section 3.3. The radionuclide release modeling is described in Section 3.4. The SCALE analysis also provided reactivity feedbacks for the point kinetics model, which are described in Section 3.5. Finally, the steady state initialization is shown in Section 3.6. Due to its importance for passive heat removal and its complexity, the DRACS example results are discussed in Section 3.7.

3.1. SFR Overview

The ABTR design specifications were developed as part of a Global Nuclear Energy Partnership (GNEP) program at ANL in 2006. The objective of GNEP was to develop a comprehensive strategy to increase the United States' global energy security, encourage clean energy development around the world, reduce the risk of nuclear proliferation, and improve the environment [4]. The ABTR design was built off of ANL's long history with SFRs including the Experimental Breeder

[5] The most complete information was obtained for the MELCOR input model describing the molten salt reactor experiment, which was actually built and operated. The other non-LWRs were design studies that were constrained by resources and the scope of the presented information.

Reactor 2 (EBR-2). The primary mission of the GNEP ABTR program was to demonstrate the transmutation of transuranics recovered from spent LWR fuel. The transmutation is facilitated using a fast neutron spectrum reactor, which is required to efficiently fission transuranics to eliminate their long-term toxicity and decay heat [4].

A schematic of the ABTR is shown in Figure 3-1. The ABTR uses three loops to remove heat from the core. The primary loop with the electromechanical pumps circulates the sodium in the vessel through the core and the shell side of the two intermediate heat exchangers (iHXs). The secondary or intermediate loop circulates sodium through the tube side of the iHX to the tube side of the sodium to CO_2 heat exchanger. The tertiary loop circulates CO_2 to the turbine. The primary shutdown heat removal connects to the tube side of the sodium to CO_2 heat exchanger but was assumed unavailable in the demonstration calculations and not modeled. Some of the key ABTR design parameters are summarized in Table 3-1.

The ABTR reactor vessel nodalization was developed using the geometry and technical information in Reference [4]. The reactor vessel is 16 m high with a diameter of 5.8 m. The primary system is completely contained within the reactor vessel, which is also surrounded by a guard vessel in the containment. The reactor thermal power is 250 MW, and the turbine generates 95 MW. The key features in the vessel include the core, 2 electromechanical pumps, 2 iHXs, a metal structure called a redan that separates the hot sodium in the core outlet region in the center of the vessel from the cooler sodium on the outer portion of the vessel.

The core is formed by 199 hexagonal assemblies as shown in Figure 3-2. The fuel is located in the 24 inner core and 30 outer core fuel assemblies. Interspersed in the inner core are 6 test assemblies, 3 secondary control and 7 primary control assemblies for reactor shutdown and control, respectively, and 3 material test assemblies. The outer core is surrounded by 78 reflector assemblies that contain 91 HT-9 stainless steel rods. Finally, 46 shield assemblies are located on the outer ring that have 19 HT-9 pins filled with B4C pellets.

The 24 inner core and 30 outer core fuel assemblies are surrounded by a HT-9 stainless steel hexagonal duct. There are 217 fuel rods in the assembly duct. The 328 cm long assembly duct includes a 38 cm inlet nozzle and a 30 cm handling socket at the outlet. The gap between adjacent assemblies is 4 mm.

The fuel slugs are a ternary metal alloy of U-TRU-Zr fuel, where the transuranic (TRU) isotopic composition is determined from a mixture of 10-year cooled LWR spent fuel with a 33 MWd/kg burnup and weapons-grade plutonium. The inner and outer core zones have fuel enrichments (i.e., TRU fractions) of 16.5% and 20.7%, respectively. The 260 cm fuel pins include a 60 cm inlet shield structure (HT-9 stainless steel), an 80 cm fuel slug, and a 120 cm gas plenum. The fuel slugs use a sodium bond between the fuel and the HT-9 cladding to enhance heat transfer. The fuel pins are helically wrapped with a wire to maintain the pin spacing (see Figure 3-3). The HT-9 fuel pin cladding outer diameter is 0.8 cm with a thickness of 0.052 cm. The fuel slug outer diameter is 0.603 cm.

Two electromagnetic or four mechanical pumps in the vessel (i.e., both options are described) circulate 1256 kg/s of sodium from the cold pool after the outlet of the iHX to the core inlet structure. The SAS4A analysis used two electromagnet pumps, which also used in the MELCOR model. The sodium flows into the 199 hexagonal core assemblies and the 250 MW core raises the sodium temperature from 355°C at the core inlet to 510°C at the core outlet. There are openings in the redan above the core exit that allows the heated sodium to enter the shell side of the two iHXs. The flow exits the bottom of the iHXs into the cold pool region formed between the redan wall and

the vessel wall. The sodium level in the cold pool region is different than the hot region due to the pressure drop through the iHXs. Figure 3-4 shows the ABTR reactor vessel including the iHXs. The iHXs are located inside of the redan structure, which is shown Figure 3-5.

The gas space at the top of the hot and cold pools in the vessel is an argon gas blanket. The argon filtration system is not described in the ABTR reference document [4]. For the demonstration calculation, a filtration pipe that exits the top of the vessel into the reactor dome is assumed to fail coincidentally with accident initiation (i.e., it could also be a leak from the top of the reactor).

The secondary side of the ABTR receives heat from the tube-side of the iHXs. The sodium of the secondary side of the iHX, or the intermediate sodium loop, connects to a heat exchanger outside the vessel that transfers heat to a CO_2 Brayton cycle with a turbine. The CO_2 loop was not modeled for the demonstration calculations.

Reference [4] includes a description of the ABTR containment. The two important features are the guard vessel that surrounds the vessel and the containment dome. The argon inerted guard vessel is a low volume structure that will contain any sodium leaks from the reactor vessel. A spill from the reactor into the low volume guard vessel does not allow an uncovery of the fuel (i.e., see Figure 3-4 for the faulted level in the reactor vessel after equilibration with the spill into the guard vessel). The guard vessel is located in the containment reactor cavity. A forced air flow cools the outer surface of the guard vessel and provides a thermal barrier to limit concrete heating (see Figure 3-4). Above the reactor vessel is the containment dome (see Figure 3-6) that contains the refueling equipment. The reactor building is a low-leakage structure (0.1% volume/day) with a design gauge pressure of 170 kPa (10 psig).

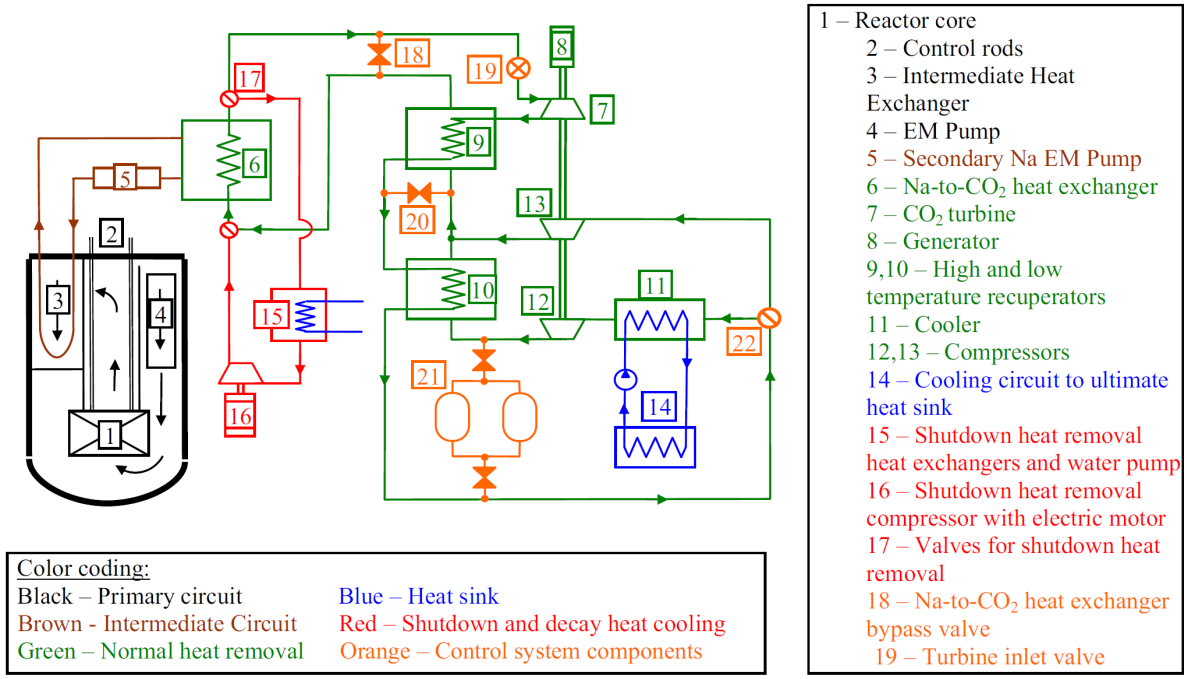

Figure 3-1 ABTR schematic [4].

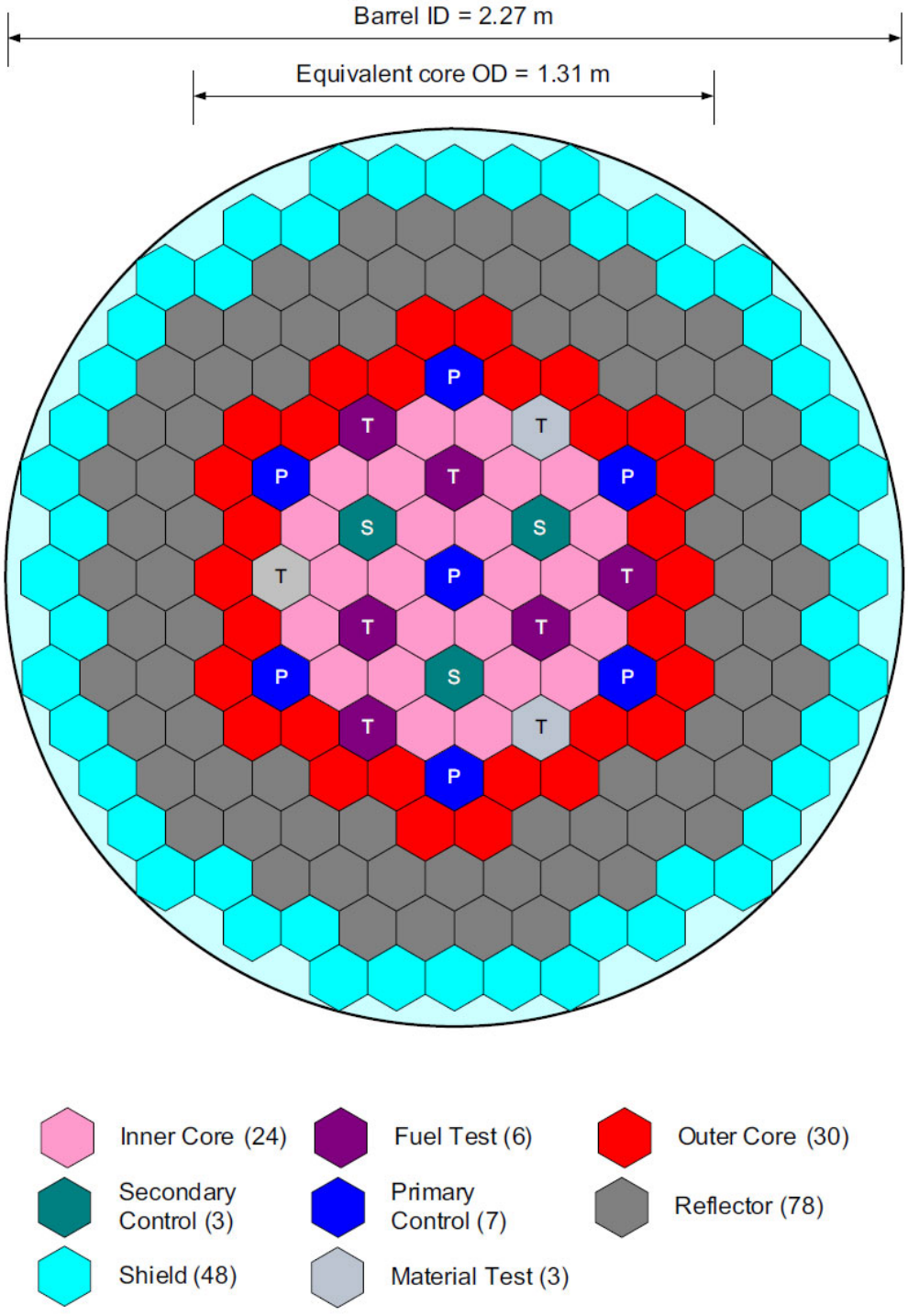

Figure 3-2 ABTR reactor core assemblies [4].

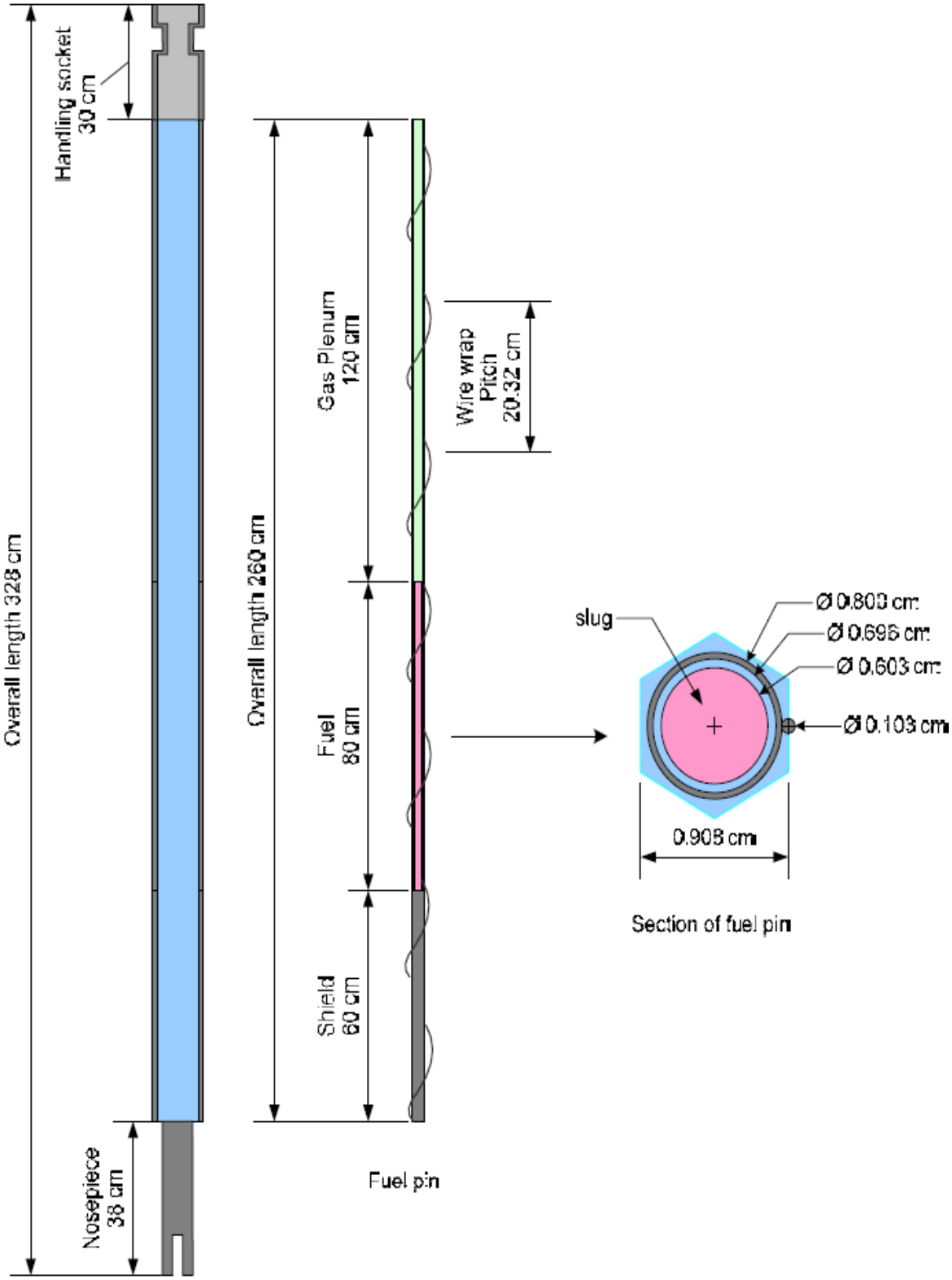

Figure 3-3 ABTR fuel assembly and fuel pin dimensions [4].

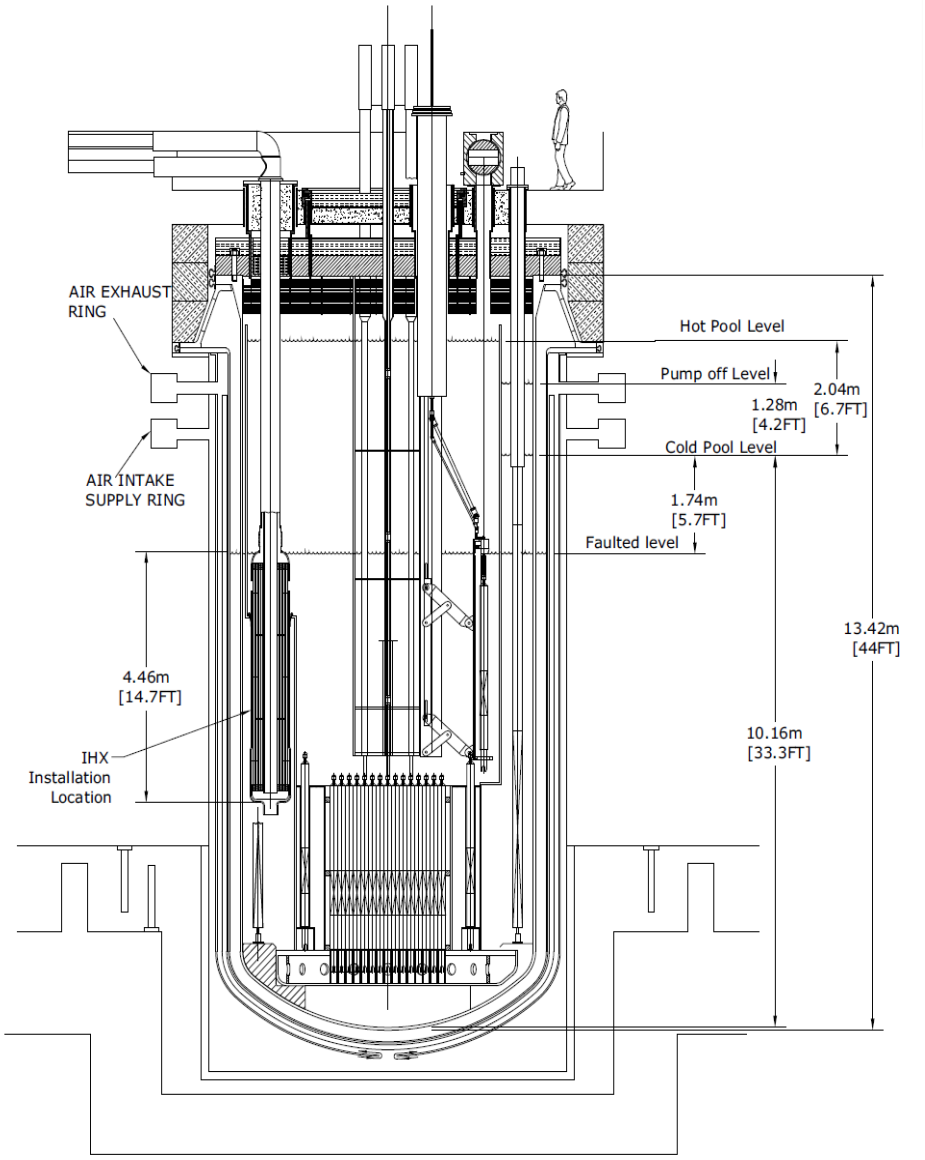

Figure 3-4 ABTR reactor vessel [4].

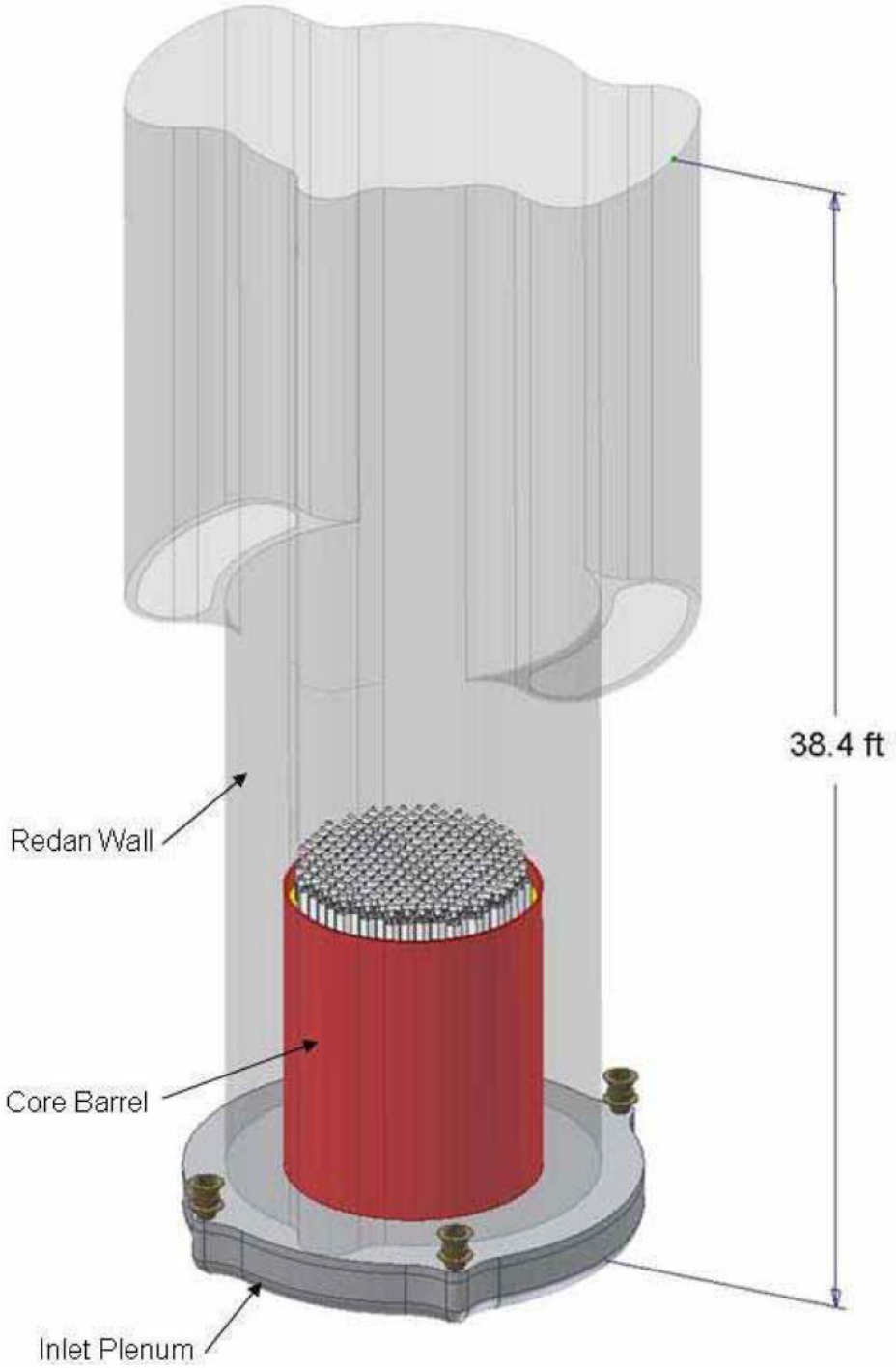

Figure 3-5 ABTR vessel redan structure [4].

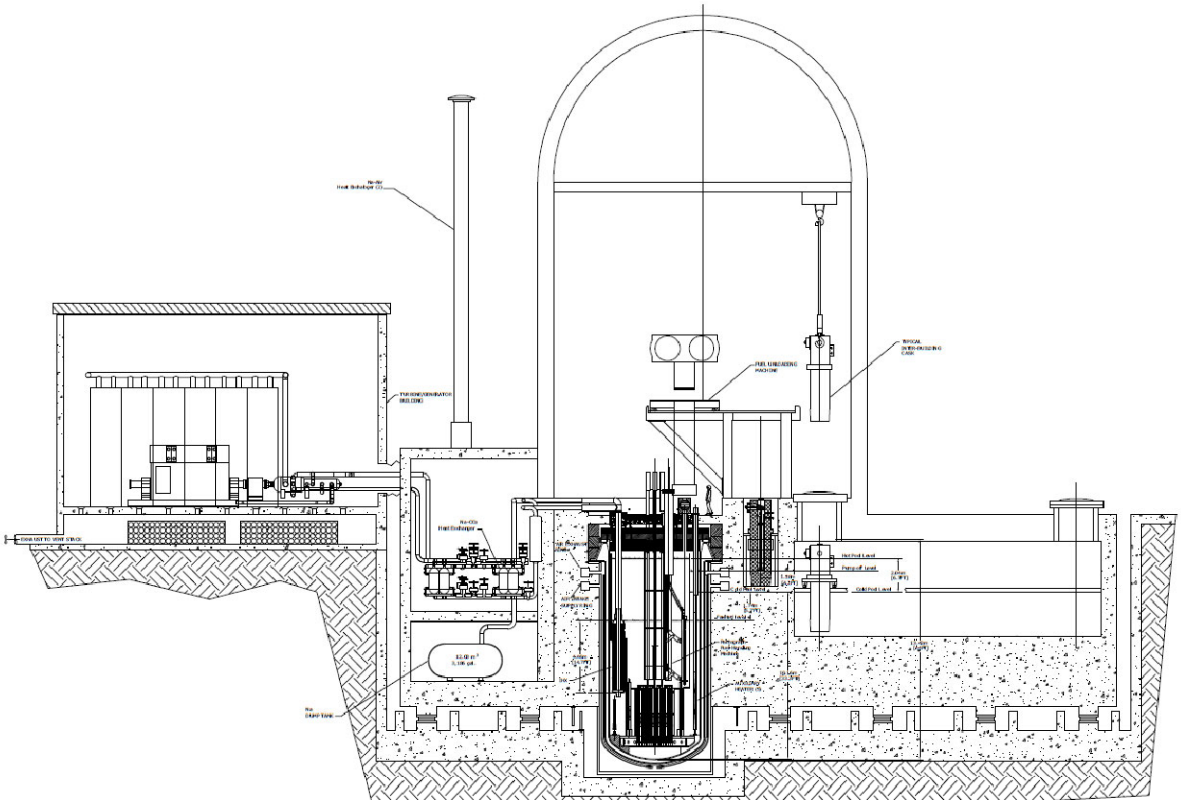

Figure 3-6 ABTR containment and surrounding reactor building [4].

Table 3-1 Key ABTR design parameters [4].

Parameter	Value
Reactor thermal power	250 MW
Coolant	Sodium
Driver fuel	Metal (~20% TRU, 80% U)
Power density	$258x10^3$ kW/liter
Reactor vessel pressure	Near atmospheric, 1.358 bar#
Core inlet temperature	355 °C
Core outlet temperature	510 °C
Primary pump	2 electromagnetic pumps 22.1 m^3 per pump
Thermal efficiency	38%
Secondary iHX inlet	333 °C
Secondary iHX outlet	488 °C

Notes:
#Assumed to be 1.357 bar (5 psig)

3.2. ABTR model nodalization

The ABTR model nodalization and key modeling features for the reactor vessel, the primary and secondary systems, and the containment are described in Sections 3.2.1 through 3.2.3, respectively.

3.2.1. Reactor vessel nodalization

The ABTR reactor vessel nodalization in MELCOR utilizes building block inputs from multiple packages. The building block approach to the input allows for the flexibility of modeling alternate reactor designs with varying levels of resolution. The reactor core is the key region in the vessel, which is composed of 199 hexagonal assemblies. The ABTR core is specified using control volumes, flow paths, heat structures, and COR package components. The COR package point kinetics model provides the fission power to the core.

The COR package fuel and structural models span the reactor core and the lower portion of the vessel. The COR package nodalization with the control volume and flow path nodalization is shown in Figure 3-7. The ABTR core nodalization has 15 axial levels and 8 radial rings. COR axial level 1 (i.e., axial levels are shown with the horizontal blue lines) is the lower spherical head of the ABTR vessel. CV-110 models the lower head region. The lower head region is hydraulicly connected to the rest of the cold pool but relatively stagnant. COR Package axial level 2 contains the core inlet plenum. The inlet plenum is modeled with CV-100. The two electromagnetic pumps discharge into inlet plenum region, which are shown in in Figure 3-7. The core inlet plenum only connects to the two pumps and the fuel assemblies and does not connect to the lower head region. The connecting flow paths the fuel assemblies are shown with arrows.

The inlet and reflector region of the fuel assemblies (see Figure 3-3) are located at COR axial level 3. The bottom of the fuel assemblies includes a HT-9 steel reflector. COR package axial levels 4 through 13 are the active fuel region. COR package rings 1 through 6 (i.e., radial rings are shown with vertical blue lines in Figure 3-7) contain the 60 inner and outer core fueled assemblies. Ring 7 contains the 10 control and 3 material test assemblies. Ring 8 holds the 78 reflector and 58 shield assemblies. The active fuel region of the fueled assemblies has 5 control volumes per ring (i.e., rings 1 through 6) with two COR axial cells per control volume. The unpowered assemblies in rings 7 and 8 are modeled with a single control volume. Finally, the fuel assembly outlet region is in COR axial level 15, which includes the fuel pin gas plenum and the handling socket (see Figure 3-3).

The ring-to-ring subdivision of the fuel assemblies is guided by the SCALE analysis of the ABTR. Figure 3-8 shows the ABTR core at the top of the figure. The SCALE nodalization of the active fuel region inside of the outer shield and reflector assemblies is shown in the middle. The SCALE individual assembly power results were subdivided into 5 groups, which are color-coded in Figure 3-8. For example, the 6 highest-power assemblies are shown in the center of the core with pink circles and have an average radial power factor of 1.27. The locations without circles are material or control test assemblies. SCALE radial zones 1 through 4 directly correspond to MELCOR rings 6 through 3, respectively.[6] The MELCOR radial nodalization splits the highest-powered assemblies (i.e., SCALE zone 5) into COR rings 1 and 2. The MELCOR subdivision of 2 rings was made to allow a single blocked fuel assembly. Ring 1 has one of the highest-powered

[6] It is normal but not required convention in MELCOR models to assign successively higher ring numbers to lower powered regions. SCALE radial zone 1 is the lowest-powered assemblies (i.e., a radial power factor of 0.8), which is assigned to MELCOR Ring 6.

assemblies and Ring 2 has the remaining 5 assemblies. The radial power factor in MELCOR rings 1 and 2 is the same.

The MELCOR nodalization of the remainder of the vessel is shown in Figure 3-9. The redan (see Figure 3-5) separates the hot pool region after the core outlet from the cold region after the iHXs. The hot pool is separated into 3 control volumes (CV-150, CV-160, and CV-170). The fluid exiting the core must rise to CV-170 before reaching the opening in the redan to the two iHXs. The lowest hot pool region (CV-150) is between the core barrel and the lower redan structure. The normal full power with the pumps operating hot and cold pool sodium levels are below the top of the redan. The top of the hot and cold pools in the vessel (i.e., CV-140 and CV-170) are inerted with an argon gas blanket.

The two iHXs are modeled separately (CV-181 and CV-182). The cold pool includes 4 control volumes (CV-110, CV-120, CV-130, and CV-140). The two iHXs discharges into CV-120. The two electromagnetic pumps and their discharge headers are modeled in CV-190, which takes suction from CV-130 (i.e., the control volume above the iHX discharge). Consequently, the fluid exiting the iHXs must flow upwards to the electromagnetic pump inlet before flowing to the core inlet plenum (CV-100).

The intermediate sodium loop provides the correct boundary conditions for normal operations but is isolated in the demonstration sequences or its performance is parametrically varied. It includes a specified temperature control volume (CV-400) for the secondary tube-side iHX inlet temperature (see Figure 3-10). CV-400 connects to CV-410 and CV-415, which models the secondary fluid in the tubes for the two iHXs. CV-410 and CV-415 connect to CV-181 and CV-182, respectively. The tubes discharge into a specified-pressure control volume (CV-420).

The heat transfer from the primary fluid on the shell-side of the iHX to the tube-side of the intermediate loop is based on a log-mean temperature difference calculation with an effective primary-side to intermediate heat transfer coefficient. The effective heat transfer coefficient in the complex counter-current iHX heat exchanger is evaluated during the steady state using a proportional-integral controller that is tuned to give the rated response. Prior to the transient, the effective heat transfer coefficient is frozen and assumed to be constant for the transient. However, the heat transfer to the secondary varies based on the log-mean temperature difference of the fluids entering and exiting the iHXs as follows,

$$Q = UA\ x\ LMTD$$

$$LMTD = (\Delta T_A - \Delta T_B)/(\ln(\frac{\Delta T_A}{\Delta T_B})$$

where,

Q	Heat transfer rate from the primary to the intermediate loop (W)
U	Effective heat transfer coefficient determined at steady state (W/m^2-K)
A	Intermediate-side tube surface area (m^2)
LMTD	Log-mean temperature difference (K)
ΔT_A	(Primary-side iHX inlet temperature) – (Intermediate-side iHX outlet temperature) (K)
ΔT_B	(Primary-side iHX outlet temperature) – (Intermediate-side iHX inlet temperature) (K)

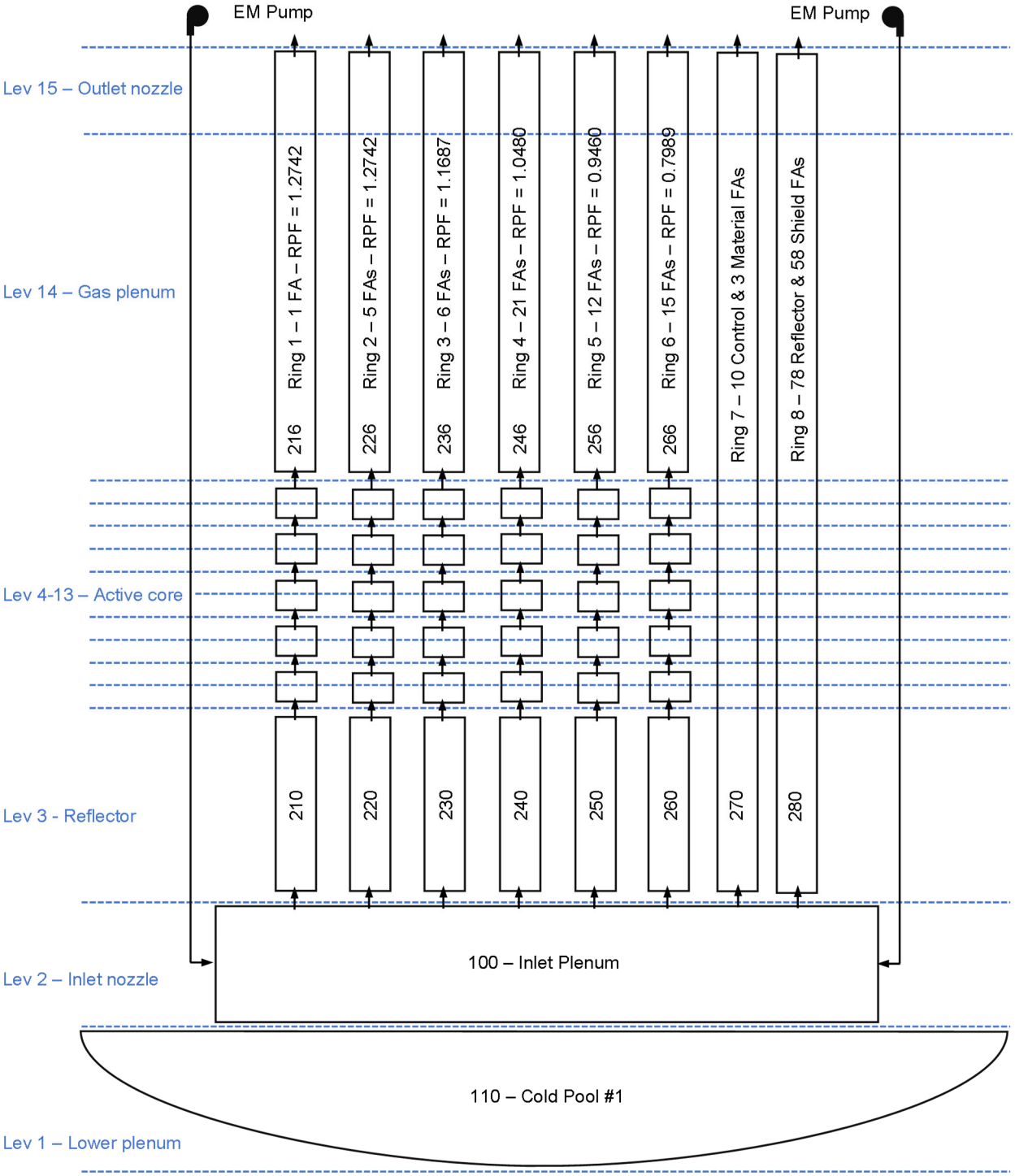

Figure 3-7 ABTR reactor core and lower vessel nodalization.

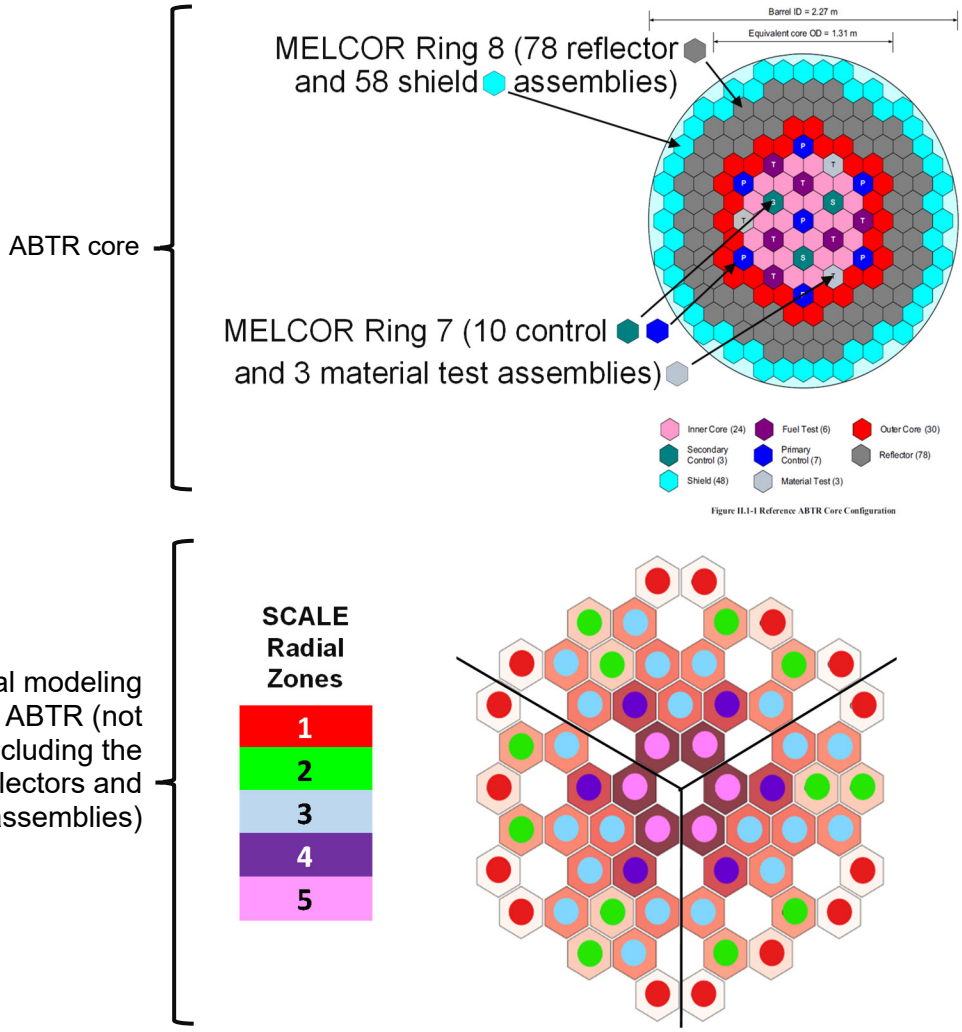

MELCOR radial mapping to SCALE

ORNL Radial Zone (r)	1	2	3	4	5	
MELCOR Radial Zone (r)	6	5	4	3	2	1
Number of Assemblies	15	12	21	6	5	1
Assembly Power Factor	0.80	0.95	1.05	1.17	1.27	

Figure 3-8 Mapping from the active fuel regions from SCALE to MELCOR.

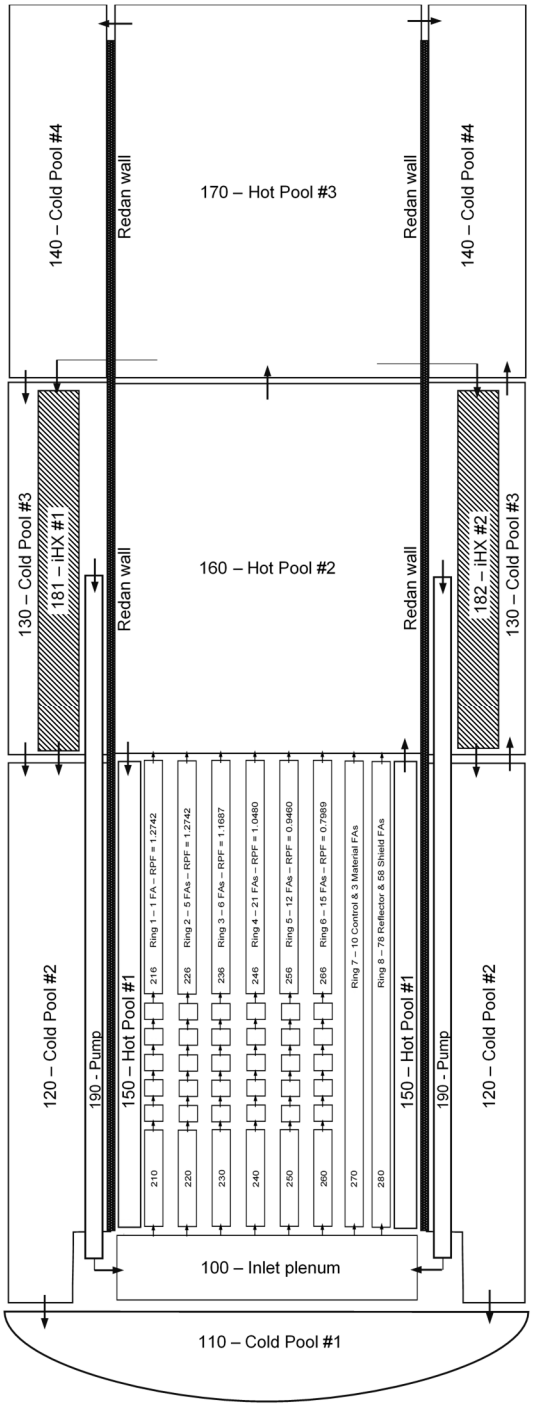

Figure 3-9 MELCOR ABTR reactor vessel nodalization.

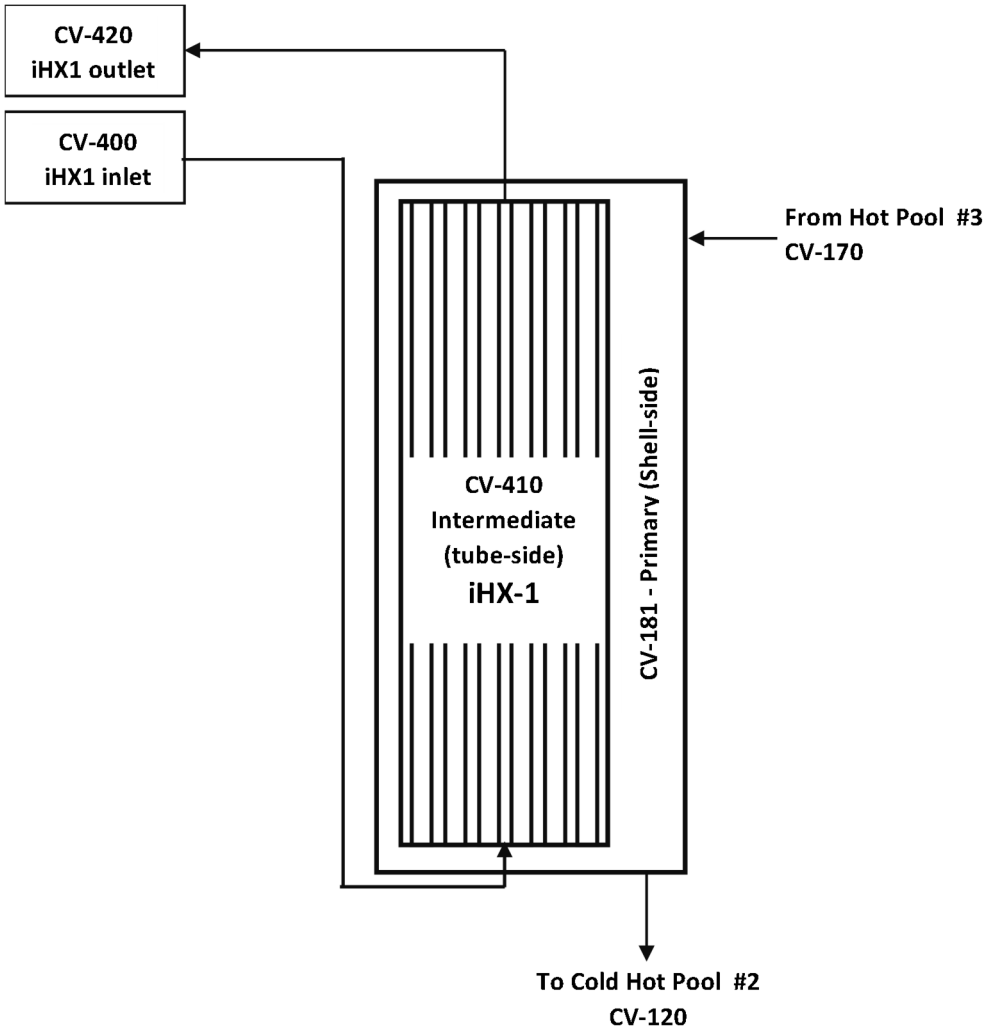

Figure 3-10 MELCOR ABTR iHX nodalization (example of iHX1 side).

3.2.2. Direct reactor auxiliary cooling system (DRACS)

The DRACS is the ABTR passive or active heat removal system. If heat removal through the iHX is not available, then the DRACS is used to remove the decay heat from the system. There are four DRACS trains connected to the ABTR vessel.[7] The DRACS heat exchangers are located in the vessel approximately adjacent to the two iHXs (see schematic in Figure 3-11). The primary system fluid enters the shell side of the annular DRACS heat exchanger. Due to the heat removal by the secondary system of the DRACS, the fluid density in the primary side of the DRACS increases, which causes the natural circulation flow. The secondary loop of the DRACS uses a sodium potassium eutectic (Na-K) fluid, which offers superior protection against freezing. The heat transferred from the primary system in the DRACS heat exchanger heats the secondary Na-K fluid.

[7] The vessel and system description section of the ABTR reference [4] identify four DHRS trains on the ABTR while the SAS4A analysis later in the same report shows three DHRS trains (e.g., see Figure 3-11 for the DRACS description from the SAS4A section of the report). The MELCOR ABTR model allowed for up to four operating DHRS trains.

The lower density Na-K rises to the secondary natural draft heat exchanger (NDHX) and the Na-K fluid flows through the shell-side of the NDHX. The tube-side of the NDHX is an air loop, which draws cool air from outside the building and cools the Na-K fluid. The heated air exits through the plant stack. There is an Na-K fluid expansion tank at the top of the Na-K loop for volume changes due to heating and cooling. Both the Na-K loop and the air loop include provisions for forced circulation. However, only their passive operation was modeled in the demonstration model. The system is started by opening a damper on the air loop as shown in Figure 3-13. The key design parameters are provided in Table 3-2.

The MELCOR DRACS nodalization is shown in Figure 3-12. The MELOR DRACS nodalization simulates the key features of the primary DRACS heat exchanger, the Na-K loop, the NDHX, the expansion tank, the air loop, air loop inlet valve, and the plant stack. The primary side of the DRACS heat exchanger connects to CV-140 (cold pool #4) and discharges to CV-130 (cold pool #3). The primary system fluid movement through the DRACS heat exchanger promotes circulation from the iHX outlet (CV-120) upwards to the primary side DRACS inlet (CV-140). The flow in the cold pool to and from the DRACS is relatively complex, which requires upward flow from the iHX outlet to the DRACS heat exchanger inlet, downward to the heat exchanger exit, and then upward to the electromechanical pump inlet. A more accurate simulation and nodalization would require guidance from a computational fluid dynamics (CFD) simulation (e.g., the approach used for pressurized water reactor severe accident hot leg and steam generation circulation patterns [16]).

Table 3-2 Key ABTR DRACS design parameters [4].

Parameter	Value
Number of trains #	4
DRACS heat exchanger capacity	625 kW per train
DRACS heat exchanger surface area	4.32 m^2 per train
DRACS primary inlet temperature	510 °C
DRACS primary exit temperature	355 °C
DRACS primary side flowrate	3.14 kg/s per train
Secondary Na-K loop flowrate	4.38 kg/s per train
Air stack cross-sectional area	8.75 m^2 per train
Air stack height	5 m

Notes:
Many places in Reference [4] report 4 DRACS trains but some places, including the schematic in Figure 3-11, indicate 3 trains. The ABTR MELCOR demo model has provisions for 0 to 4 trains available.

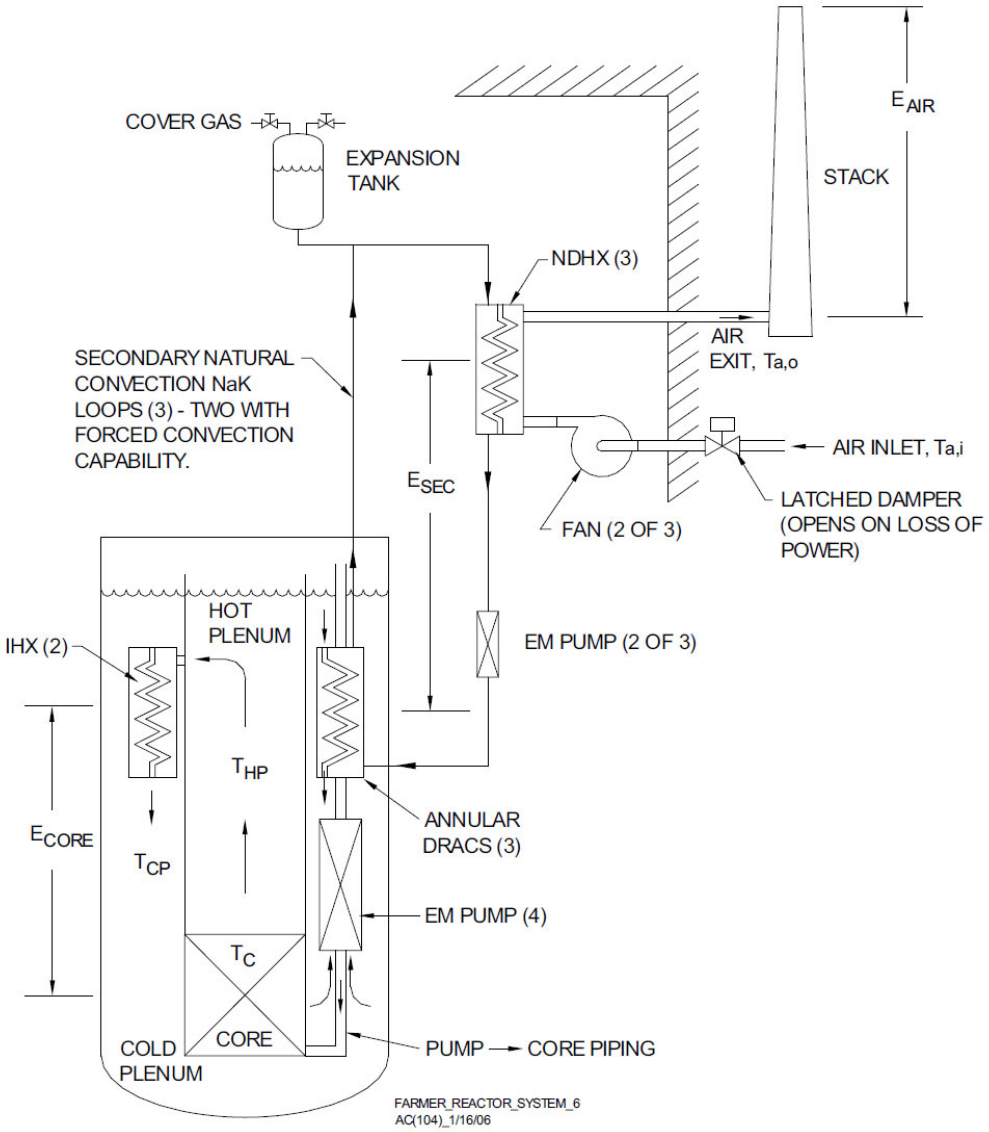

Figure 3-11 Schematic of the ABTR DRACS [4].

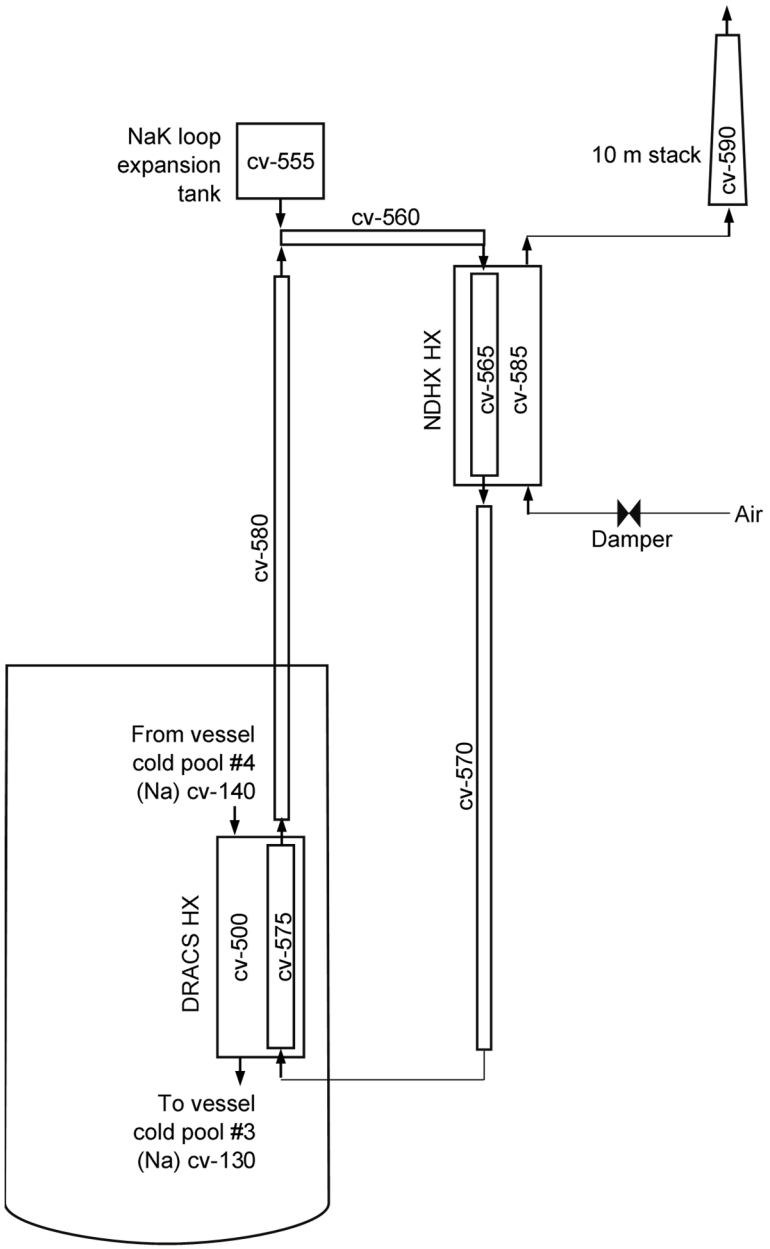

Figure 3-12 MELCOR nodalization of the ABTR DRACS.

3.2.3. Reactor containment nodalization

The ABTR containment nodalization is shown in Figure 3-13. The scope of the containment includes the reactor dome (CV-25) and the reactor cavity region around the reactor vessel (CV-10, CV-15, and CV-20). The reactor dome and presumably the entire containment pressure boundary is a low leakage structure. The large dome houses the reactor refueling equipment and is the final barrier for radionuclide release. It is a low-leakage containment structure (0.1% volume per day) with a gauge design pressure of 69 kPa (10 psig). Reference [4] also describes the dome as a protective barrier against external hazards (e.g., high winds).

The reactor cavity includes a guard vessel (CV-10) that surrounds the reactor vessel. The guard vessel is an argon-inerted, low volume vessel that contains any spills. Figure 3-4 shows the resultant

levels in the reactor and guard vessel (i.e., the faulted level) if there was a large spill from the primary system. The sodium level in the guard vessel would equilibrate just above the inlet elevation of the iHX following a sustained spill or leak.

The ABTR guard vessel is cooled by an air duct system in the reactor cavity. The forced air flow enters the reactor cavity and flows down the periphery of the reactor cavity to an opening at the bottom of the guard vessel cooling structure. The air supply and exhaust rings on the reactor cavity cooling system are shown in Figure 3-4. The air enters the gap at the bottom of the guard vessel cooling structure and flows upward adjacent to the guard vessel. There is insulation on the outside of the guard vessel to reduce the heat load to the guard vessel cooling system. CV-15 represents the air volume inside the guard cooling system. CV-20 is the air volume between the guard cooling system and the reactor cavity wall. The cavity wall has a steel liner adjacent to a thick concrete wall.

The containment dome leakage paths are located at low and high locations on the dome wall. When there is an external wind, one flow path is assigned to the upwind side of the building and the other is on the downwind side. The guidance for modeling building wind effects is described in Reference [17]. External wind effects are included in DOE facility safety analyses, where there are no strong driving forces for fission product release. The wind increases the building infiltration and exfiltration rates. This is not important for a very low leakage containment like the ABTR design versus a confinement. However, the wind-enhanced leakage was added for future flexibility in investigating a confinement design or an enhanced containment leakage scenario. Both an upwind infiltration location and a downwind location were included in the model. The wind effects are modeled as an additional Bernoulli pressure term in the flow path pressure solution,

$$dP_{Wind} = \frac{1}{2}\rho C_p v^2$$

where,

dP_{Wind}	Bernoulli wind pressure term, (Pa)
ρ	Fluid density, (kg/m^3)
C_p	Building coefficient, (-)
v	Wind velocity, (m/s)

The values for building coefficients are typically obtained using computational fluid dynamics evaluations. For wind effects modeled in the demonstration calculations, generic values were obtained from the American Society of Heating, Refrigerating and Air-Conditioning Engineers (ASHRAE) handbook (see Table 3-3 [18]).

Table 3-3 Typical building coefficients [18].

Wind Direction	Value
Upwind	0.7
Downwind	-0.4
Side and top of the building	-0.35

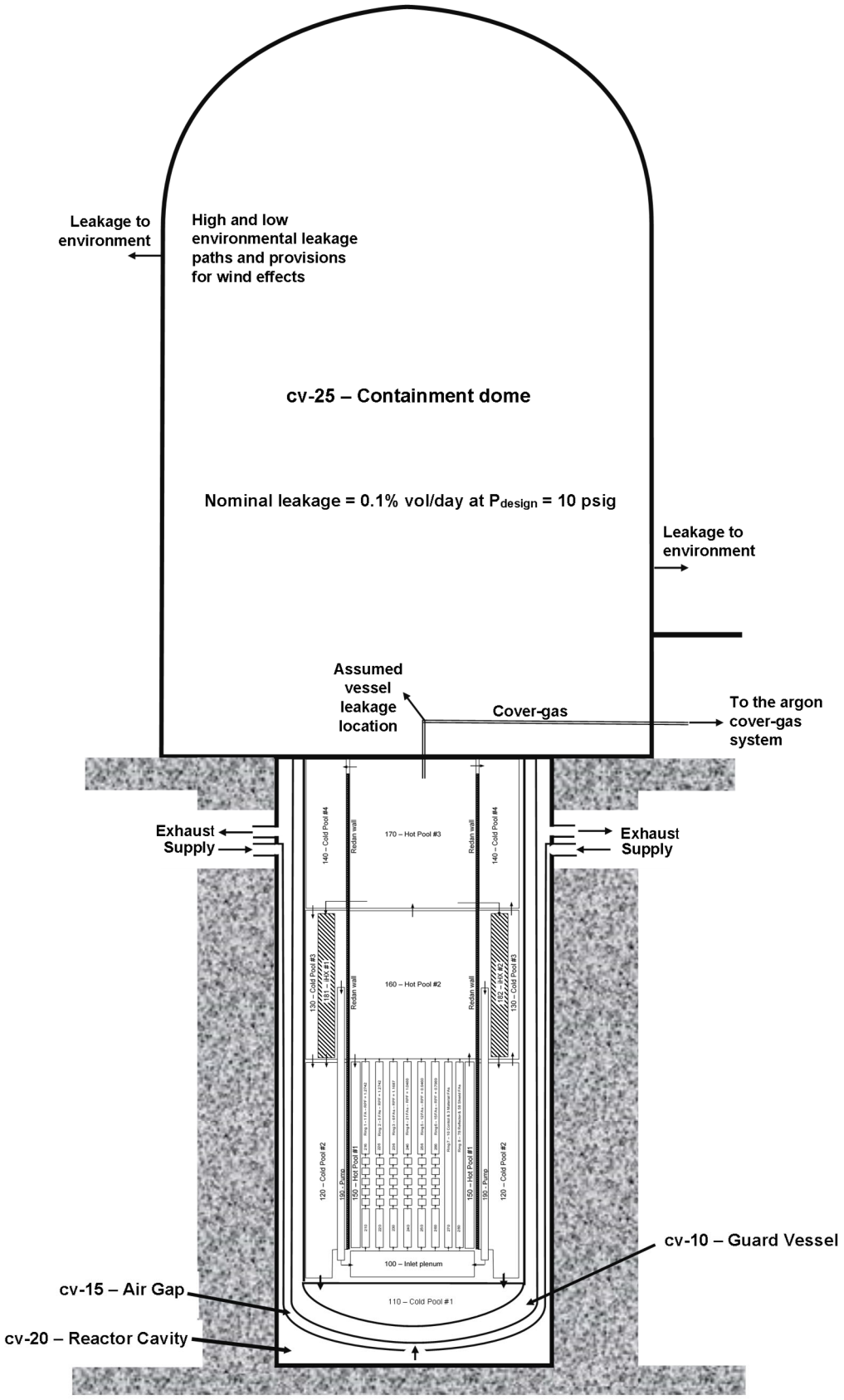

Figure 3-13 ABTR reactor containment nodalization.

3.3. Radionuclide inventory and decay heat input

The radionuclide inventory and decay heat inputs were calculated using SCALE at ORNL [6]. ORNL used a full-core, explicit assembly TRITON model (i.e., the 3-dimensional lattice physics and depletion model in the SCALE code suite) to deplete the fuel from the beginning of the equilibrium cycle to the end of the 4-month equilibrium cycle. The results from the 600 depletion zones were summed to determine the radionuclide mass inventories. Post-shutdown decay heat curves were generated for 51 data points from shutdown to 10 days. The data from the radionuclide mass inventory and decay heat curves were grouped according MELCOR's radionuclide class definitions (see Table 3-4). The decay heat powers for the 12 MELCOR classes and the total reactor decay heat power versus time after shutdown are shown in Figure 3-14. The shutdown inventories for the 12 MELCOR radionuclide classes are shown in Table 3-5. For the airborne transport of released iodine, 95% of the iodine is assumed to form cesium iodide aerosols and 5% remains in a gaseous (i.e., I_2) form.[8]

Table 3-4 MELCOR radionuclide classes.

Class	Class Name	Chemical Group	Representative Element	Member Elements
1	XE	Noble Gas	Xe	He, Ne, Ar, Kr, Xe, Rn, H, N
2	CS	Alkali Metals	Cs	Li, Na, K, Rb, Cs, Fr, Cu
3	BA	Alkaline Earths	Ba	Be, Mg, Ca, Sr, Ba, Ra, Es, Fm
4	I2	Halogens	I_2	F, Cl, Br, I, At
5	TE	Chalcogens	Te	O, S, Se, Te, Po
6	RU	Platinoids	Ru	Ru, Rh, Pd, Re, Os, Ir, Pt, Au, Ni
7	MO	Early Transition Elements	Mo	V, Cr, Fe, Co, Mn, Nb, Mo, Tc, Ta, W
8	CE	Tetravalent	Ce	Ti, Zr, Hf, Ce, Th, Pa, Np, Pu, C
9	LA	Trivalents	La	Al, Sc, Y, La, Ac, Pr, Nd, Pm, Sm, Eu, Gd, Tb, Dy, Ho, Er, Tm, Yb, Lu, Am, Cm, Bk, Cf
10	U	Uranium	U	U
11	CD	More Volatile Main Group	Cd	Cd, Hg, Zn, As, Sb, Pb, Tl, Bi
12	AG	Less Volatile Main Group	Ag	Ga, Ge, In, Sn, Ag

[8] As information from the sodium thermochemical databases becomes available, Gibbs energy minimization models can be used to identify likely chemical forms. For example, iodine may preferentially combine with sodium to form sodium iodide [24]. MELCOR includes the Thermochimica Gibbs energy minimization solver for these evaluations.

Table 3-5 ABTR radionuclide class masses.

MELCOR RN Class	MELCOR Class Mass (kg)
Noble Gases (Xe)	4.2686
Alkali Metals (Cs)	3.7145
Alkaline Earths (Ba)	1.7790
Halogens (I)	0.3686
Chalcogens (Te)	0.6049
Platinoids (Ru)	5.4353
Early Transition Elements (Mo)	68.3912
Tetravalent (Ce)	1199.52
Trivalents (La)	10.6539
Uranium (U)	3284.14
More Volatile Main Group (Cd)	0.1345
Less Volatile Main Group (Ag)	0.2780

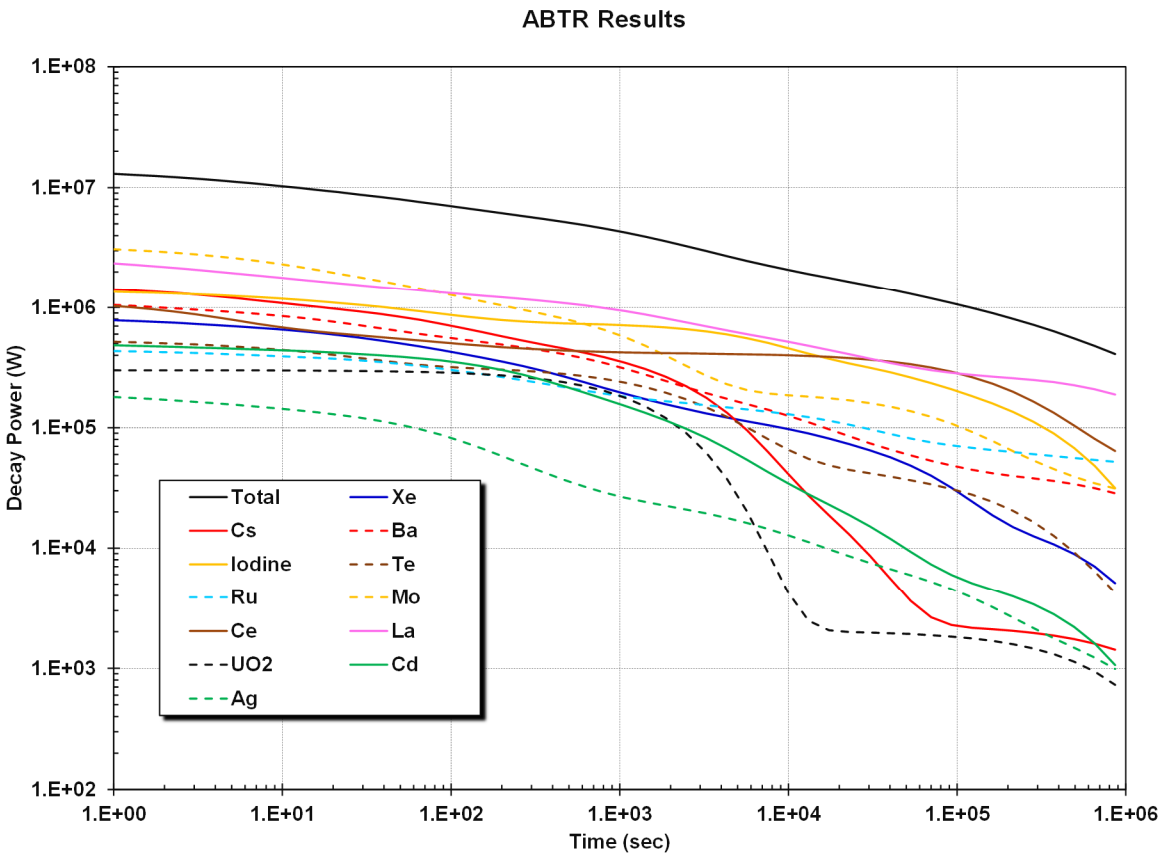

Figure 3-14 SFR decay heat curves.

3.4. Fission product release

At present, MELCOR does not have built-in provisions for radionuclide release from the metallic fuel used in the ABTR. Conceptually, the generalized release model or the various UO_2 fuel release models allow considerable flexibility via modifying user inputs to model radionuclide release from other fuel types. To support such an effort, ANL has reviewed available radionuclide release data from metallic fuel that could provide the technical basis for the MELCOR radionuclide release models [19]. The report provides integral release fractions at four temperature ranges. The first temperature range includes normal operating temperatures and slightly elevated temperatures (i.e., 500°C - 700°C). The second temperature range includes appreciable eutectic formation, but below the melting temperature of the fuel matrix (i.e., 700°C - 1100°C). The third temperature range represents temperature ranges where fuel melting occurs (i.e., 1100°C - 1300°C), and the last temperature range is high temperatures where fuel melting has occurred but below fuel vaporization. (>1300°C). The results from Reference [19] are summarized in Table 3-6.

The details and format of the data in Table 3-6 are very crude relative to the wealth of radionuclide release data from UO_2 fuel. A complication of using an integral release estimate is the uncertainty in the time-dependence. For example, the UO_2 release models use kinetic models based on time, temperature, and the properties of the radionuclides (e.g., diffusivity and vapor pressure). Consequently, a modeling scheme and assumptions are needed to use this limited data, which has

not yet been formulated. In addition, a comparison of the elements in Table 3-6 versus Table 3-5 indicate that MELCOR's default radionuclide assignments would need some minor redefinitions.[9]

Table 3-6 Metallic Fuel Release Fractions [19].

Elements	500°C - 700°C	700°C - 1100°C	1100°C - 1300°C	>1300°C
Xe, Kr	≤ 85%	≤ 100%	~100%	~100%
I, Br	≤ 15%	≤ 20%	≤ 30%	≤ 100%
Cs, Rb, Eu	≤ 55%	≤ 60%	≤ 100%	≤ 100%
Te, Sb, Se	≤ 1%	≤ 1%	≤ 5%	No data
Ba	≤ 5%	≤ 10%	≤ 15%	≤ 20%
Sr	≤ 0.1%	≤ 5%	≤ 20%	≤ 20%
Ru	≤ 0.1%	≤ 1%	≤ 5%	≤ 5%
La, Zr, Nd, Nb, Pm, Pr, Y, Cm, Am	≤ 0.1%	≤ 1%	≤ 30%	≤ 30%
Ce, Pu, Np	≤ 1%	≤ 5%	≤ 10%	≤ 15%
U, Pu	≤ 0.1%	≤ 0.1%	≤ 0.1%	≤ 0.1%

As described in Section 2.2, the SFR modeling includes models for the fission product gas migration to the gas plenum. The initial fraction of noble gases present in the gas plenum at start of the calculation is an input specification. It is assumed that 25% of the noble gas inventory migrated into the fuel pin gas plenums. Similarly, the fraction of cesium and iodine radionuclides that migrated into the sodium bond prior to the transient calculations is specified to be 5%.

A comparison of the specified ABTR radionuclide gap inventory from the previous paragraph versus the data from Reference [19] in Table 3-6 suggests some adjustments in the initial gap inventory may be warranted. The MELCOR ABTR steady state fuel temperature ranges from 405°C to 617°C. Consequently, the normal operating fuel temperatures range span from ~100°C below to ~100°C above the lower bound of the lowest temperature range in Table 3-6. The key contributors to the gap inventory are the noble gases (Xe, Kr), the halogens (I, Br), the alkali metals (Cs, Rb), the barium group (Ba, Sr), and Eu[10]. Consequently, the gap inventory could be significantly higher than specified for these radionuclide groups, which should be resolved when new metallic fuel release models are developed.

There are several complications to be resolved to use the insights from Reference [19]. For example, the specification of releases from the fuel to the gap during normal operation requires some consideration. For example, the fuel pin temperatures from the bottom to the top of the active fuel span from below the lowest temperature range in Table 3-6 to the center of the lowest range. Consequently, the lower, cooler regions of the fuel would have different releases than the top of the fuel. Similarly, the radionuclide release into the gap from the lower-powered fuel assemblies would be different than the higher-powered fuel assemblies (see Figure 3-8). Furthermore, fuel assemblies on their second or more fuel cycle may have spanned other power and temperature histories. Estimations or conservative assumptions will be needed for regions below 500°C. Since MELCOR

[9] MELCOR has default radionuclide element assignments based on LWR UO_2 fuel. However, the user input includes provisions to reassign the elements in a radionuclide class and the number of radionuclide classes.

[10] Reference [19] recommends including europium (Eu) with the alkali metals.

only tracks the overall gap inventory, the accumulated gap inventory across all regions of the fuel rod must be included. Finally, the release model will need to be separated from the gap inventory to avoid accruing of additional releases until it transitions above 700°C. An updated evaluation of the SFR gap inventory, as described above, has not yet been performed.

The SFR radionuclide release data, such as the information in Table 3-6 from Reference [19], is still being reviewed and not incorporated into MELCOR. In lieu of a SFR metallic fuel radionuclide release model, the gap inventory was specified assuming 25% of the noble gases in the gap region, 5% if the cesium, and 5% of the iodine. The data in Table 3-6 suggests up to 85% of the noble gases and 55% cesium may be released from the highest-temperature regions of the fuel and an undetermined amount from lower temperature regions. A more refined estimation would require further review of the data, examination of temperature specific releases, and incorporation of assembly-specific burnups and inventories. The present demonstration calculations and current MELCOR modeling simply specify a core-wide gap inventory, which could be further explored via uncertainty studies. However, due to the rapid release of the volatile radionuclides after the fuel melting and failure,[11] the impact of the initial gap inventory is short-lived in a severe accident and not believed to be a first-order impact on the overall source term.

3.5. Point Kinetics Modeling

MELCOR includes a six-group point kinetics model for the dynamic calculation of the reactor power. The model was developed to support the evaluation of the DOE NGNP [20] but it is flexible enough through user inputs for other reactor types. SCALE was used to determine the reactivity feedbacks for the ABTR. The axial fuel expansion, the radial grid plate expansion, the fuel density, the structure density coefficient, the sodium void worth, and the control rod worth were evaluated using SCALE. The results are shown in Table 3-7.

The reactivity feedbacks were evaluated by varying the core thermophysical properties. The fuel assembly axial expansion feedback was evaluated assuming a 1% increase in length, which corresponded 575 K increase in the fuel temperature. The thermal expansion of the lower grid plate was varied across a 293 K to 628 K temperature range, which corresponded to a pitch increase of 0.6%. The fuel density was varied by 1%. The structure density, which includes all of the HT-9 components, was varied by 1%. The sodium void worth was determined by completely voiding the assemblies. The fuel temperatures for the Doppler coefficient were evaluated over the 473 K to 1650 K temperature range. A voided correction to the Doppler was developed over the same temperature range. ORNL noted that the Doppler feedback is better fit with a logarithmic fit, which was included. Finally, the sodium void worth from filled to completely voiding the assemblies was determined and implemented as a linear feedback based on the overall assembly voiding.

All of the feedback effects were incorporated into the ABTR model except the structure density temperature and voided sodium Doppler feedbacks. The structure density included all of the HT-9 components, which spanned the temperatures of hundreds of MELCOR components and their corresponding volumes. The structural density feedback was an order of magnitude smaller than the other feedbacks. Due to its low importance and the input complications, the structural density feedback was not included.

Only one of the demonstration calculations included sodium voiding (i.e., the blocked assembly calculation) where the single assembly in Ring 1 was blocked and voided. A separate SCALE

[11] For example, nearly all of the noble gases, I, Br, Cs, Rb, and Eu as the fuel melts.

calculation was performed assuming only one assembly was voided, which showed a negligible change in the power of the affected assembly and the surrounding assemblies (i.e., within the statistical variability of the power evaluations). Furthermore, the appropriate contributions of the two correlations while during assembly voiding was not analyzed. A possible implementation of the Doppler voiding effect would be to assume linear weighting of the two correlations by the local void fraction. In summary, the voided Doppler feedback was not needed for the present calculations and implementing it presented some uncertainties and complications. Consequently, it was not included.

SCALE was also used to evaluate radial and axial power profiles. As described in Section 3.2.1, the core radial nodalization was guided by the SCALE assembly power evaluations. SCALE predicted the axial power profiles were uniform across the core (see Figure 3-15).

Table 3-7 ABTR reactivity feedbacks.

Feedback Effect	SCALE Value
Axial fuel expansion coefficient (cents/K)	-0.1347 ± 0.0033
Radial grid plate expansion coefficient (cents/K)	-0.3376 ± 0.0067
Fuel density coefficient (cents/K)	-0.2444 ± 0.0044
Structure density coefficient (cents/K)	-0.0125 ± 0.0021
Sodium void worth ($)	-0.4623 ± 0.0165
Sodium density coefficient (cents/K)	-0.1252 ± 0.0389
Doppler coefficient ($ with T in K)	-1.004 ln(T) + 15.67
Sodium voided Doppler coefficient ($ with T in K)	-0.776 ln(T) + 13.68
Primary control assemblies ($)	-22.07
Secondary control assemblies ($)	-15.77

Finally, a SCALE analysis was performed to confirm the long-term impact of xenon on an unprotected transient (i.e., unprotected without insertion of the shutdown control assemblies). In thermal reactors, the buildup and decay of xenon has a huge impact on the core reactivity feedback. SCALE confirmed that xenon has a negligible impact on the ABTR fast flux neutron spectrum reactor. Consequently, the xenon feedback is not required for unprotected ABTR transients.

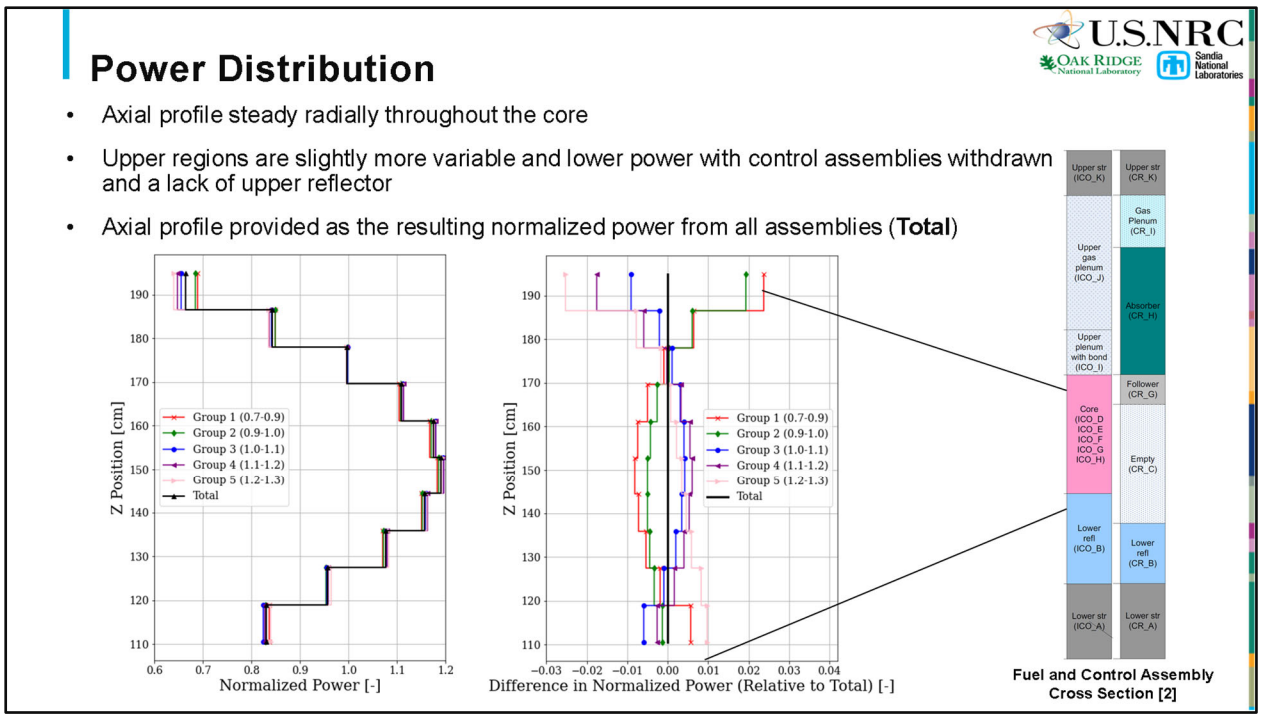

Figure 3-15 SCALE ABTR axial power profile [12].

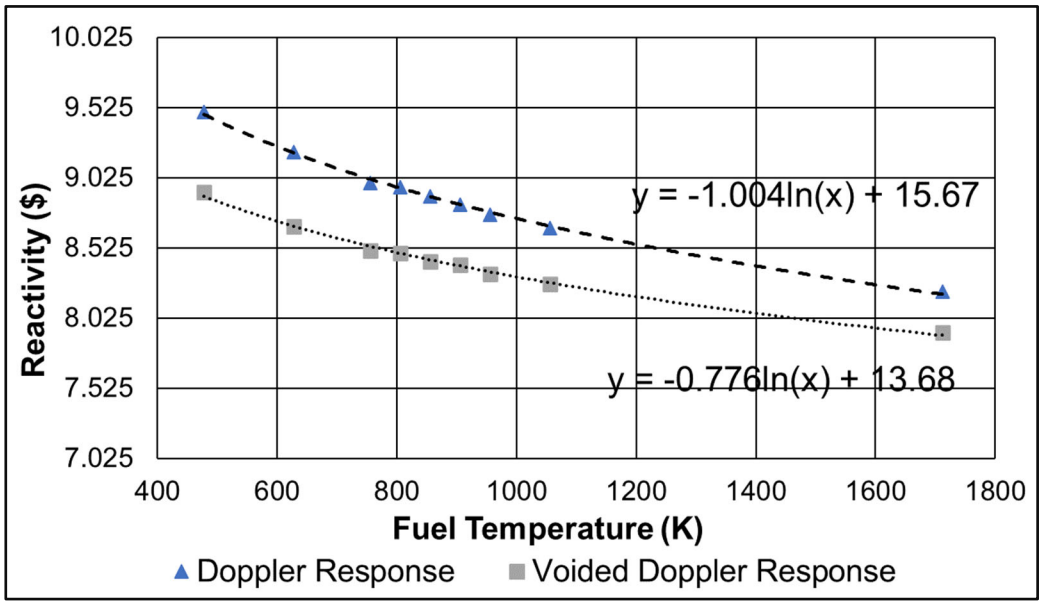

Figure 3-16 SCALE Doppler reactivity feedback curves [12].

3.6. Steady state initialization

The SFR model was initialized to steady state conditions that were provided in Reference [4]. Figure 3-17 through Figure 3-24 show the comparison to key steady state variables from Reference [4]. Due to initialization problems starting the input model with a nearly incompressible fluid at low-pressure, the model was set to isobaric and stagnant conditions. The input model initially oscillated but quickly stabilized to the rated flow rates (see Figure 3-17). A simple pump with

a proportional-integral controller was used to establish a primary system flow of 1260 kg/s. The flow split evenly between the two iHXs.

The core inlet was split between the various assemblies. The flow inlet orifices for all of the fuel assemblies were modeled the same. The inlet flow rates for the fueled assemblies were ~20.2 kg/s per assembly (see Figure 3-18). The details on the flow orifices to the non-fueled assemblies in Rings 7 and 8 were unknown (Figure 3-8). However, Figure III.7-4 in Reference [4] showed the mass flows calculated with the SAS model. The flow orifices on Rings 7 and 8 were adjusted to give ~0.3 kg/s per assembly, or only 1.5% of the fueled assembly flowrate.

The secondary system used two pumps for the two iHX loops. The pumps used a proportional-integral controller to establish 628 kg/s per assembly (see Figure 3-19).

The core inlet and outlet steady state sodium temperatures are shown in Figure 3-20. A log-mean temperature difference (LMTD) heat transfer model was used to calculate the iHX heat transfer. The sodium is heated in the core and cooled in the iHXs. The secondary side iHX inlet temperature was specified to be 333 °C from the design value in Reference [4]. The iHX secondary outlet temperature and the primary-side iHX inlet and outlet temperatures were dynamically calculated by MELCOR. The heat flux through the iHX tubes was determined from the LMTD and an effective heat transfer coefficient. The effective heat transfer coefficient was determined in the steady state using a proportional-integral controller to establish the target core inlet temperature.

The temperature drop across the iHX was 167 °C versus the design value of 155 °C. Since the iHX primary and secondary flow rates and the secondary side iHX inlet temperature matched the design values, it can be concluded that the fluid thermophysical properties used in MELCOR are slightly different from Reference [4]. The temperature difference across the iHX is approximately 7%. Consequently, the MELCOR liquid sodium heat capacity is approximately 7% lower. The difference is noted for further investigation but not resolved further for the demonstration calculations.

The secondary side temperatures are shown in Figure 3-21. The secondary side iHX inlet temperature was specified to match the design value. Similar to the vessel, the calculated temperature increase across the secondary side of the iHX is also higher than the design value. The calculated temperature rise is 169 °C versus the design value of 155 °C (i.e., ~9% higher).

The system energy balance is shown in Figure 3-22. The core thermal power of 250 MW is removed by the two iHXs. The two iHXs respond identically to remove ~125 MW per iHX. The heat generation and heat removal balance one another after the system flows and fluid temperatures stabilize. The small difference between the core power and the iHX heat removal is due to the vessel heat loss to the DRACS (<0.7% of the rated power) and heat loss to the guard vessel.[12]

The rated power is 250 MW, which is the sum of the fluid fission power (236 MW), and the decay heat from the radionuclides in the fluid (14 MW), see Figure 3-23. The ABTR decay heat power is determined from SCALE, which is an input into MELCOR.

The vessel hot and cold pool levels are shown in Figure 3-24. The hot and cold pools levels are independent and separated by the redan. A vessel mass inventory controller was used to set the hot pool level to 10.04 m above the bottom of the vessel. Figure 3-4 shows the normal difference between the hot and cold pool levels is 2.04 m, which is the offset due to the pump head on the cold

[12] The 4 trains of DRACS are operating continuously during the steady state with the damper of the air flow at 1% open. The dampers fully open with a loss of power or a plant signal for startup of the shutdown heat removal.

pool side of the redan. The calculated hot to cold pool elevation difference was 1.7 m. The pump head is the summation of the pressure drops in the iHX, the core, the pump, and the core inlet at the rated flow. There were not sufficient details in Reference [4] to better resolve the various pressure drops. Furthermore, the consistency of Figure 3-4 with the various pump options (i.e., number of pumps and electromagnetic versus mechanical design) discussed in Reference [4] is unknown. The difference is noted but not further refined.

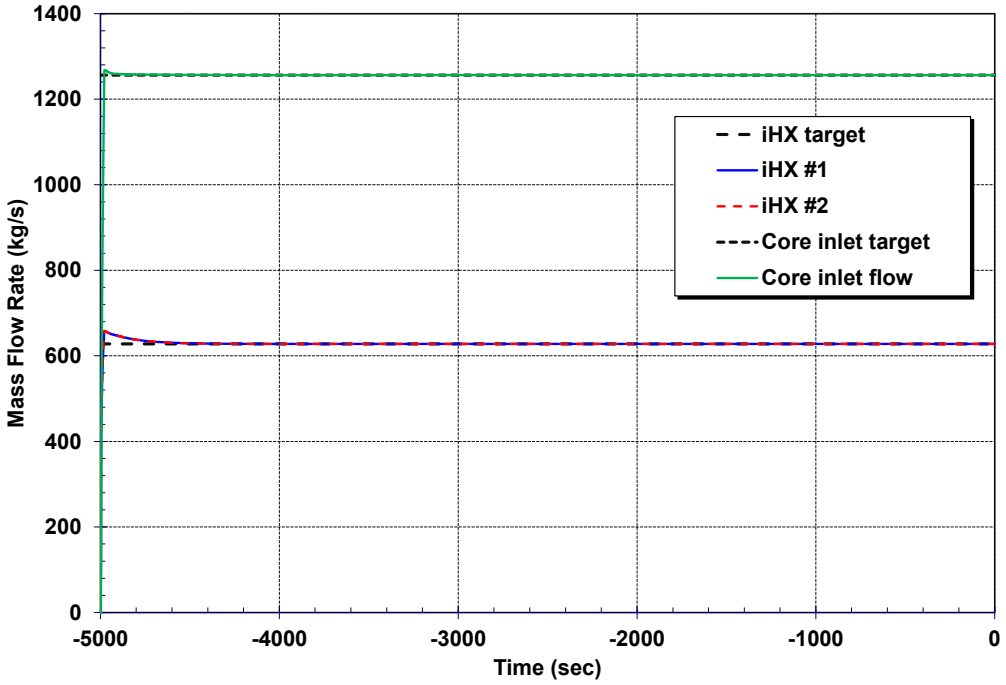

Figure 3-17 Primary iHX and core steady state flows.

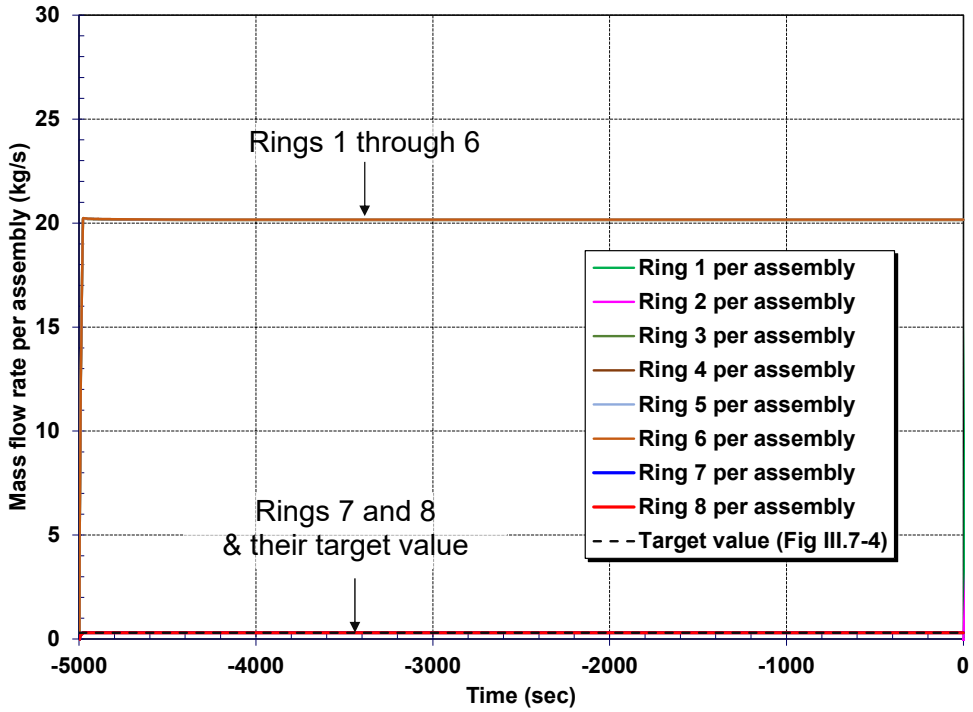

Figure 3-18 Assembly steady state flows.

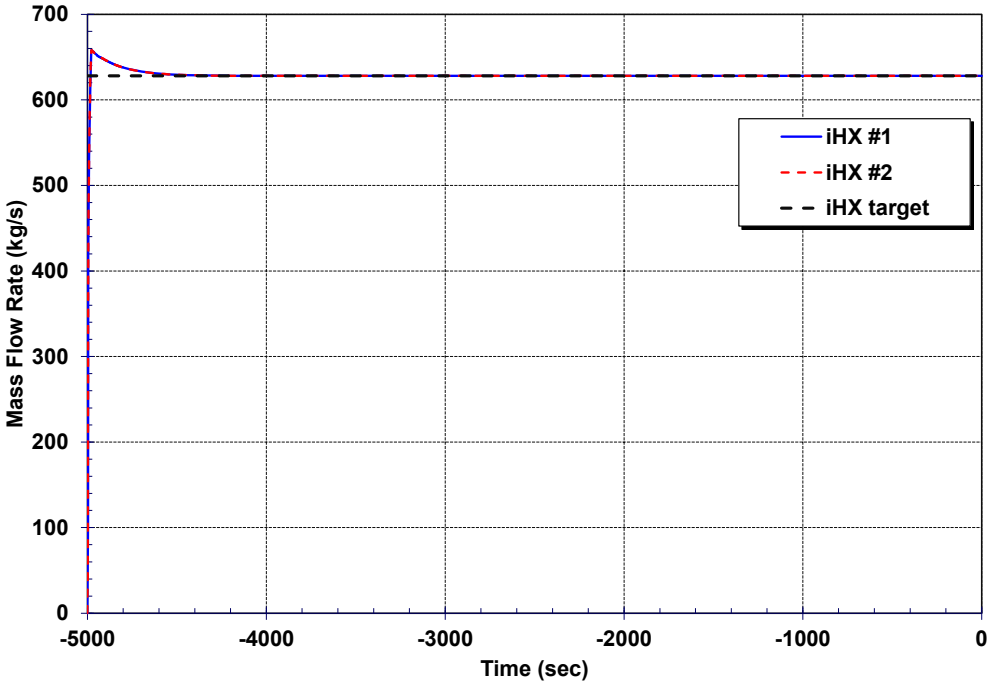

Figure 3-19 Secondary iHX steady state flows.

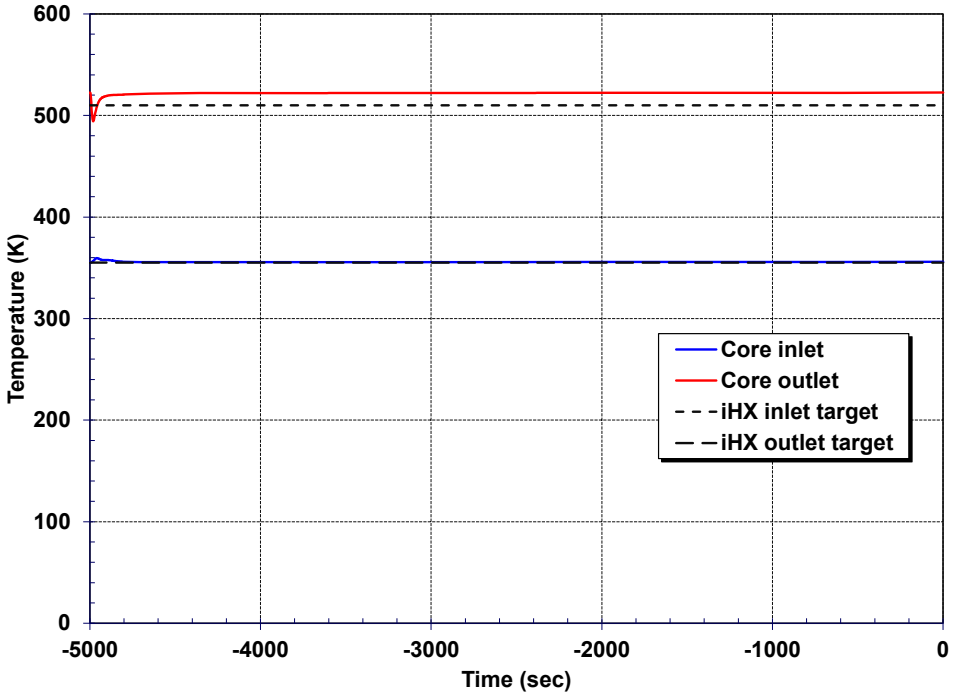

Figure 3-20 Primary system steady state temperatures.

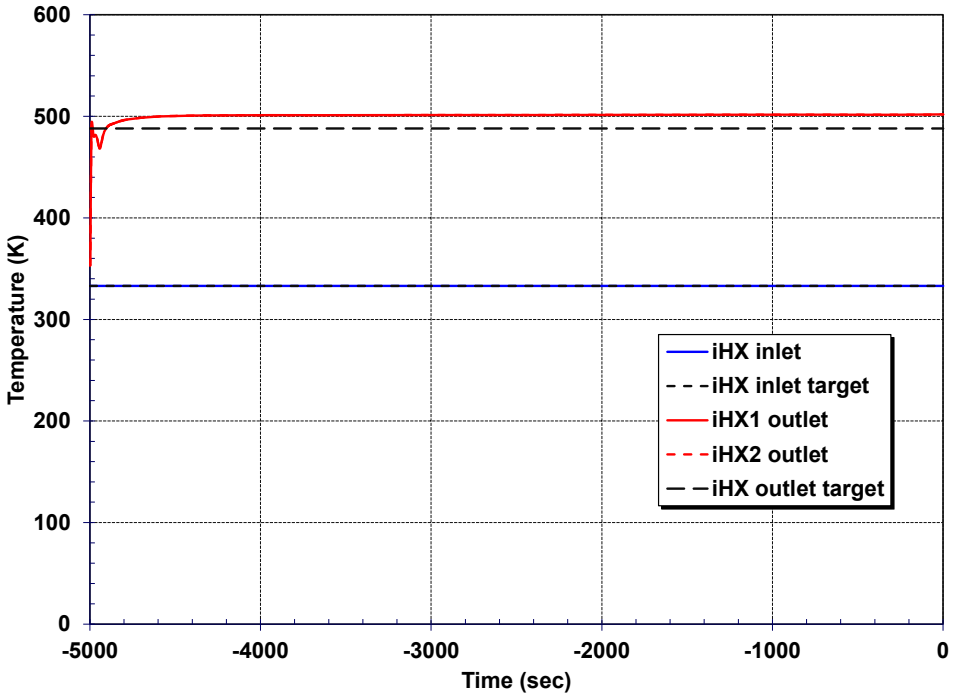

Figure 3-21 Secondary system steady state temperatures.

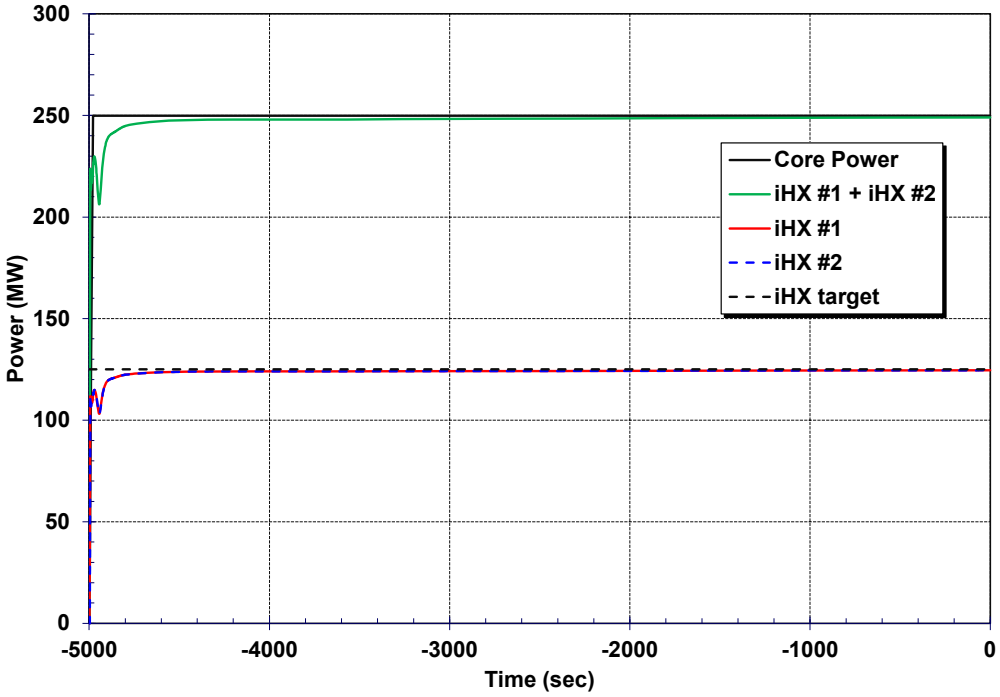

Figure 3-22 System energy balance.

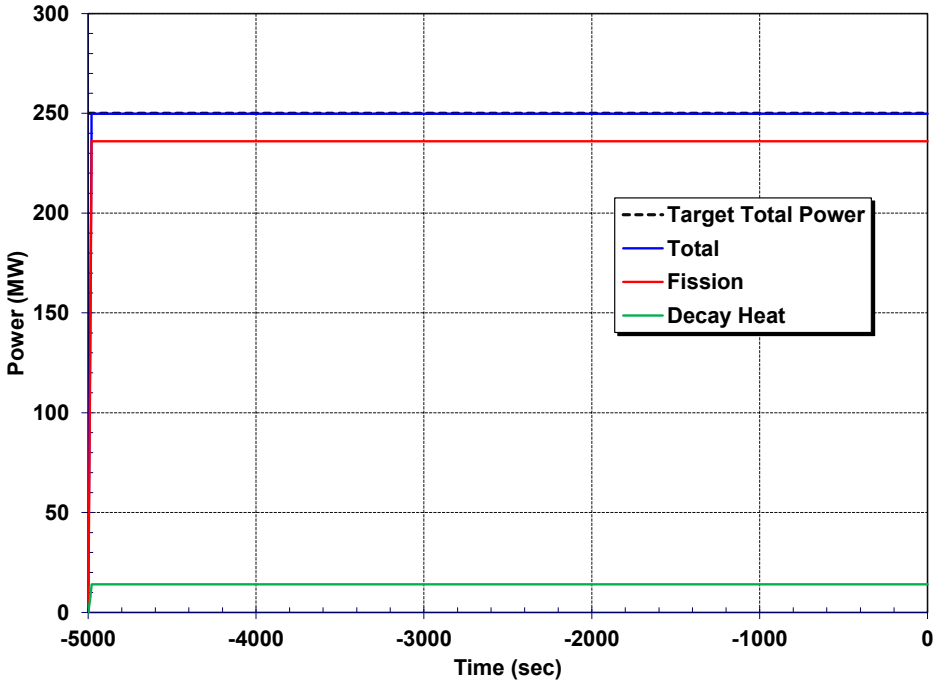

Figure 3-23 Core total, fission and decay heat powers.

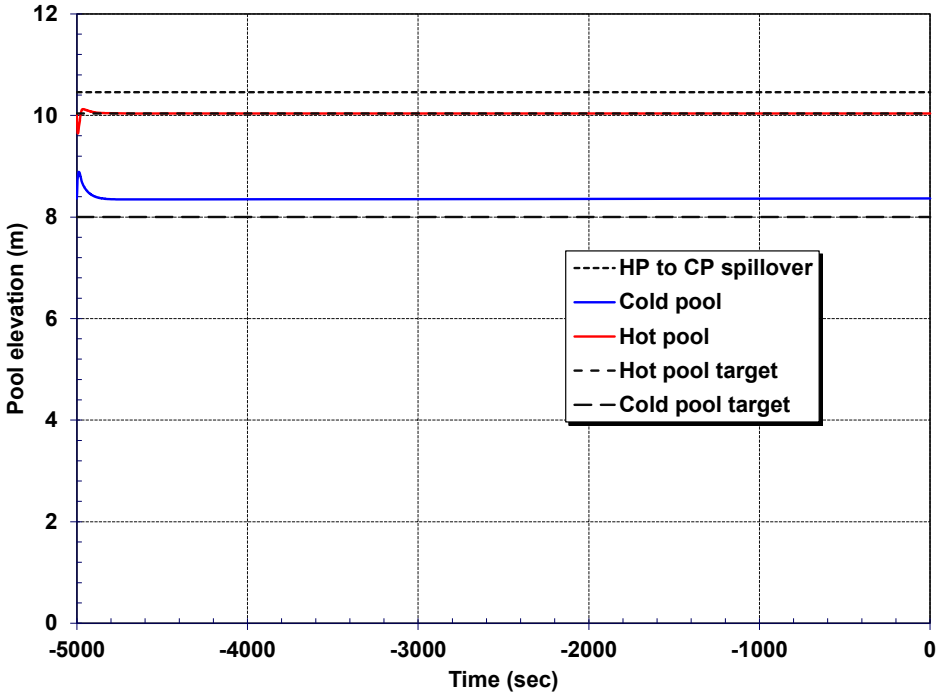

Figure 3-24 Vessel hot and cold pool levels.

3.7. DRACS model testing

The passive DRACS was particularly challenging to model due to conflicting and unclear information in the ABTR reference material. Nearly every identification of the DRACS in Reference [4] shows four separate trains except Section III.7 of Reference [4] (i.e., the SAS4A simulation section), which only identifies three trains. The SAS4A analyses consider failure of one train (i.e., 2 of 3 operating) but identifies a maximum ~2.2 MW heat removal rate (e.g., Figure III.8-2 in Reference [4]). The design DRACS heat removal rate is only 625 kW per train, or 1.25 MW for two DRACS. The MELCOR results did not exhibit such a deviation above design performance. Consequently, the MELCOR result is conservative relative to the SAS4A result but consistent with the specified design performance. Without additional design information, it was not possible to resolve the differences.

Each DRACS train includes three passive loops and three different fluids (i.e., Na, Na-K, and air). The heat transfer characteristics and flow resistances of each passive loop were balanced separately to generate the design heat removal values presented in Reference [4]. However, the air flow rate, the inlet and exit temperatures, and the NDHX heat transfer area was not reported in Reference [4]. Consequently, some testing and assumptions were needed to model the air side of the NDHX to achieve the overall system performance. The ABTR MELCOR input model includes four different, scaled DRACS input models, which allowed modeling of 0, 1, 2, 3, or 4 DRACS trains.

The transient response of the DRACS is complicated due to the coupled passive loops and complex flow patterns in the reactor vessel cold pool around the DRACS heat exchanger. Also, the beyond design basis accident simulations included in this report generated conditions that varied significantly from design values. Whether it was due to inadequate or excess heat removal capability

(which could vary throughout the transient due to the varying unprotected fission power response), the conditions in the vessel and in the DRACS system varied from the design conditions. The overall heat removal was eventually controlled by the heat removal from the air loop. The air enters the shell side of the NDHX from outside the building, flows across the tube Na-K tube bundle, and exits the NDHX to the exhaust stack (see Figure 3-11). The NDHX air-side heat removal is a function of the air flow rate and the temperature rise in the NDHX. There was limited data on the NDHX geometry and performance, especially on the air-side of the NDHX. The hydraulic flow resistance through the NDHX on the air side of the heat exchanger was tuned to remove 625 kW per DRACS train with the Na-K loop at its design conditions.

Some of the results highlighting the DRACS performance from the ULOF scenario are shown in Figure 3-25, Figure 3-26, Figure 3-27, and Figure 3-28. In this calculation, all 4 DRACS trains were operating. The calculated heat removal rates are compared to the core power in Figure 3-25. The long-term core power oscillated near at 3000 kW, which is balanced by the heat removal from the DRACS. The core fission power equilibrated to a value where the fission power plus the decay heat converged near the DRACS heat removal rate. The core power oscillations are due to small but periodic flow and temperature oscillations of the fluid entering the core (Figure 3-26).

The flow and temperature oscillations are very small but sustained due to the delayed response of the primary system and DRACS heat removal versus the core fission power response. However, the core power is self-correcting to near DRACS heat removal rate but very sensitive to small changes inlet conditions. If the core power increases above the DRACS heat removal rate, then the core temperature rises and the inherent negative temperature reactivity feedbacks causes the power to decrease. Similarly, if the core power is too low, then the core temperature decreases and the core power rises. A higher temperature leaving the core led to an increase in natural circulation flow through the DRACS and vice versa. The time lag for the fluid to circulate from the core to the DRACS and back to the core contributed to the flow and temperature oscillations.

The ULOF presents fluid conditions more severe than the design values, which contributes to higher heat removal relative to the design values. The impact of the higher DRACS heat removal rate is observable in the primary side DRACS heat exchanger flow and the Na-K loop flow as compared to their design values (see Figure 3-27). The higher core power increases the heat flow to the DRACS, which generated a higher flow rate in the DRACS flow loops than the design values. There was no design flow rate for the air flow. However, the increased heat load to the NDHX resulted in an increase in the NDHX LMTD, which is described next.

Similar to the increase in flows, the DRACS and NDHX heat exchanger LMTDs increased during the transient (see Figure 3-28). A higher LMTD increases the heat removal. The design value for the DRACS heat exchanger LMTD was available and is shown. The NDHX heat exchanger air outlet temperature was not reported in Reference [4], so there is no NDHX LTMTD design value. However, the calculated NDHX LMTD rises to 88 from 76, which was the tuned value to give the design heat removal of 625 kW per DRACS train.

The net impacts of the increased flow and larger LMTDs combined to increase the heat removal for 4 DRACS trains from 2500 kW to 2920 kW, or 730 kW per DRACS train (i.e., the design heat removal is 625 kW per train). The 17% increase in heat removal relative to the design heat removal seemed plausible. Nevertheless, there was incomplete data on the DRACS design parameters and therefore high uncertainty in conditions varying from the available design values. Sensitivity calculations are presented in Section 4.2.2 that used the DRACS model described in Section 3.2.2 and discussed here. The sensitivity calculations varied the number of DRACS trains available and

operating as a surrogate for uncharacterized uncertainties in the DRACS heat removal characteristics and the incremental impacts of fewer than 4 DRACS trains.

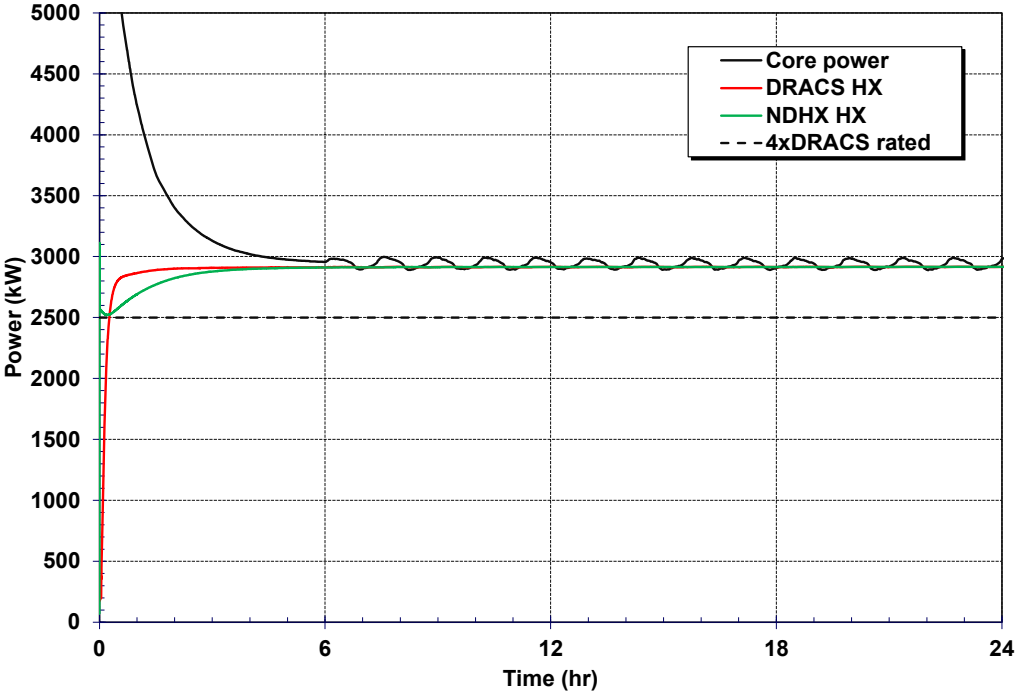

Figure 3-25 DRAC and NDHX heat removal and the LOFC core power versus the design DRACS heat removal.

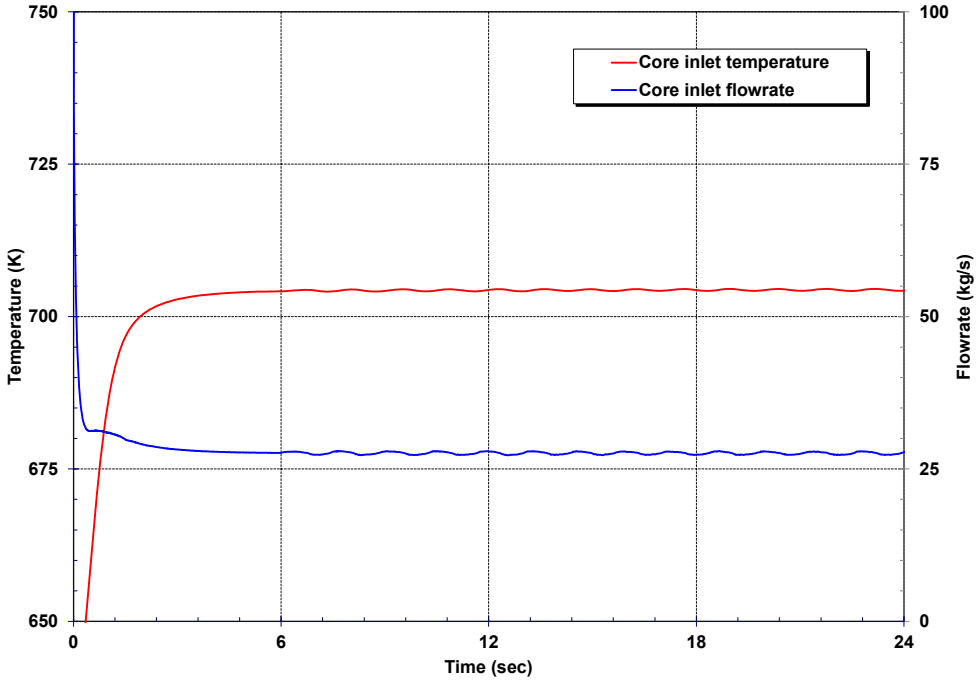

Figure 3-26 Core inlet temperature and flowrate in the LOFC.

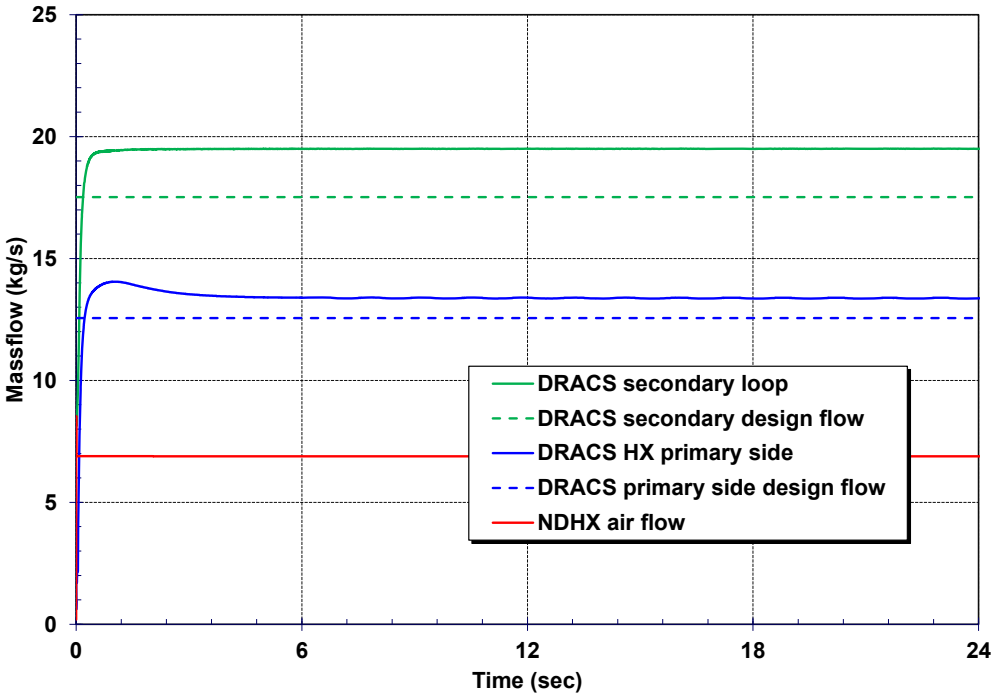

Figure 3-27 DRACS primary (Na), secondary (Na-K), and air loop flow rates.

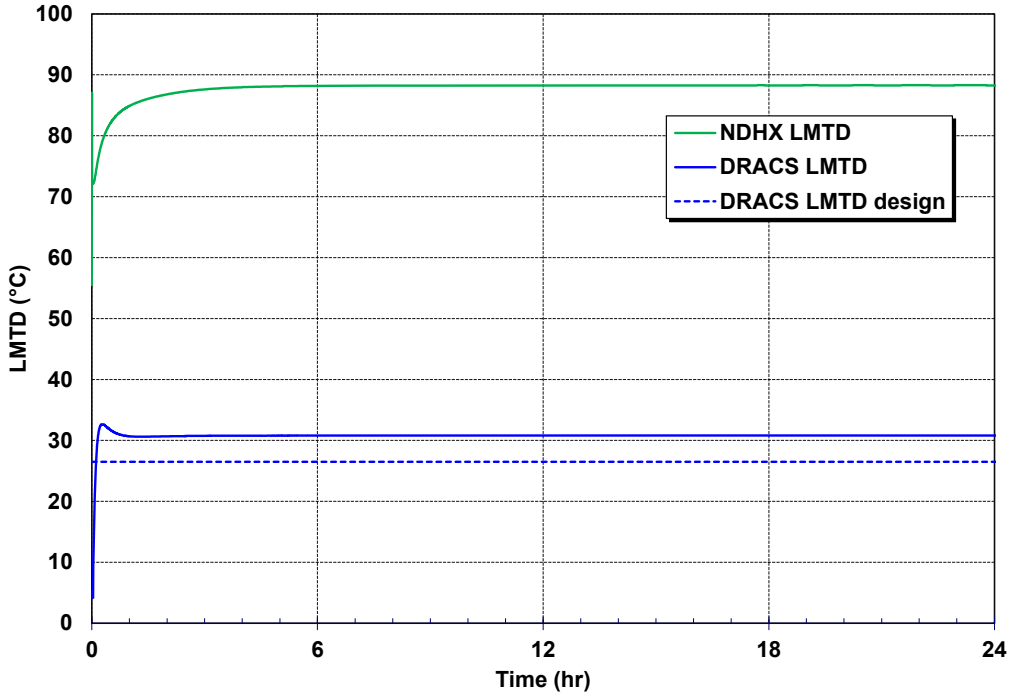

Figure 3-28 DRACS and NDHX transient LMTDs.

4. EXAMPLE RESULTS

The ABTR demonstration calculations consisted of three scenarios. The first scenario is an unprotected transient overpower (UTOP). The UTOP unprotected scenario designation corresponds to a failure of the control assemblies to insert. The transient initiator is the spurious withdraw of one or more of the inserted control assemblies, which causes an increase in the core reactivity. The second scenario is the unprotected loss-of-flow (ULOF). The ULOF scenario assumes a complete loss of power to the reactor, which includes the primary electrical power and the emergency power system. With the loss of all electrical power, the primary sodium pumps and the secondary heat removal are unavailable, which only leaves natural circulation flow in the vessel and the passive mode operation of the DRACS for the system heat removal. The final scenario is a single blocked fuel assembly transient. It assumes that the reactor is operating at full power conditions when the inlet nozzle to the highest-powered fuel assembly is blocked. The reactor protection system operates and inserts the control assemblies.

The UTOP and ULOF included some boundary condition variations to illustrate the ABTR response to varying amounts of reactivity increases and heat removal, respectively. The UTOP scenarios are discussed in Section 4.1; the ULOF scenarios are discussed in Section 4.2; and the single blocked assembly is discussed in Section 4.3. The UTOP and ULOF sequences did not have a radionuclide release. However, the blocked fuel assembly heated and degraded, which included a release of radionuclides. The discussion of the calculations also includes the thermal-hydraulic response of the ABTR reactor.

4.1. Unprotected transient overpower results

The UTOP sequence is initiated with the withdraw of one or more of the control assemblies in the core. The reactor protection system fails to insert the remaining control assemblies or stop the movement of the control assemblies that are withdrawing. The primary and intermediate pumps continue to operate and the iHXs continue to remove heat. A detailed simulation of the ABTR balance of the plant was beyond the scope of this project. It is assumed the secondary sodium iHX inlet temperature remains constant. However, the iHX heat transfer from the primary to the secondary is limited to ~280 MW, or about 12% over the design condition. The actual iHX capacity and transient sodium inlet temperature requires an integral calculation of the intermediate loop, the power conversion loop with turbine, the circulating water system, etc., which was beyond the scope of the project.

The reactivity worth of the control assemblies was analyzed for an equilibrium cycle [4]. The largest core excess reactivity occurs at the beginning of the equilibrium cycle (BOEC). The central rod assembly was determined to have the largest worth because of the higher neutron flux in the center of the core. The excess reactivity is controlled by the ABTR primary control system, which positions the control rods within the core. The critical rod position for full power at the BOEC is 63.4 cm from the bottom of the active core. The reactivity addition by a complete withdraw of the central assembly is 0.9 $.

The maximum rod withdraw speed has not been fully evaluated. However, the ABTR design report cites the maximum withdraw rate in a previous sodium fast research reactor to be 25 cm/min [4]. Based on a 63.4 cm position in the core and a 25 cm/min withdraw speed, it will take 50.9 sec to fully withdraw the central rod.

The base case response to a 0.9 $ reactivity insertion is described in Section 4.1.1. In Section 4.1.2, some sensitivity cases are presented where the magnitude of the reactivity insertion was increased

above the base case. Finally, Section 4.1.3 shows bounding results where there are no limits on the iHX heat removal. The sensitivity calculations are intended to illustrate an alternate response to base case assumption of the iHX heat removal limited to ~280 MW.

4.1.1. Base case results

The UTOP base case assumes that the highest worth central rod assembly (i.e., 0.9 $) withdraws over 50.9 sec. Figure 4-1 shows the core reactivity response to the central assembly withdraw. The dashed line is the reactivity insertion from the withdrawn control assembly, which adds 0.9 $. The other reactor feedbacks are shown in Figure 4-1 and described in Section 3.5. The ABTR's inherent negative temperature feedback works to offset the core power and temperature rise from the positive reactivity insertion. The net reactivity from the withdrawn control assembly and the other feedbacks are shown on the black line on Figure 4-1. The total reactivity initially increases above zero for ~100 sec until the combined effect of the other feedbacks causes the net reactivity to go negative. The net reactivity subsequently approaches zero.

The impact of the core reactivity on the core power calculation is shown in Figure 4-2. The core power rises with the initial increase in reactivity and decreases when the net reactivity goes negative. The core power rises to 350 MW but is subsequently limited to the maximum heat removal rate through the iHXs (i.e., assumed to be 280 MW). The long-term core power from the excess reactivity added by the withdrawn central control assembly is balanced by the heat removal from the iHXs. The increased power causes a net increase in the system temperature that generates enough negative reactivity to balance the positive reactivity from the withdrawn control assembly. The initial core power response developed more heat than could be removed by the iHX. Consequently, the temperature leaving the iHXs increased due to limited heat removal capacity.

The system temperature response is shown in Figure 4-3, which includes the core inlet temperature, the hot pool (HP) temperature at the core outlet, the upper vessel hot pool (HP) temperature, and the peak fuel temperature. The fuel temperature, as illustrated by the peak fuel temperature, increases until the inherent negative reactivity balances the positive reactivity addition. Simultaneously, the core inlet temperature increases because the heat addition from the core exceeds the maximum iHX heat removal rate (~280 MW). However, the temperatures eventually stabilize with a higher core temperature and a core power that matches the maximum iHX heat removal rate. If the core power increases above the equilibrated value (~280 MW), then the temperature leaving the iHX and entering the core would also rise. A rise in the core inlet temperature increases the overall core temperature, which introduces a negative reactivity to reduce power. The long-term temperature power response is stable and converge on the balanced configuration (i.e., see Figure 4-2 and Figure 4-3).

The highest fuel temperatures occur between 68 s to 110 sec following the reactivity insertion The hot pool has a 94 K temperature rise in response to the higher power and higher core inlet temperature. The long-term hot pool has a 257 K margin to the sodium saturation temperature (i.e., 1145 K). The peak fuel temperature has a 145 K margin to the local sodium saturation temperature in the core (i.e., 1214 K). Finally, the peak fuel temperature has a very large margin to the fuel melting temperature (1623 K). The ABTR UTOP showed a large margin to adverse consequences and had a stable response.

In summary, the ABTR response to the base case UTOP is a power increase to 350 MW and core heatup due to the positive reactivity insertion from the withdrawn control assembly. The core heatup generates negative temperature reactivity that offsets and exceeds the positive reactivity. The

core power decreases until it matches the maximum iHX heat removal capacity (i.e., assumed to be ~280 MW). The system stabilizes at core power and iHX heat removal rate of ~280 MW. The peak fuel temperature of 1068 K occurs shortly after the end of the positive reactivity insertion until the negative reactivity insertion matched the positive reactivity insertion (i.e., peak temperature from ~68 sec to 110 sec), which was below the local fluid saturation temperature (1214 K) and well below the fuel melting temperature (1623 K).

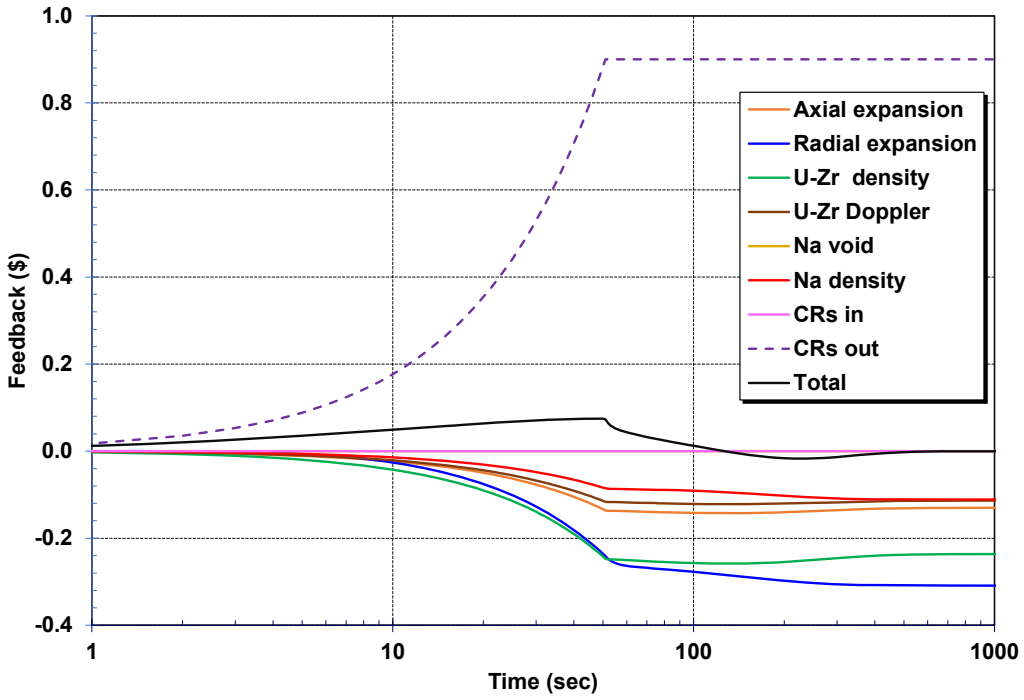

Figure 4-1 UTOP base case reactivity feedbacks.[13]

[13] The 0.9 $ reactivity from the inadvertent highest worth control rod withdraw is labeled as CRs out (i.e., subsequent sensitivity calculations show multiple rods being withdrawn). The CRs in represents reactivity worth of the normal reactor shutdown system. The UTOP is an unprotected transient. Consequently, reactor shutdown system does not operate and the CRs in remains at 0 $.

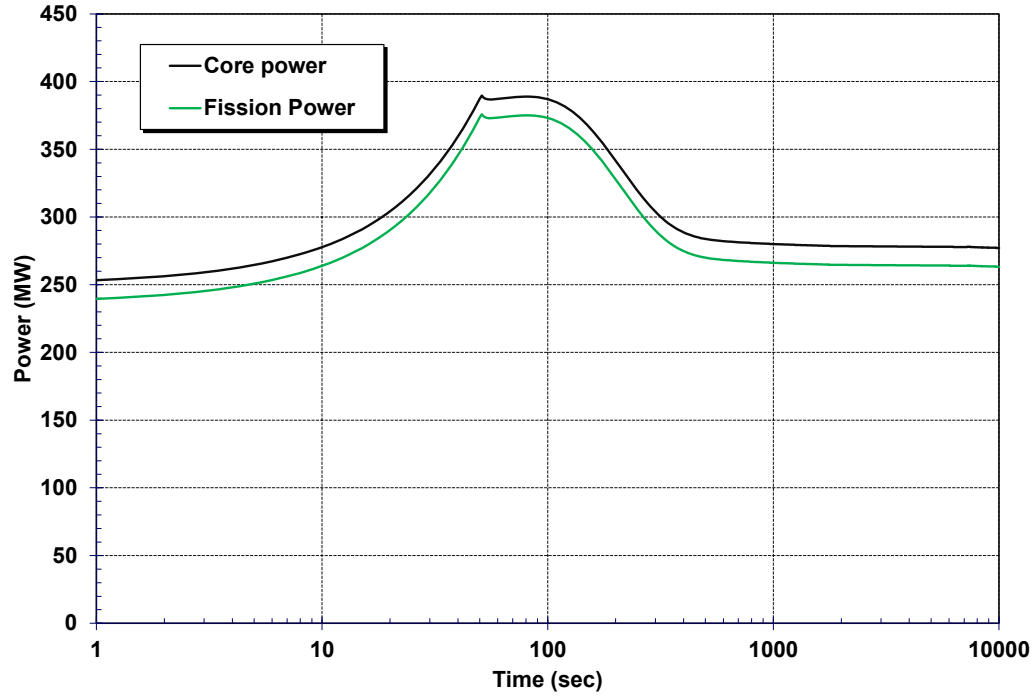

Figure 4-2 UTOP base case fission and total core power.

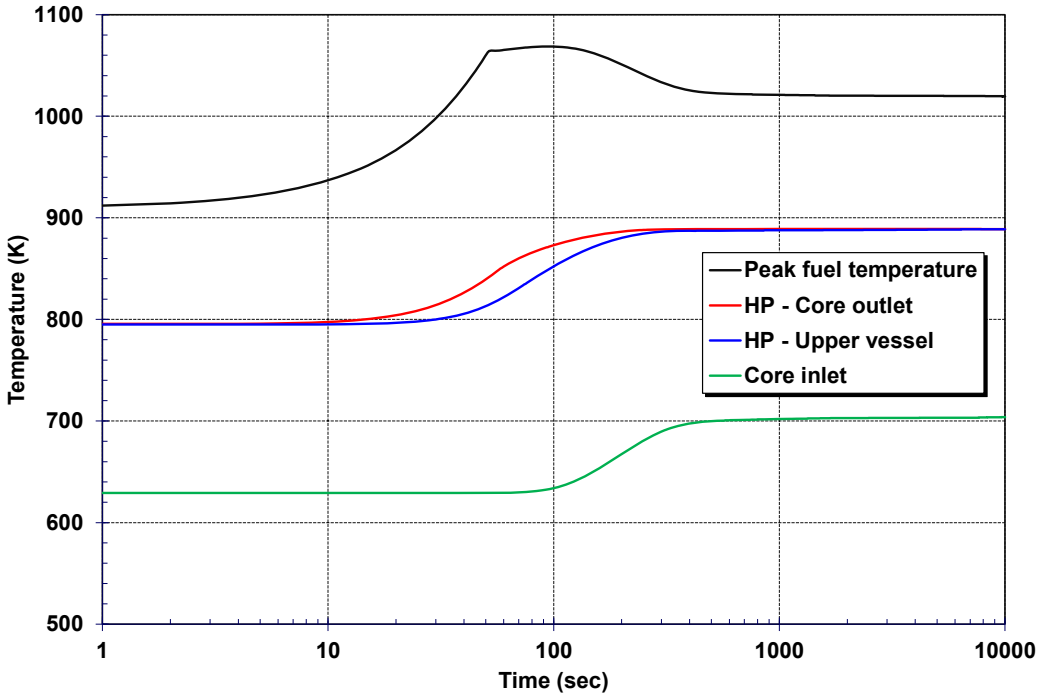

Figure 4-3 UTOP base case vessel fluid and peak fuel temperature response.

4.1.2. Reactivity insertion sensitivity case results

A set of UTOP sensitivity calculations were performed to assess the margins from more severe reactivity insertions. The sensitivity calculations assumed reactivity additions of 1.5 $, 2.0 $, 2.5 $, 2.6 $, 2.7 $, and 2.8 $.[14] The core power responses for the base and sensitivity UTOP cases are shown in Figure 4-4. Similar to the base case, the core power rises in response to the reactivity insertion. Successively larger reactivity insertions generate larger core power rises. The peak power varies from 340 MW in the base case to 692 MW in the +2.7 $ case.

The net reactivity for the sensitivity cases is shown in Figure 4-5. The response after the reactivity insertion shows successively larger negative reactivities and faster power decreases, which is attributed to the difference between the peak power and the maximum iHX heat removal rate. As explained above, the long-term core power adjusts to the iHX heat removal capacity. The overall core temperature rise adjusts to develop enough negative reactivity to balance the positive inserted reactivity. With successively higher core powers (i.e., >200% of rated), the temperature of the fluid leaving the core increases. The impact from the increase in the core outlet temperature results in a heat higher load to the iHX, which can only remove about 280 MW. Consequently, the fluid temperature leaving the iHX and entering the core rises, which leads to larger overall negative reactivities until the core power drops to ~280 MW. All cases have converged to ~280 MW by 2000 sec.

The peak fuel temperatures in the UTOP calculations are shown in Figure 4-6 relative to the sodium saturation temperature. The peak fuel temperatures were 1069 K, 1171 K, 1256 K, 1343 K, 1360 K, and 1377 K as a function of increasing reactivity insertions. The peak fuel temperature rose quickly while the control assembly was withdrawing. However, the fuel started cooling by ~100 sec once the power began decreasing. The saturation temperature at the peak fuel location is 1236 K. The corresponding amounts of subcooling in the assembly were 262 K, 180 K, 112 K, 43 K, 29 K, and 15 K as a function of increasing reactivity insertions. There was significant fluid subcooling at the time of the peak fuel temperature. The results for the 0.9 $ and 2.7 $ reactivity insertion cases are summarized in Table 4-1. For example, the fuel, cladding, local fluid, and local saturation temperatures at the peak fuel temperature location in the 2.7 $ reactivity insertion case at 100 sec were 1373 K, 1227 K, 1223 K, and 1239 K, respectively. The fuel cladding was only 12 K below the local fluid saturation temperature and the fluid subcooling relative to the cladding temperature was only 15 K. At the end of the 2.7 $ calculation (i.e., 10,000 sec), the fuel, cladding, the local fluid, and the local saturation temperatures at the peak fuel temperature location were 1207 K, 1144 K, 1142 K, and 1236 K, respectively. The fuel cladding was 92 K below the local fluid saturation temperature and the fluid subcooling had risen to 94 K.

Finally, the peak fuel temperatures had a very large margin to the fuel melting temperature (1623 K). If there was vigorous boiling or fuel melting, then the accident progression could have further degraded. There is excellent cladding to fluid heat transfer during boiling. However, boiling can increase the fluid pressure drop, which could lead to instabilities in the flow and a local dryout. Instead, the ABTR UTOP showed a large margin to boiling in the core or fuel melting for the base

[14] Initially, a 3.0 $ reactivity insertion case was attempted. However, the sodium in the highest-powered assemblies started boiling and the solution convergence slowed. The problem was traced to issues with the sodium equation of state properties, which is scheduled to be updated as part of the code modernization project. Additional calculations were performed with incrementally smaller values. The 2.7 $ reactivity insertion case ran to completion without convergence issues.

reactivity insertion of 0.9 $. The sensitivity cases with higher amounts of reactivity insertion also showed some margin to boiling up to a reactivity insertion of 2.7 $.

Table 4-1 Summary of local peak core temperatures in the 0.9 $ and the 2.7 $ reactivity sensitivity calculations.

Parameter	0.9 $ reactivity insertion		2.7 $ reactivity insertion	
	100 sec	10,000 sec	100 sec	10,000 sec
Peak fuel (K)	1069	1019	1323	1207
Peak cladding (K)	979	954	1227	1144
Sodium liquid (K)	977	953	1223	1142
Local saturation (K)	1238	1239	1239	1236
Fluid subcooling (K)	261	286	15	94
Cladding subcooling (K)	259	285	12	92
Fuel melting margin (K)	711	604	295	479

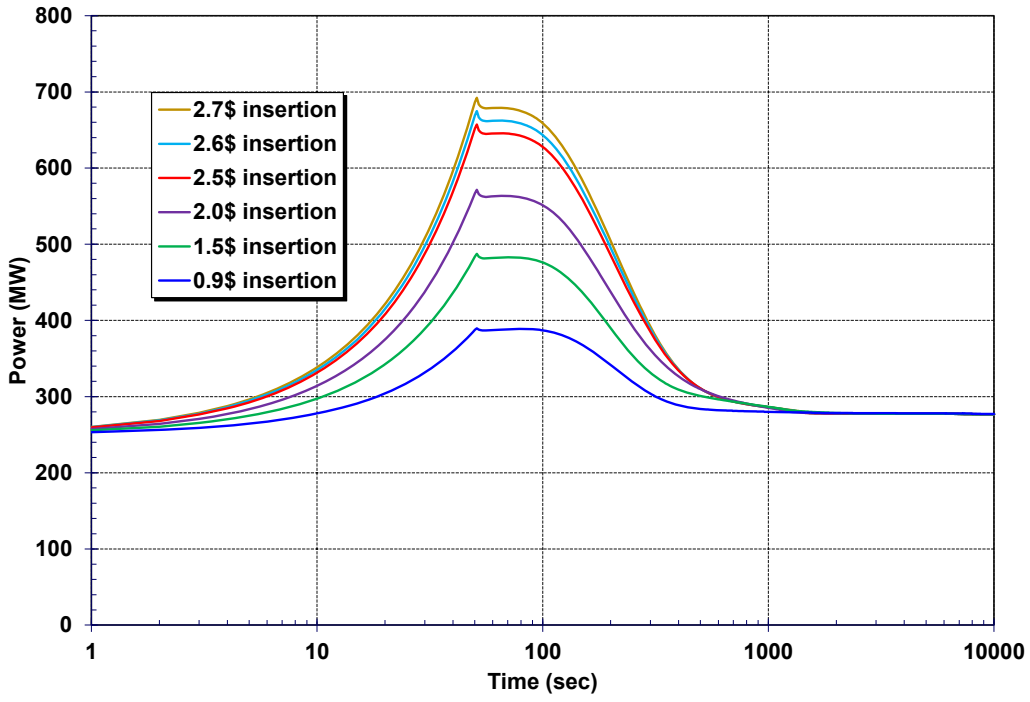

Figure 4-4 UTOP core power sensitivity results.

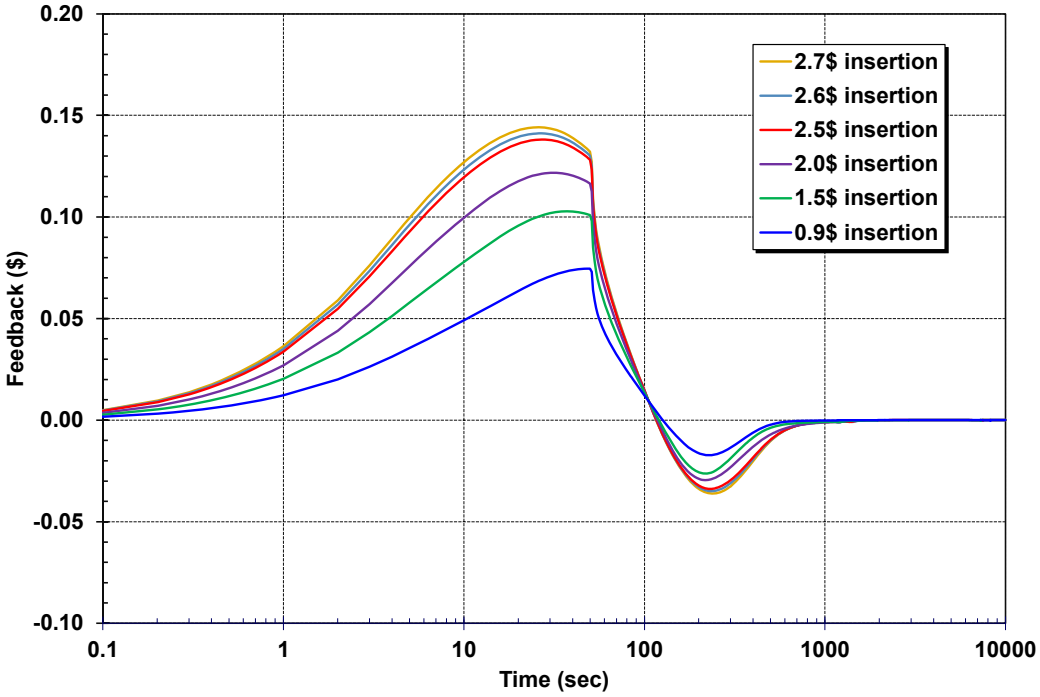

Figure 4-5 UTOP net reactivity sensitivity results.

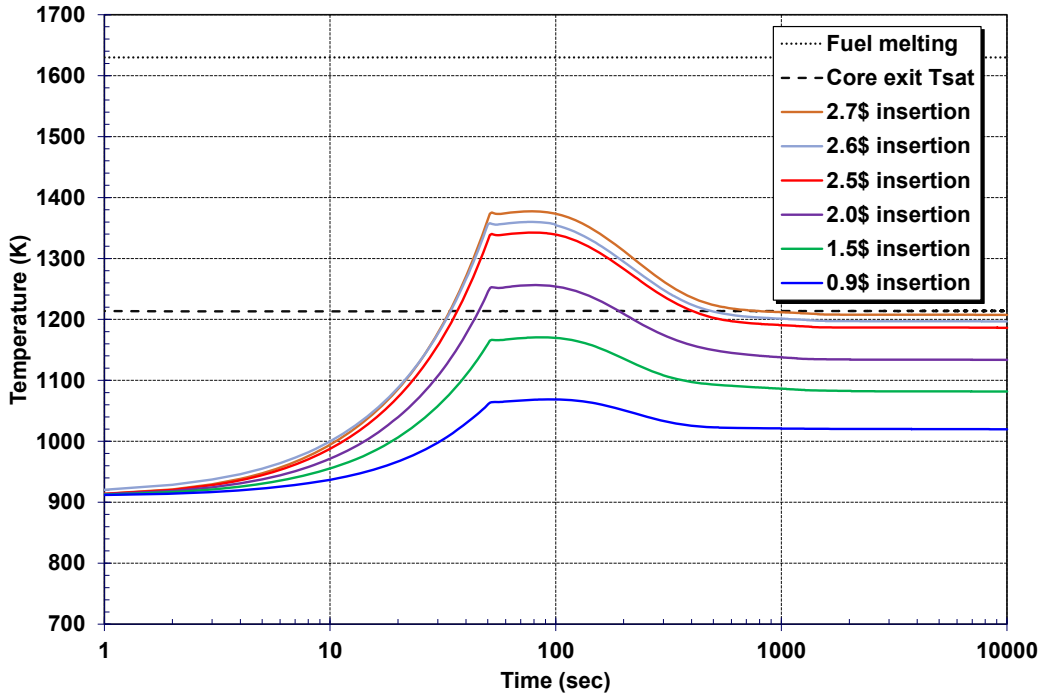

Figure 4-6 UTOP peak fuel temperature sensitivity results.

4.1.3. No limits on iHX heat removal sensitivity case results

A set of UTOP sensitivity calculations was performed to examine the impact of the iHX performance on the results. The heat removal from the iHX is expected to be limited and also a complex transient function of the intermediate sodium loop, the power conversion loop, and the cooling water system heat removal capacities and performance characteristics. There is no limit on the iHX heat removal capacity in these sensitivity calculations, which provides a bounding response. The unlimited heat removal was modeled by allowing the iHXs to maintain a steady primary-side outlet temperature. In the previous calculations, the effective heat transfer coefficient times the LMTD (U x LMTD) was limited to an overall iHX heat removal of ~280 MW, or about 12% over their rated value. In the no limit on iHX heat removal calculations, this heat removal limit was removed.

Figure 4-7 shows core power response in the limited and unlimited iHX heat removal results. The peak core powers in the two cases were similar, which was expected. The maximum core power occurred in the limited heat transfer cases before constraints of limited iHX heat removal impacted the long-term core power. The assumed boundary conditions for the unlimited iHX heat removal allowed the intermediate loop control system to maintain the normal steady state iHX outlet temperature. For example, the peak powers in the 2.7 $ reactivity insertion case for the limited and unlimited iHX heat removal were 687 MW and 692 MW, respectively. The peak powers in the 0.9 $ cases were both ~390 MW. The core power in the limited iHX heat transfer cases subsequently decreased and converged to ~280 MW. In contrast, the iHX heat removal increased in the unlimited iHX heat removal cases and remained at a high value. Although the iHX heat removal was unbounded, the core power stopped increasing when the inherent negative temperature feedbacks in the core balanced the reactivity insertion from the withdrawn control assemblies. Similar to the previous responses with limited iHX heat removal, the large thermal inertia of the sodium system allowed the negative temperature reactivity feedback to smoothly approach and offset the positive reactivity insertion.

The peak fuel temperature is shown in Figure 4-8. The peak fuel temperature has the same trends as the core power. The fuel temperature rises with the positive reactivity insertion but stabilizes and slowly decreases after the control assemblies withdraw.

Figure 4-9 compares the core inlet and exit temperatures for the limited and unlimited iHX heat removal sensitivity cases. The core fluid temperatures in the limited iHX heat removal cases (i.e., lefthand side of Figure 4-9) generated the same long-term core power at the maximum iHX heat removal rate (~280 MW) with the same approximate core temperature rises from core inlet to exit but at successively higher overall temperatures to offset higher reactivity insertions. In contrast, the unlimited iHX heat removal cases (i.e., righthand side of Figure 4-9) generated successively higher temperatures rises from the same inlet temperature as a function of increasing reactivity insertions. The core outlet temperatures were approximately the same in both sets of calculations. Furthermore, both sets of sensitivity calculations developed enough negative temperature feedback to offset the positive reactivity insertion. However, the resultant long-term core temperature profile and core power reflected the constraints of the iHX heat removal.

Finally, Figure 4-7 shows that successively higher reactivity insertions resulted in higher core powers at the end of the reactor insertion relative to the long-term power. The time scale of the radial expansion feedback at higher reactivity insertions is the primary reason for the successively larger core power decreases. Whereas the limited iHX cases all return to the same long-term core power that was only 12% higher than the steady state power, the core power in the unlimited iHX cases

(a) remained at a higher core power and (b) responded to all changes in the reactivity feedbacks due to the unlimited heat removal capacity. The heatup and expansion of the radial inlet plate occurred at a slower timescale than the other feedbacks. As the inlet plate heated and continued to expand after the initial reactivity insertion, the additional negative feedback led to a core power decrease. As shown Figure 4-10, the radial expansion feedback had increasing more negative contributions with higher reactivity insertions and their associated higher core power and average fluid temperature in the core.

Figure 4-11 also shows that the positive increase in the radial expansion feedback after the maximum negative value is larger than the positive increase in the other feedbacks. The positive increase in the radial expansion feedback was the prime factor in the long-term decrease in core power. The slower response of the negative radial feedback also occurred in the limited iHX heat removal cases but the impact on core power is not observed due to the overall system constraint to the same iHX heat removal rate. Consequently, the core temperature continuously responded to any change in radial expansion feedback to maintain a net zero total reactivity and a core power that matched the limited iHX heat removal rate (~280 MW).

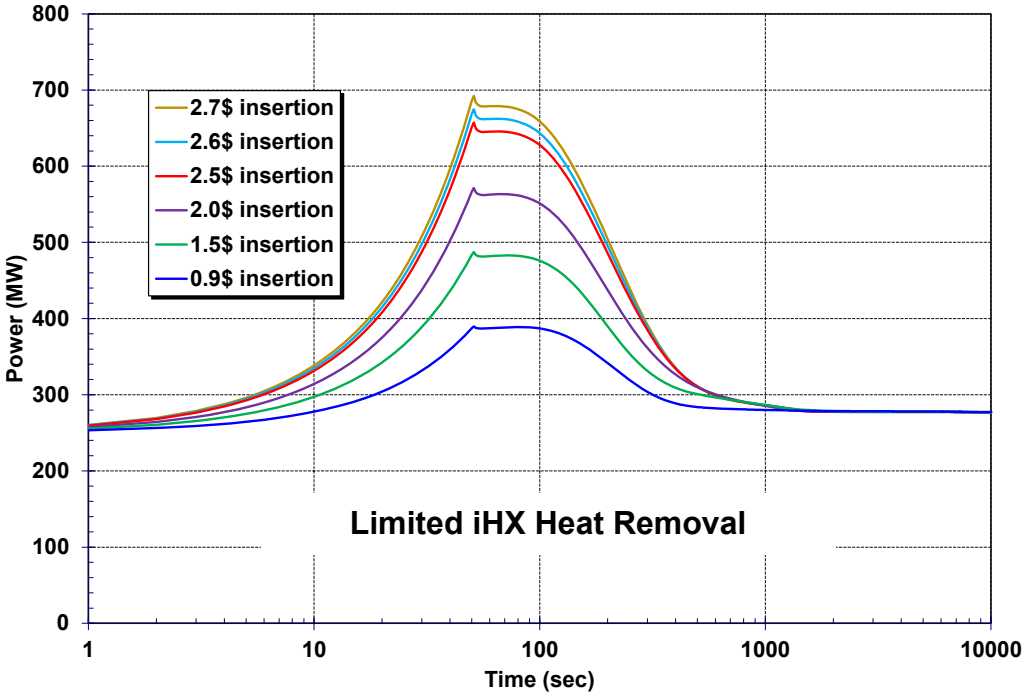

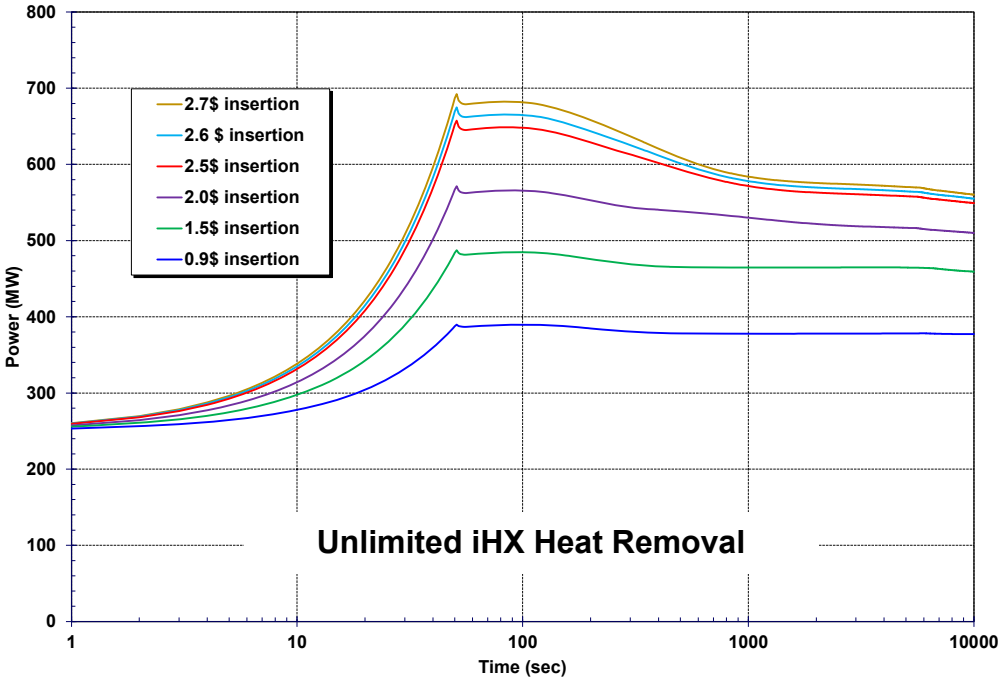

Figure 4-7 Comparison of UTOP core power sensitivity results with and without limited iHX heat removal.

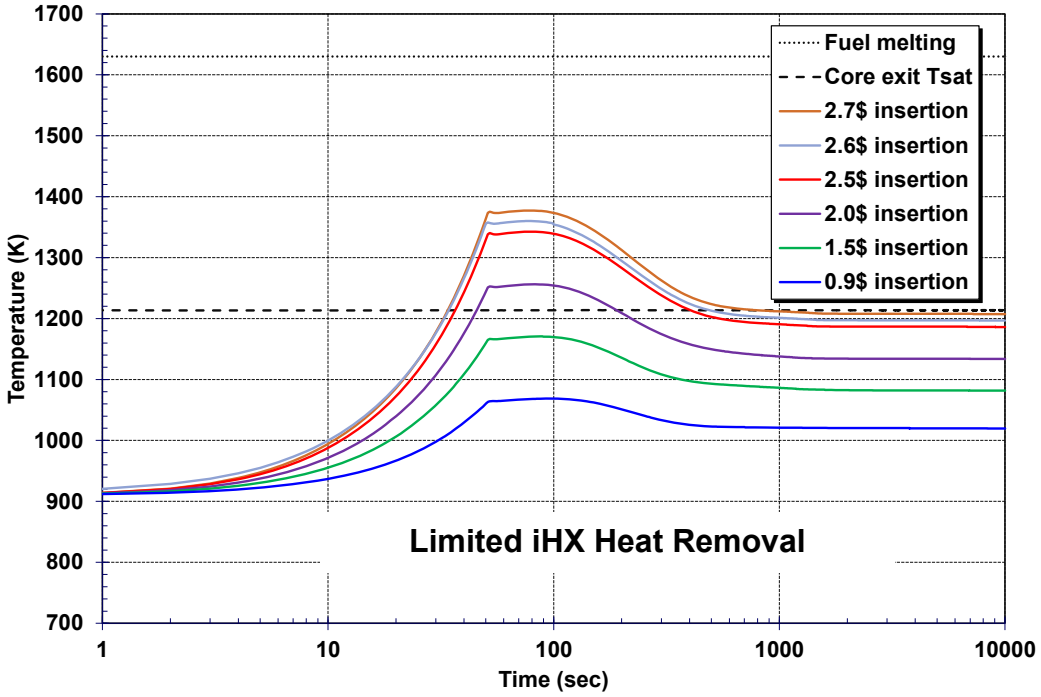

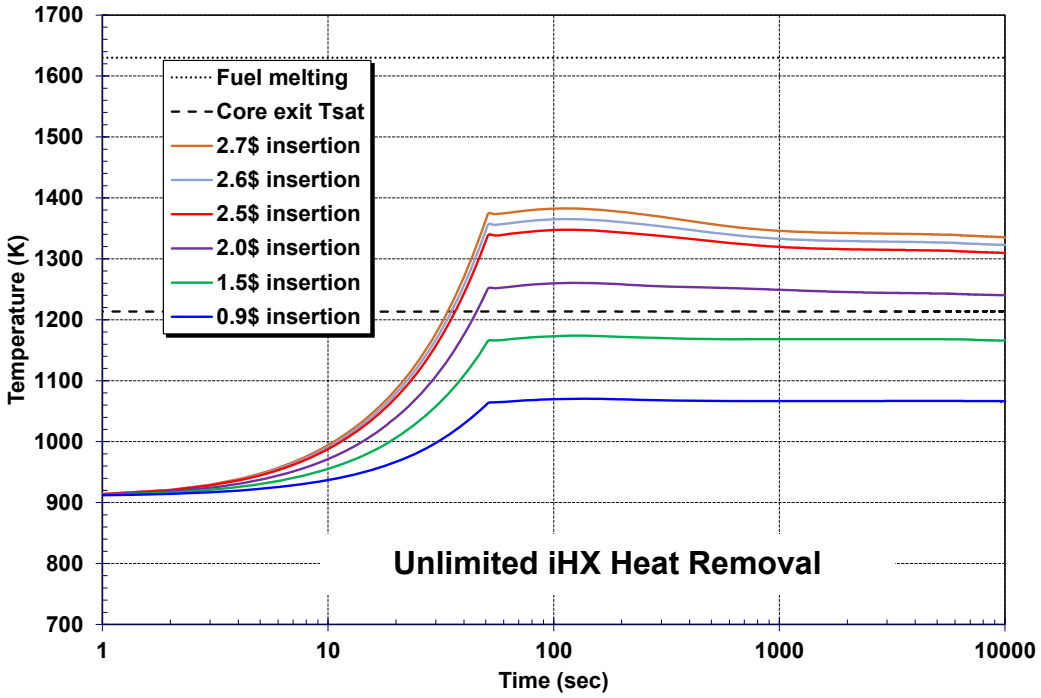

Figure 4-8 Comparison of UTOP peak fuel temperature sensitivity results with and without limited iHX heat removal.

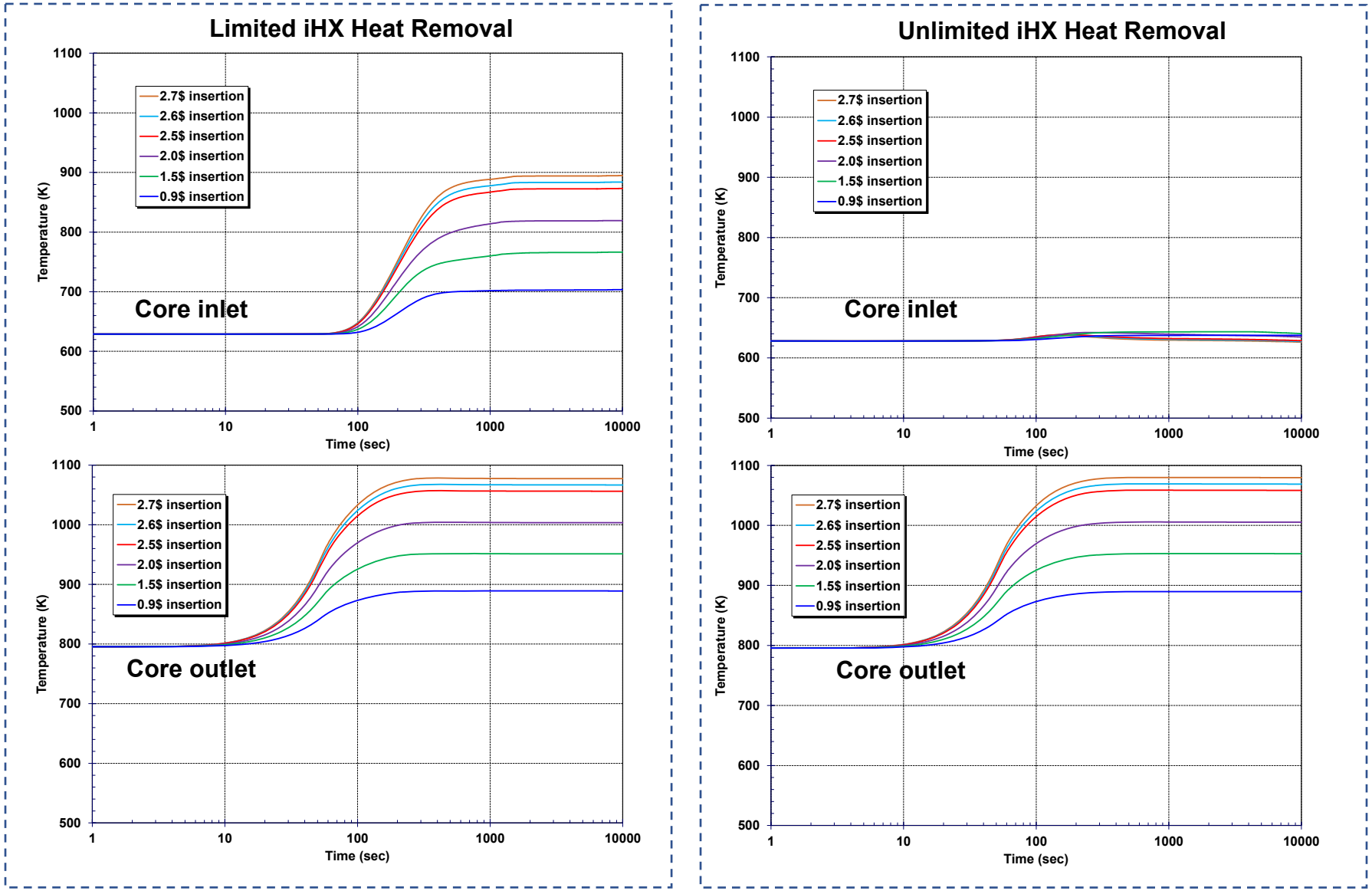

Figure 4-9 Comparison of UTOP core inlet and exit fluid temperature sensitivity results with and without limited iHX heat removal.

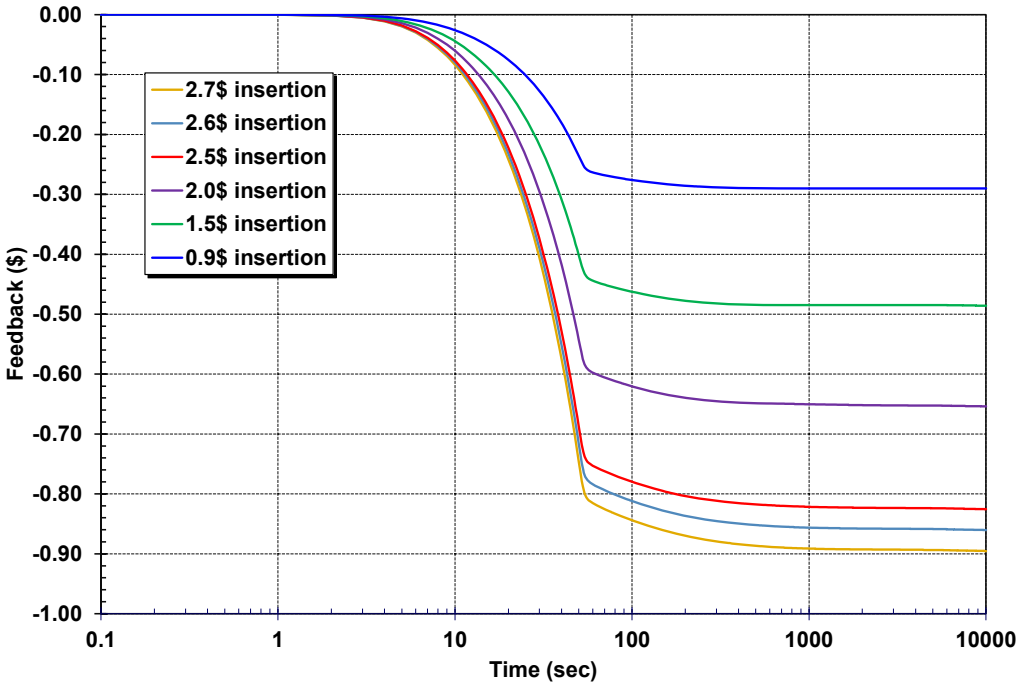

Figure 4-10 Comparison of UTOP radial expansion feedback sensitivity results with unlimited iHX heat removal.

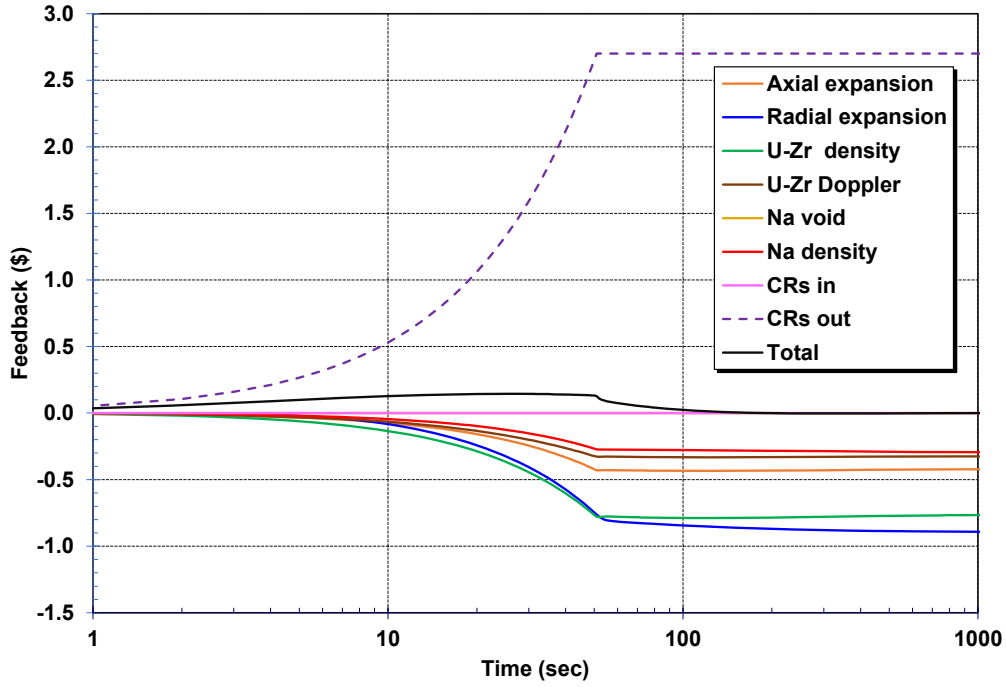

Figure 4-11 UTOP reactivity feedbacks for the 2.8 $ reactivity insertion with unlimited iHX heat removal.

4.2. Unprotected loss-of-flow results

The ULOF sequence is initiated with the failure of the primary and secondary sodium coolant pumps. The iHX heat removal also ceases after the secondary side to isolate and terminates any intermediate loop natural circulation flow. The reactor protection system fails to insert the control assemblies in response to the loss of the primary and secondary pumps. Consequently, the ULOF has the compounding effects of no forced circulation, no heat removal, and no active system termination of the fission reaction. The passive mode of the DRACS is the only means of heat removal. The ULOF base case is shown in Section 4.2.1. The base case assumes 4 DRACS trains are available for passive heat removal. Section 4.2.2 presents sensitivity cases with 0, 1, 2, 3, or 4 operating DRACS trains.

4.2.1. Base case results

The ULOF base case assumes 4 DRACS trains are available for heat removal. The DRACS includes forced circulation fans and pumps for the air flow and the secondary Na-K loop, respectively. However, it is assumed only the passive circulation mode is available. The DRACS design rating is 625 kW per train, but the heat removal rates vary as conditions change from the design values. The primary and intermediate pump flow coast down rates from the SAS4 analysis in Reference [4] were used, which is a halving time of 7 seconds.

The initial challenges to the reactor in a ULOF are the high core power and decreasing flow. Figure 4-12 shows the primary and intermediate pump flow rate response to the ULOF. The pumps coast down in response to the loss-of-power. The intermediate system is assumed to isolate after the pumps coast down but the there is a persistent natural circulation flow through primary system pumps. The primary system flow decreases to 10% of the rated flow within 50 sec, which is the natural circulation flow without the pumps.

As shown in Figure 4-13, the core power decreases in response to the decrease in flow and loss of the intermediate system heat removal. Simultaneously, there is negligible heat removal from the DRACS for ~160 sec until the in-vessel thermal gradients start to establish flows through the DRACS and NDHX heat exchangers. The DRACS heat removal does not match the core power for ~11,000 sec. Consequently, the primary system and the core are heating during this timeframe. The core heatup causes a negative temperature reactivity that lowers the core power, which are discussed next.

The temperature rise of the fuel and the hot pool temperature at the core exit was relatively small, as shown Figure 4-14. The maximum fuel temperature started decreasing after 60 sec and cooled to 800 K, or about 112 K below the steady state value (i.e., 912 K). Over the same timeframe, the core outlet temperature also increases to 809 K by 120 sec before eventually stabilizing to ~768 K. The core inlet began a sustained heatup from 629 K to 713 K. The core inlet fluid comes through the pumps from the Cold Pool DRACS outlet (i.e., see temperatures in Figure 4-14 and nodalization in Figure 3-9). The cold pool heats due to the loss of the iHX heat removal but benefits from the DRACS heat removal. The net effects are a heatup of the fluid entering the core, an increase in the overall core fluid and structure temperatures, and a decrease in the core power. The overall increase in the core structure and fluid temperatures is best shown through the various inherent negative reactivities, which is discussed next.

Figure 4-15 shows the various core reactivities and their responses. Each of the core reactivity feedbacks discussed in Section 3.5 has an inherent negative temperature contribution. Each feedback term is formed by calculating the local temperature change from steady state times the feedback

term. All reactivities are decreasing, which corresponds to fuel, fluid, and structure temperature increases. The maximum total negative feedback is -1 $ at 70 sec. The large negative magnitude of the total reactivity rapidly decreases the total core power (see Figure 4-13) to 21 MW by 100 sec and 6 MW by 1000 sec. However, the steady reduction in core power and an increase in the relative DRACS effectiveness eventually resulted in a positive reactivity at 1900 sec. The total reactivity oscillated around 0 $ until ~10,000 sec when the fission power started to increase. The fission power increase combines with the core decay heat power to oscillate the near the DRACS heat removal rate. The system stabilizes in this configuration with small and slow oscillations in the fission power (i.e., see Figure 4-16, approximately ±40 kW fission power fluctuations). The fission power steadily increases as the decay power decreases. However, the total core power is approximately constant after 11,000 sec.

In summary, the ABTR response to the base case ULOF is a core heatup that reduces the core power. The system heats up and absorbs the energy addition from the core. The system stabilizes when the core power and the DRACS heat removal are balanced at ~11,000 sec. A peak fuel temperature of 946 K occurred at the beginning of the transient (i.e., 57 sec), which was well below the fluid saturation temperature (1214 K) or the fuel melting temperature (1623 K).

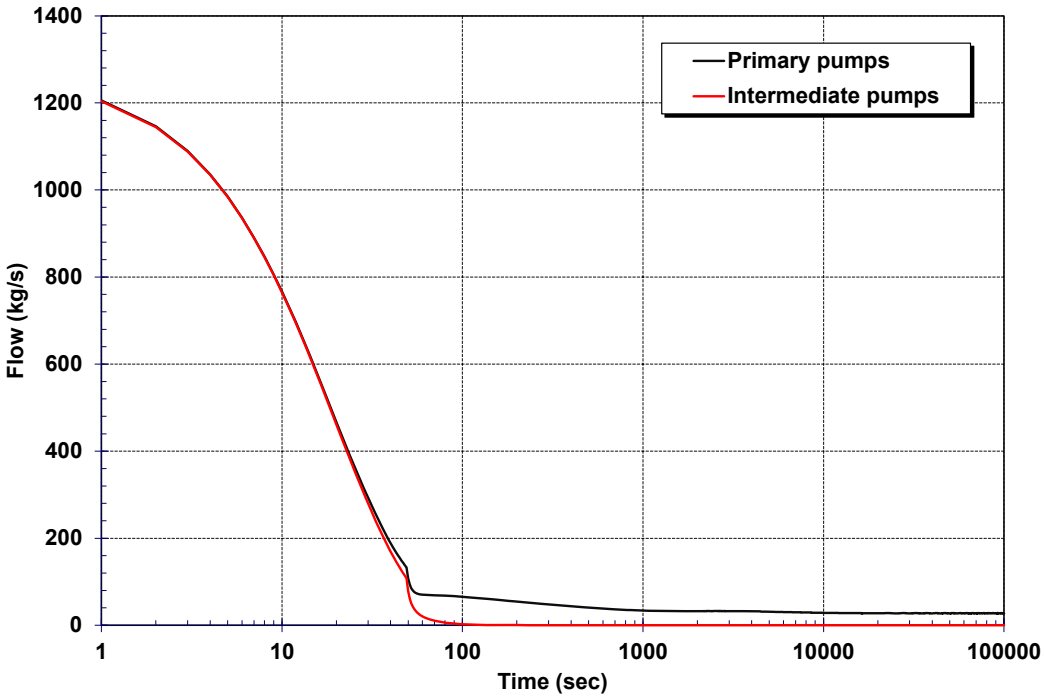

Figure 4-12 ULOF base case primary and intermediate pump flows.

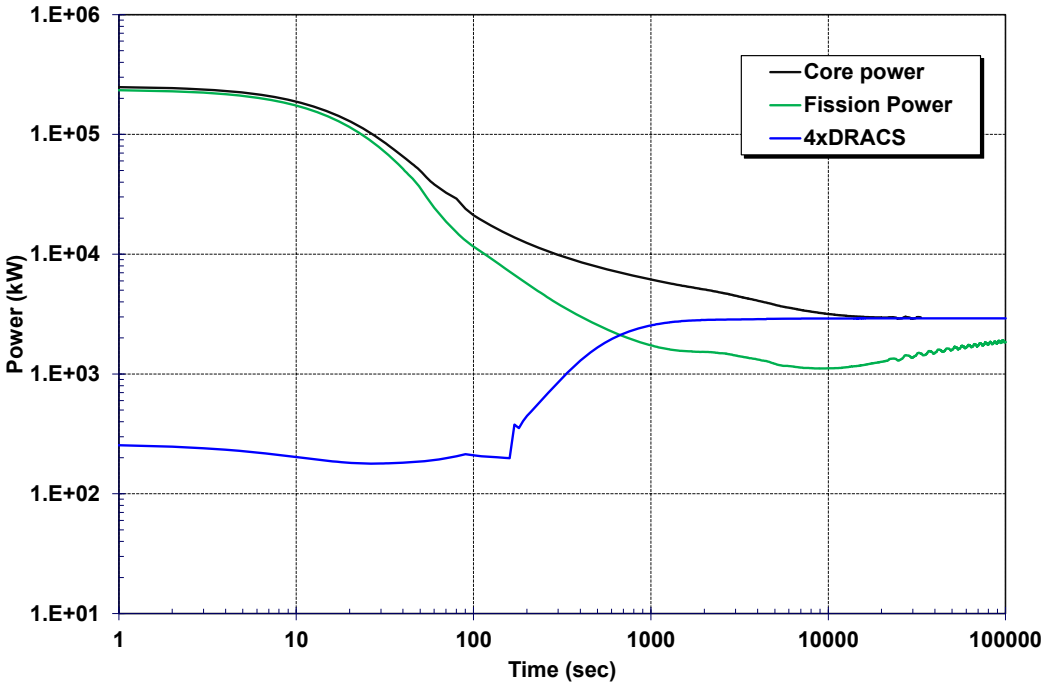

Figure 4-13 ULOF base case total, fission, and DRACS power.

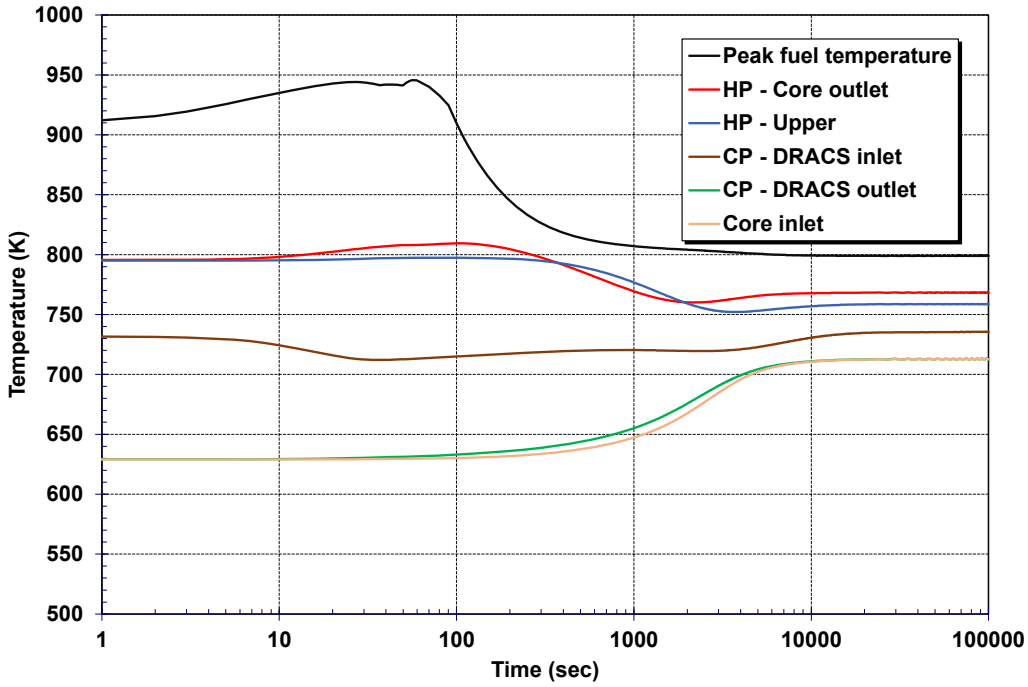

Figure 4-14 ULOF base case peak fuel, hot pool, and cold pool temperatures.

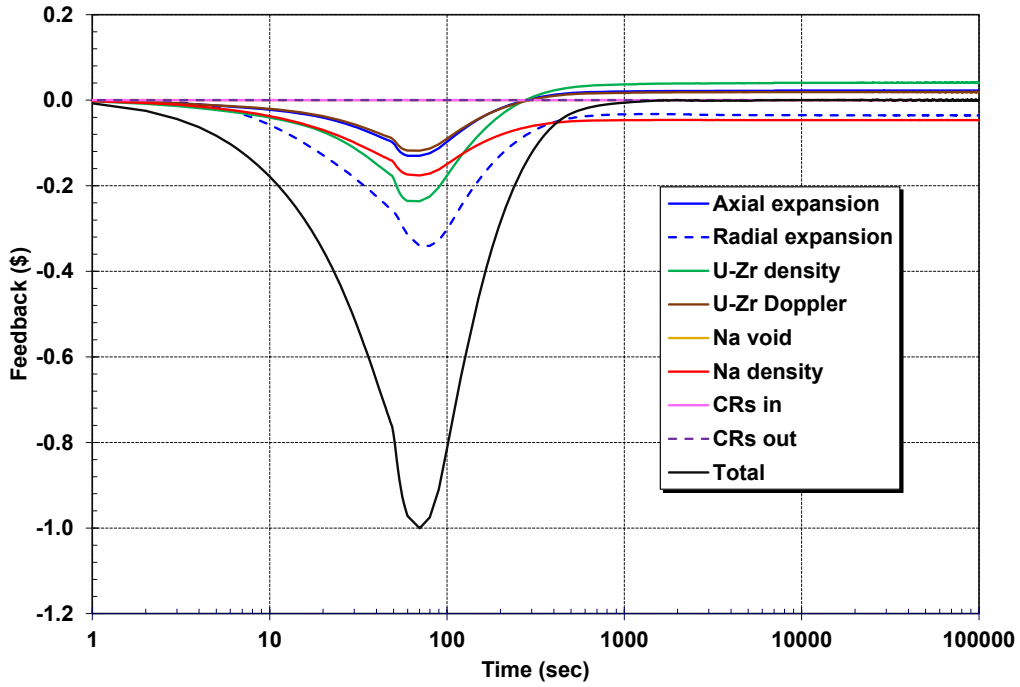

Figure 4-15 ULOF base case reactivity feedbacks.

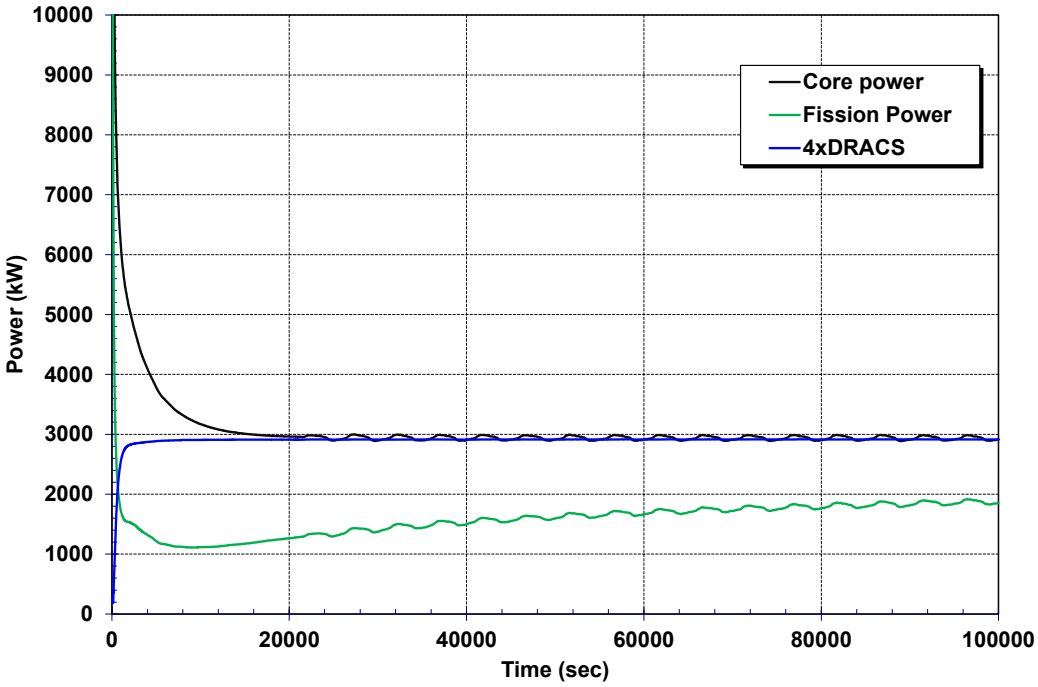

Figure 4-16 ULOF base case total, fission, and DRACS power (linear scales)

4.2.2. DRACS sensitivity results

A set of ULOF sensitivity calculations was performed to assess the system response to less DRACS heat removal capacity. As discussed in Section 3.7, there was missing information in the DRACS geometry and design specifications. The ULOF sensitivity cases address system failures, system availabilities (e.g., repairs), alternate designs (i.e., some places in Reference [4] indicated only 3 trains), or different off-design performance characteristics from the MELCOR calculations. The sensitivity calculations compare the ULOF base case response with 4 DRACS trains versus the response with 3, 2, 1, and no DRACS trains.

A comparison of the ULOF core power versus the DRACS heat removal for the ULOF DRACS sensitivity cases is shown in Figure 4-17. Each DRACS sensitivity case is color-coded on Figure 4-17. The core power and the DRACS heat removal are dashed and solid lines, respectively. The base case has the maximum DRACS heat removal capacity, which reached ~2.92 MW (i.e., 2920 kW on Figure 4-17). The corresponding heat removals for the 3, 2, and 1 DRACS train cases are 2.46 MW, 1.83 MW, and 1.13 MW. The DRACS responded with increasing efficiency with a decreasing number of trains for 730 kW/train, 820 kW/train, 915 kW/train, and 1130 kW/train for 4, 3, 2, and 1 DRACS trains, respectively. Each successive decrease in available DRACS trains created larger deviations from the design conditions that gave 625 kW per train. While the changing DRACS efficiency is qualitatively consistent with the thermal response of the system, there is not enough design information to assess the quantitative accuracy. Nevertheless, the various results illustrate a range of responses that illustrate degrading conditions. The core power in the 4, 3, 2, and 1 DRACS cases converge on total DRACS heat removal at 25,440 sec (7.1 hr), 25,700 sec (7.1 hr), 28,500 sec (7.9 hr), and 83,300 sec (23.1 hr), respectively.

The 1% damper open calculation includes 4 DRACS trains but the air flow dampers remain at the 1% open position. It is assumed that the dampers for the air flow to the NDHXs did not open on the accident signals. Consequently, the 1% damper case has some heat removal but was relatively small. The total DRACS heat removal settled near 200 kW, or 50 kW per DRACS train. The nominal DRACS heat removal in the 1% damper position was much greater than 1% of the design value, which would be 6.25 kW per train. However, the NDHX heat removal does not scale linearly with the damper position. The velocity and exit temperature of the air on the airside of the NDHX increased well above their nominal values, which contributed to a DRACS heat removal rate of 124 kW (i.e., 31 kW/train) at steady conditions prior to the transient (i.e., 5% of the design heat removal capacity with the damper fully open).

The core power for the damper at 1% position is shown on Figure 4-17, which is nearly identical to the core power in the 1 DRACS train case. In both the 1% damper and 1 DRACS train cases, the core heated enough to shut down the fission reaction, which left only the core decay heat. Sometime after 100,000 sec (27.8 hr), the 1xDRACS case will have a return of the fission power to offset the growing difference between the DRACS heat removal and the decay power. However, the calculation was not extended that far. The core power in the 1xDRACS case is expected to respond similarly to the other DRACS cases but at a delayed time (i.e., >27.7 hr). The 1 DRACS heat removal case exceeded the core power at 83,300 sec (23.1 hr) but will not return to fission until the core cools enough to generate sufficient positive reactivity to offset the prior system heatup.

The peak fuel temperatures for the 5 cases are shown in Figure 4-18. The responses of the 2, 3, and 4 train DRACS cases are approximately identical. There is negligible influence of the number of DRACS trains on initial peak fuel temperature response due to the delay in the DRACS startup. Subsequently, the DRACS system stabilizes relatively to the various core powers (see Figure 4-17).

The system temperatures (i.e., including the fuel temperatures) balance at a condition where the net reactivity is near zero. This implies the long-term temperatures in the core for these three cases will also be similar. Consequently, the long-term maximum fuel temperatures with low fission powers were also similar (~800 K and ultimately tied to generating a net reactivity of 0 $ in the core). Furthermore, the DRACS heat removal matched the core power at about the same timing, which prevented in any successive heat ups or deviations as a function of the DRACS response. The specific long-term peak fuel temperatures were 797 K, 799 K, and 801 K for 2, 3, and 4 trains, respectively. The peak and the long-term peak fuel temperature results showed a large margin to the fluid saturation temperature (1214 K) and the fuel melting temperature (1623 K).

The long-term peak fuel results for no and 1 train DRACS cases showed different behaviors. The heat removal in the 1 train DRACS case was below the core power until 83,300 sec (23.1 hr). Unlike the 2, 3, and 4 train cases, the primary system, the long-term core heat up was not balanced after 25,440 sec to 28,500 sec to a net reactivity of 0 $. Rather, the 1 DRACS response was controlled by the decay heat power. As suggested by the peak fuel temperature response, the 1 DRACS cases is well above the core temperature conditions where the net reactivity will be 0 $. However, it is trending to that condition after 83,300 sec but with a net negative reactivity that is preventing any significant fission power.

The comparison peak fuel temperature of the no DRACS case to the 1 DRACS cases illustrates the benefit of even a single DRACS train. In both cases, the primary system is being heated by the same magnitude of decay heat and no fission power. The slow heatup of the peak fuel temperature illustrates the large thermal mass of the ABTR and the benefits of even a small amount of DRACS heat removal.

The long, sustained heatup in no DRACS case causes an expansion of the sodium such that the hot pool spills over into the cold pool after 63,540 sec (17.7 hr). The fluid starts spill into the cover gas systems at 74,400 sec (20.7 hr) when the vessel fills to the top. The initial peak and the long-term peak fuel temperature results showed a delay in system boiling (1214 K) until after >100,000 sec (27.7 hr). There is no risk of fuel melting (1623 K) until the large hot and cold pools of sodium boil down and uncover the core (i.e., after many days).

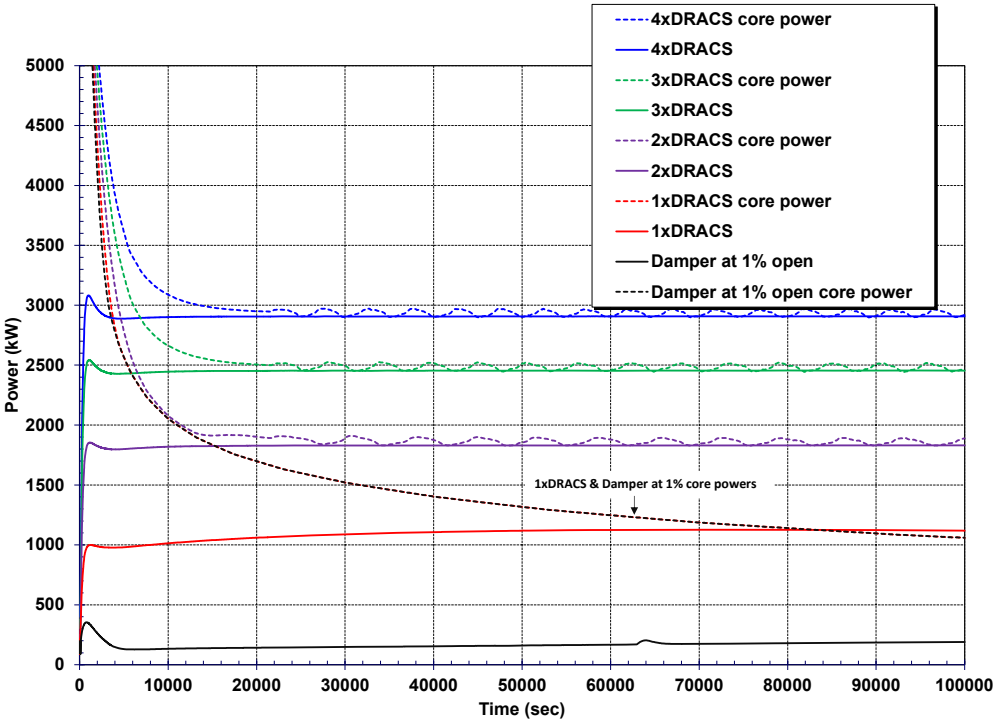

Figure 4-17 Comparison of the core power and DRACS heat removal for the DRACS sensitivity cases.

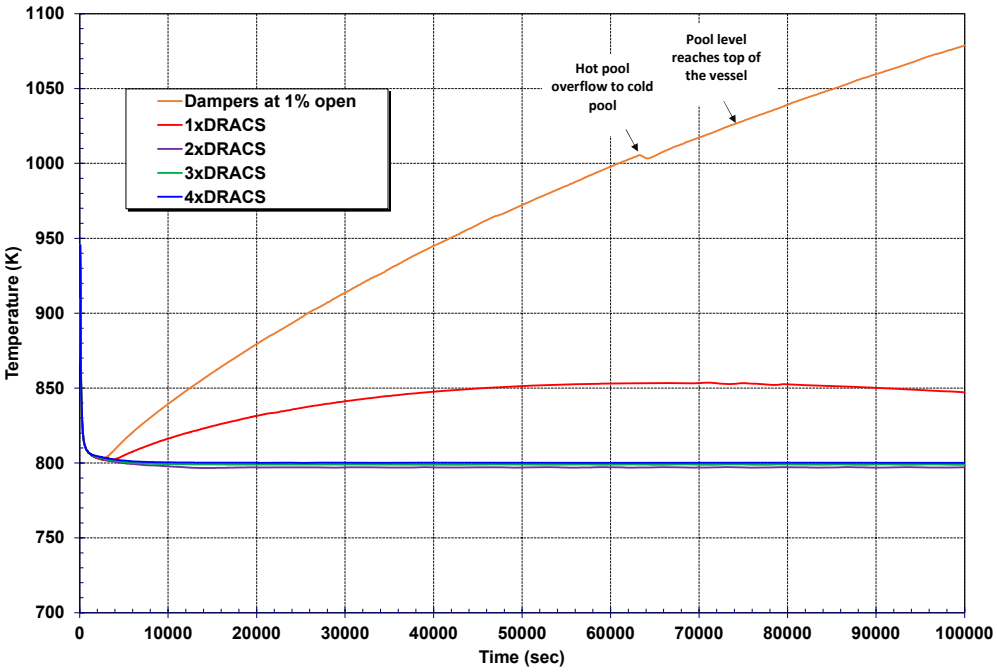

Figure 4-18 Comparison of the peak fuel temperature for the DRACS sensitivity cases (long-term results).

4.3. Single blocked assembly results

The final calculation is a single blocked assembly. Due to the lack of a source term in the other sequences, the blocked assembly sequence was selected to demonstrate the new SFR fuel degradation modeling. The new models related to the fuel degradation in SFR are discussed in Section 2.1. The blocked fuel assembly is initiated with a 100% blockage of the single high-powered assembly in Ring 1 of the core nodalization (see Figure 3-7). The primary and intermediate system pumps remain running. The control assemblies are assumed to start inserting near the beginning of the accident to terminate the fission reaction (see discussion below). The cover gas system at the top of the vessel is assumed to leak into the containment dome.

There were some significant computational problems in the blocked assembly calculation. The complications arose from convergence issues during the complete melting and relocation of the metallic fuel. The difficult physics included the relocation of molten materials into the residual sodium at the bottom of the assembly, reentry of subcooled sodium from the assembly exit, and the radial heating of the interstitial fluid surrounding the affected assembly duct. Several modeling simplifications were applied to allow the calculation to progress, which will be summarized. In retrospect, a separate effects modeling approach of the single assembly would have been a better approach to test the new models without the complications of the response of the remainder of the core and surrounding volumes. The blocked assembly results presented in this report should be considered a preliminary evaluation.

The following modeling simplifications were used to circumvent convergence issues. First, since the interstitial bypass region surrounding the assembly ducts is only 4 mm wide, the base model lumped all the Ring 1 to Ring 7 interstitial space between ducts into a single control volume (i.e., CV-200, not shown on Figure 3-7). The single lumped control volume did not accurately represent the interstitial space adjacent to an overheating blocked assembly. Consequently, a separate control volume for the interstitial space around the blocked assembly was added to better represent the local conditions but this volume had severe convergence problems and the approach was abandoned. The final approach made the outside surface of the blocked duct adiabatic, which avoided the bypass region convergence problems but also neglected the associated heat transfer.

Second, any small leakage into the failed assembly also created computational problems with a continual flow of liquid and vaporizing sodium interacting with heating and relocating molten fuel. Therefore, the inlet was completely blocked, which is possible but likely not credible.

The previous two model modifications created a new problem where the fuel over-heated to non-physically high temperatures. Consequently, some leakage was allowed through the assembly inlet after the fuel melted but not from the top. The initial phase of the accident was characterized with a rapid vaporization of the sodium in the assembly and a rapid pressurization causing the two-phase ejection of the liquid and vapor sodium. The resulting configuration was a voided assembly. However, the liquid sodium could penetrate back into the assembly from the hot pool after the assembly voids, which also caused convergence problems. Consequently, the assembly exit was configured to only allow outflow. The only inflow into blocked assembly was a 0.2% opening at the inlet after 31 seconds (i.e., reached to allow convergence).

The inflow cooled the degraded fuel, which allowed the calculation to progress and evaluate the longer-term transport of the released radionuclides. The timing and rate of the inflow had no significant impact on the radionuclide release, which occurred during the initial fuel degradation. Without a cooling flow, the fuel continued heating and the calculation stopped. While the timing and rate of the inflow was arbitrary, it had a negligible impact on the release radionuclides from the

initial fuel melting. The released radionuclides had already transported to the hot pool above the blocked assembly.

The preliminary calculations did not include a reactor trip. Consequently, the reactor remained at power during the blocked assembly fuel degradation phase. The reactor fission power in the blocked assembly caused non-physically high fuel temperatures. It is unknown what signal might cause the reactor to trip (e.g., a high radiation signal or a pressure instability in the vessel). Furthermore, the ABTR MELCOR model lacked the appropriate feedback and spatial physics for melting and relocating fuel. Consequently, a reactor trip signal was assumed to occur at 6 seconds when the fuel started melting (i.e., primarily to avoid numerical issues). The control assembly started to insert at 6 sec and took 60.5 sec for fully insert.

A number of other changes were needed including equilibrium thermodynamics in the blocked assembly and homogeneous flow to promote complete assembly voiding during the rapid pressurization and liquid expulsion phase.

The modeling changes described above allowed the calculation to proceed through fuel melting, cladding melting and failure, fuel relocation, fission product release, and gradual reflooding. The calculated refrozen and relocated assembly end state is consistent with observations from other metal fuel reactor accidents with inlet blockages (e.g., Fermi-1 [21] or NIST [22]). A primary motivation of the modeling modifications was to illustrate the transport of the released fission product gases into the containment and the environment. Any fission product gases that transported to the gas space at the top of the vessel were vented through the cover gas system and assumed to leak into the containment (see Figure 3-6). However, the non-gaseous fission products were retained in the hot sodium pool above the core (see Section 3.4 and the discussion below for a further explanation). The transient progression is described next.

Following the initiating event that blocked the assembly, the sodium in the assembly began a rapid heatup and began boiling at 3 sec (see Figure 4-19). All the sodium in the assembly had been expelled by 10 sec and only sodium vapor surrounded the fuel. As described above, a slow reflood started at 31 sec to cool the molten fuel, which was iteratively determined as described above.

The fuel cladding temperatures by axial level are shown in Figure 4-20. The fuel cladding is coupled to the fuel through the sodium bond in the gap between the fuel slug and the cladding. The cladding heats the sodium fluid in the assembly duct. The sodium boils at approximately 1170 K, which is a function of the local pressure. The fuel cladding temperatures rapidly ascend to fuel melting temperature (i.e., 1643 K). Due to the high thermal coupling between the cladding and fuel, initially through the sodium bond, the fuel, and the cladding heat together. The fuel melts at 1623 K but is retained by the intact cladding. The fuel melting phase is shown by the temperature plateau at 1623 K. Following the fuel melting, the fuel rod temperature increases to the steel cladding melting temperature (i.e., 1687 K). The cladding melts and candles until it structurally weakens and collapses. The sharp temperature drops indicate the failure of that region of the fuel rod (i.e., 10 axial levels in the active fuel region, see Figure 3-7). Any intact rod sections above a failed location are assumed to collapse into debris at the same time.

The initial collapse occurs at level 5 of the active fuel region[15] at approximately 10 sec. Consequently, level 5 through 10 collapse at the same time. The peak axial power is at level 5, which explains why it

[15] Note, the MELCOR core package nodalization includes 3 axial levels below the start of the axial fuel as shown in Figure 3-7. Consequently, active fuel level 1 corresponds to MELCOR core level 4.

was the first cladding failure location. Active core levels 4, 3, 2, and 1 collapse at 11 sec, 13 sec, 30 sec, and 63 sec, respectively. Consequently, the entire assembly has failed by 63 sec.

Figure 4-21 depicts aspects of the initial fuel degradation. In the lefthand image, the assembly is at the normal full power condition. The fuel is intact and there is no solid or molten debris in the assembly. The middle picture shows 9 seconds after the flow blockage. The fuel is still intact but approaching the fuel melting temperature. The liquid level has dropped to below the bottom of the active fuel. The righthand figure shows the state at 15 sec after the flow blockage. The top 8 active fuel levels have collapsed (i.e., pictorially shown as an empty space in the intact fuel column). The bottom 2 axial fuel levels are intact. Some of the debris is solid and some is molten. The locations of the solid debris are pictorially indicated in the middle column. There is also molten debris supported above the solid debris field. Some molten fuel drained through the bottom of the assembly without freezing.

The fission product release from the blocked fuel assembly is shown in Figure 4-22. The release fractions are based on the whole core inventory. A 100% release fraction for just the blocked assembly is indicated with the dashed line. Essentially all the noble gases (i.e., 97% for the Xe radionuclide class, see Table 3-4 for included elements) are released from the fuel and the fuel pin plenum. A significant portion of the volatile iodine and cesium are also released (5.6% of the blocked assembly inventory). The release fractions of the less volatile radionuclides are also shown but relatively small. The magnitude of the release is influenced by temperature and time. As noted in Section 3.4, there is some information on metal fuel release fraction by temperature but not time. The fuel debris started to cool and quench after 31 sec, which limited the magnitude of the release.

The fission product gas release (i.e., Xe class) is modeled using the new SFR models within the fuel pin and LWR debris field models outside the fuel. The fission product release to the fluid is assumed to start after the fuel melts via a leak in the fuel pin cladding pressure boundary (i.e., >1630 K).

Figure 4-23 shows the xenon (noble gases) distribution after release. The xenon gas bubbles through the hot pool to the argon gas space at the top of the vessel. The fission product gases in the argon gas space vent through the cover gas line and leak into the containment. The argon cover gas flow sweeps nearly all of the released xenon out of the argon gas blanket vessel into the containment. A small amount of the xenon is circulated into the cold pool. The containment leaks at 0.1% volume per day at 68.9 kPa gauge (10 psig). However, the containment has a negligible pressurization from this transient, so the actual leakage is <<0.1% volume per day. Consequently, the xenon release fraction to the environment is very small ($5x10^{-7}$ at 6900 sec) at the end of the calculation.

Figure 4-24 shows the cesium/iodine distribution after its release. Both cesium and iodine are assumed to form non-gaseous compounds that are retained in the hot pool. Consequently, there is no transport to the vessel argon gas layer, the containment, or the environment. Complete retention of the volatile fission products in the liquid sodium may be nonconservative. Alternate behaviors could be explored further using the MELCOR GRTR model using a liquid sodium database with a Gibbs free energy minimization (GEM) solver. MELCOR uses the Thermochimica GEM solver and database information to calculate the radionuclide chemical forms, vapor pressures, and solubilities [23]. Sodium iodide is a possible chemical form of iodine. However, the development of a sodium thermochemical database for radionuclide source terms is incomplete and lacking data [24]. Consequently, there is limited information to guide exploratory modeling. As more information is collected, GRTR could be used for identified volatile chemical compounds with Antione vapor pressure and solubility correlations in lieu of a developed thermochemical database.

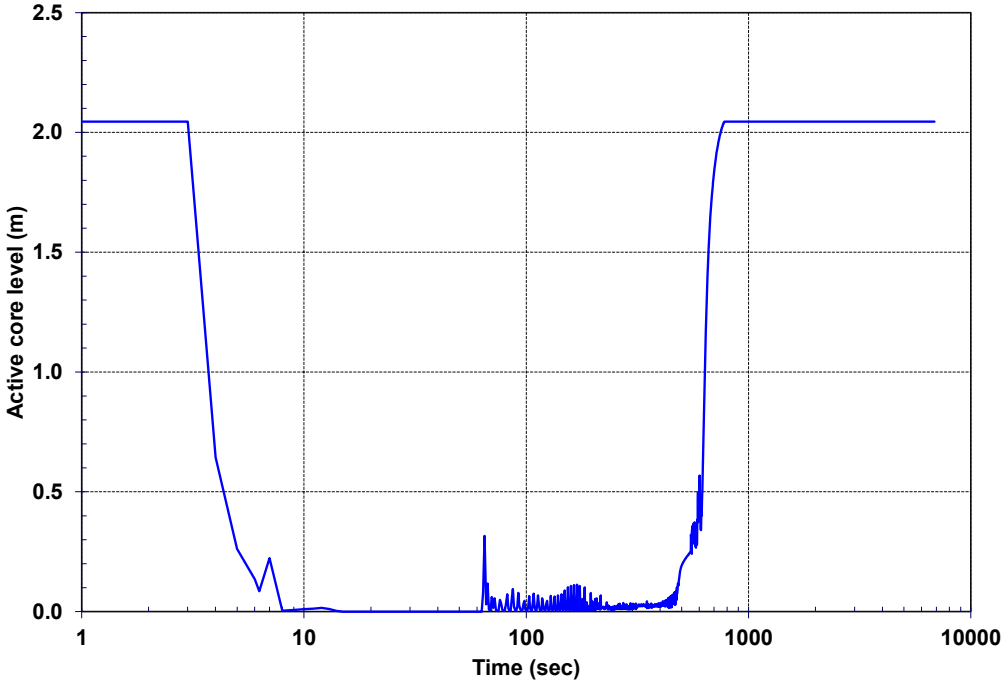

Figure 4-19 Blocked assembly liquid sodium level.

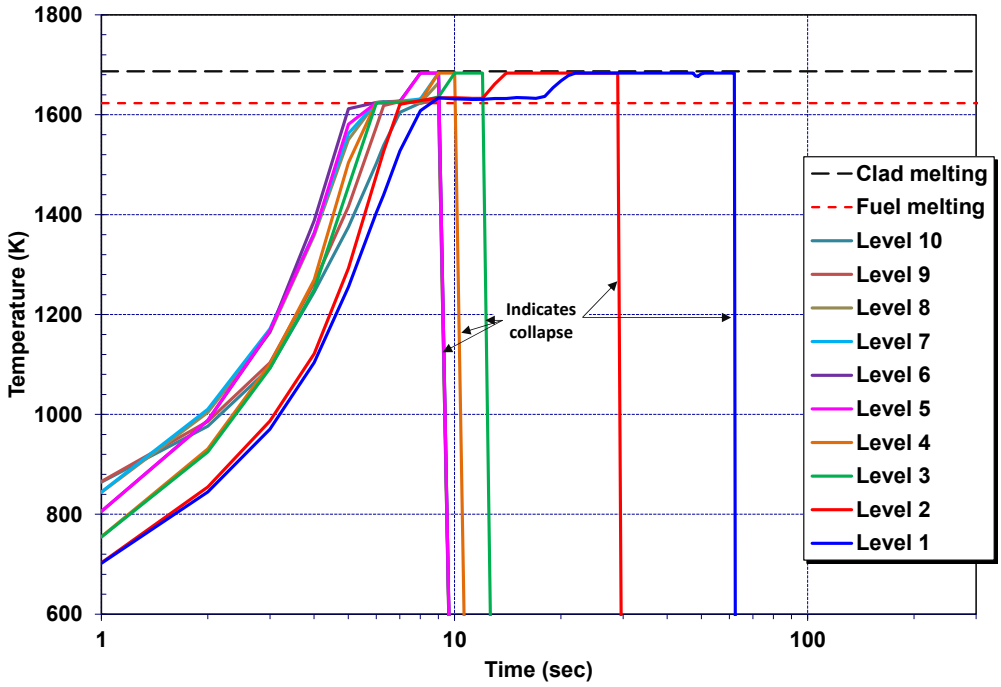

Figure 4-20 Blocked assembly fuel cladding temperatures.

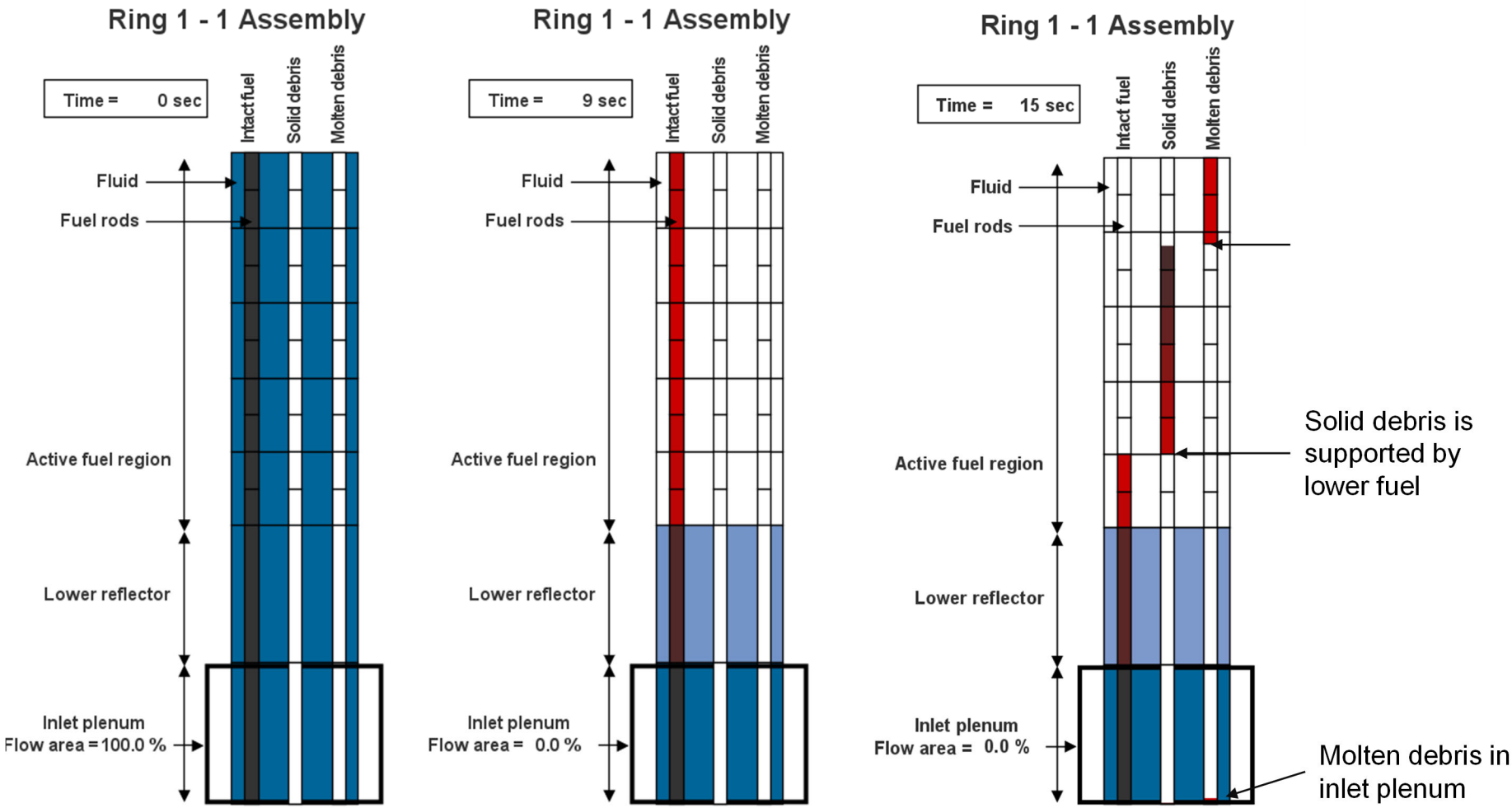

Figure 4-21 Blocked assembly fuel degradation illustrations.[16]

[16] The fuel degradation illustrations are from the Symbolic Nuclear Analysis Package (SNAP) graphical animation program. The colors of the fuel and fluid regions vary according to their temperature. A brighter red fuel or debris color is hotter than a darker color.

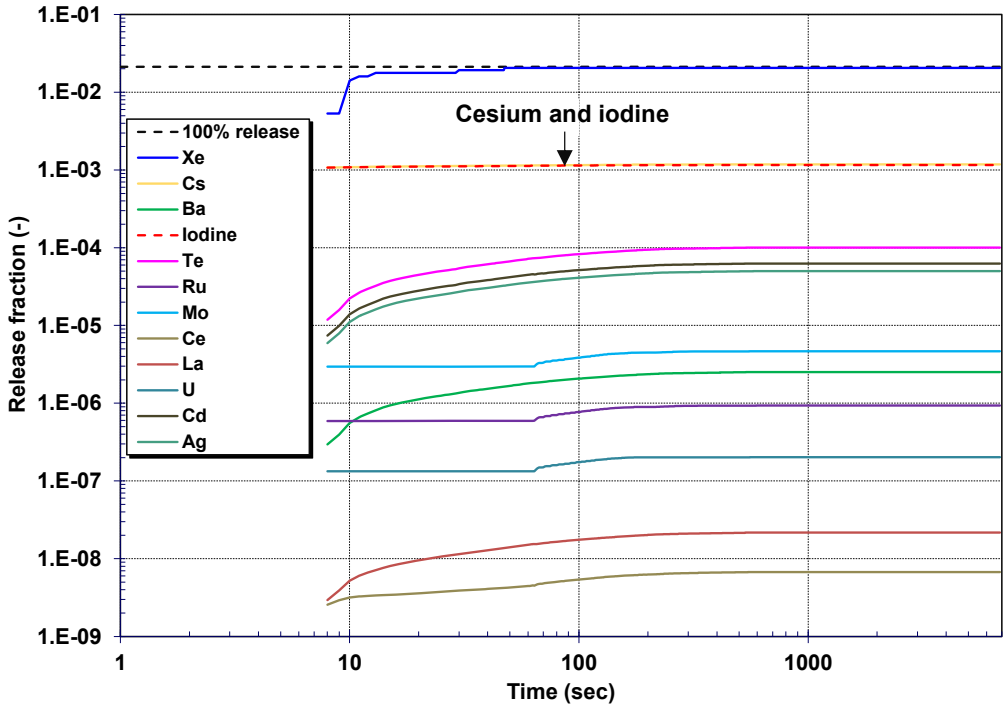

Figure 4-22 Radionuclide release faction from the fuel based on the whole core inventory.

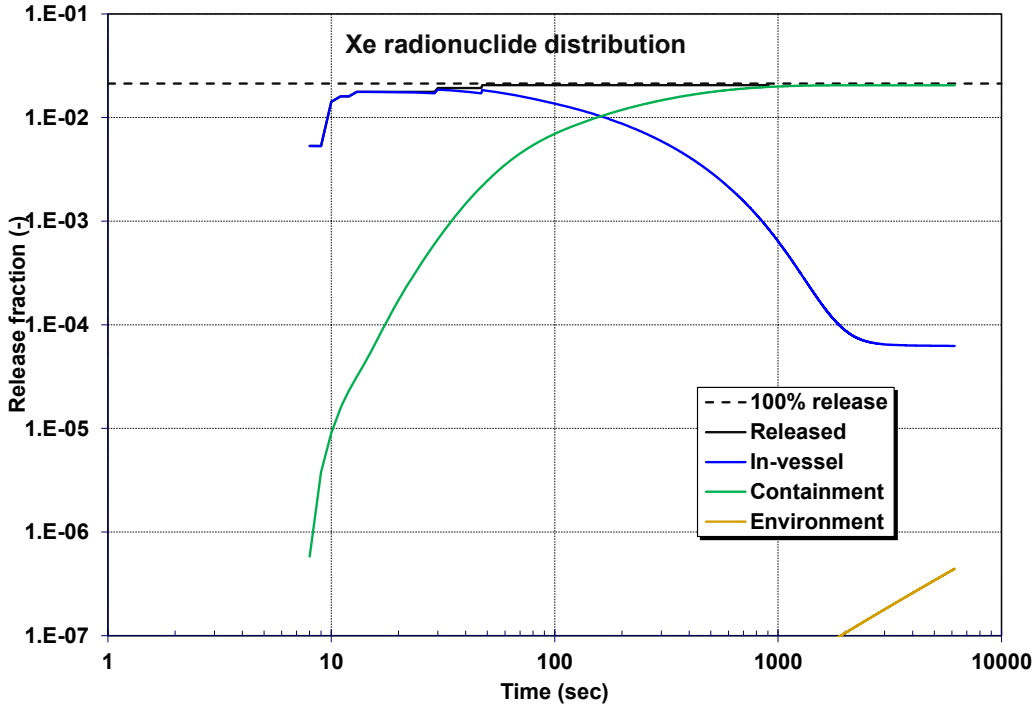

Figure 4-23 Xe radionuclide class distribution.

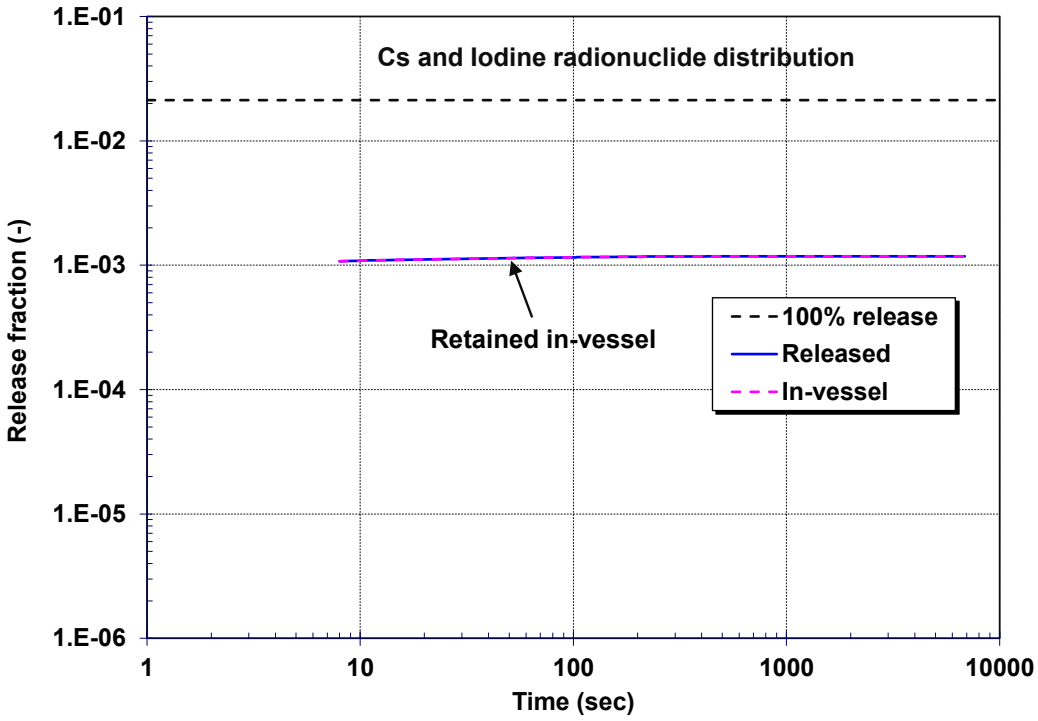

Figure 4-24 Cesium and iodine radionuclide class distribution.[17]

[17] The cesium and iodine responses were essentially identical so just one curve is shown on the figure.

This page left blank

5. SUMMARY

The MELCOR code has been updated to support NRC safety evaluations of accidents in SFRs. This report presents demonstration calculations for a ABTR SFR. A MELCOR model of the ABTR was developed that included the vessel, the in-vessel sodium circulation system, the intermediate heat exchangers (iHXs), the intermediate loop interface to iHXs, the three loop DRACS passive safety system, the reactor guard vessel, the reactor cavity, and the containment. The SCALE results for the radionuclide inventory and decay heat were incorporated. SCALE also provided the axial and radial power, and the core reactivity feedbacks.

The ABTR input model was used to demonstrate the UTOP, the ULOF, and single blocked assembly sequences. UTOP scenario sensitivity calculations were performed to illustrate the impact of larger reactivity insertions and the role of the intermediate loop heat removal. ULOF sensitivity calculations were performed that varied the number of DRACS trains available for heat removal. Finally, a single blocked assembly calculation was performed that included fuel melting, cladding failure, fuel relocation, and fission product release, and fission product gas transport to the environment. The analyses demonstrate the flexible capabilities of MELCOR to evaluate the accident progression in an SFR. The code can also incorporate evolving data from ongoing research programs and includes flexible inputs for sensitivity and Monte Carlo sampling on uncertain parameters.

This page left blank

REFERENCES

[1] "Nuclear Energy Innovation and Modernization Act," Public Law No: 115-439, January 2019.

[2] "Non-LWR Vision and Strategy Near-Term Implementation Action Plans," Nuclear Regulatory Commission, ADAMS Accession No. ML16334A495, 2019.

[3] Humphries, L. L., et al., MELCOR Computer Code Manuals: Volume 1; Reference Manual - Version 2.2.18019, Sandia National Laboratories, SAND2019-13442, Jan 2021.

[4] Y.I. Chang, P.J. Finck, and C. Grandy, "Advanced Burner Test Reactor Preconceptual Design Report", ANL-ABR-1 (ANL-AFCI-173), 2006.

[5] "Non-Light Water Reactor (Non-LWR) Vision and Strategy, Volume 3 – Computer Code Development Plans for Severe Accident Progression, Source Term, and Consequence Analysis" NRC ADAMS Accession No. ML20030A178, Revision 1, January 31, 2020.

[6] A. Shaw, F. Bostelmann, W. A. Wieselquist, "Application of SCALE to Sodium Fast Reactor in Support of Severe Accident Analyses," ORNL/TM-2022/2758, February 2023, Oak Ridge National Laboratory, Oak Ridge, TN.

[7] Wagner, K., et al., "MELCOR Accident Progression and Source Term Demonstration Calculations for a Heat Pipe Reactor," Sandia National Laboratories, SAND2022-2745, March 2022, https://www.osti.gov/biblio/1854082.

[8] Wagner, K., et al., "MELCOR Accident Progression and Source Term Demonstration Calculations for a Heat Pipe Reactor," Sandia National Laboratories, SAND2022-2745, March 2022, https://www.osti.gov/biblio/1854083.

[9] Wagner, K., et al., "MELCOR Accident Progression and Source Term Demonstration Calculations for a FHR," Sandia National Laboratories, SAND2022-2751, March 2022, https://www.osti.gov/biblio/1854081.

[10] Wagner, K., et al., "MELCOR Accident Progression and Source Term Demonstration Calculations for a Molten Salt Reactor," Sandia National Laboratories, SAND2023-01803, April 2023.

[11] B. Rearden and M. Jessee, "SCALE Code System, ORNL/TM-2005/39, Version 6.2.3," UT-Battelle, LLC, Oak Ridge National Laboratory, 2018.

[12] "SCALE/MELCOR Non-LWR Source Term Demonstration Project –Sodium Fast Reactor (SFR)," NRC Adams Ascension Number ML22189A173, https://www.nrc.gov/docs/ML2235/ML22353A109.pdf, September 13, 2022.

[13] Tsai, S.S, "The NACOM Code for Analysis of Postulated Sodium Spray Fires in LMFBRs," NUREG/CR-1405, Brookhaven National Laboratory, Upton, New York, March 1980.

[14] Louie, D. L. Y., and M. Aoyagi, *Sodium Fire Collaborative Study Progress–CNWG Fiscal Year 2020*, SAND2021-0136, Sandia National Laboratories, Albuquerque, NM, January 2021.

[15] Louie, D. L. Y., and M. Aoyagi, Sodium Fire Collaborative Study Progress–CNWG Fiscal Year 2021, SAND2021-015469, Sandia National Laboratories, Albuquerque, NM, December 2021.

[16] C. F. Boyd and K. W. Armstrong. "Computational Fluid Dynamics Analysis of Natural Circulation Flows in a Pressurized Water Reactor Loop under Severe Accident Conditions," NUREG 1922, U.S. Nuclear Regulatory Commission, Washington, DC. March 2010.

[17] Louie, D. L., Humphries, L. L., "NSRD-10: Leak Path Factor Guidance Using MELCOR," Sandia National Laboratories, SAND2017-3200, March 2017.

[18] ASHRAE, "Handbook of Fundamentals," American Society of Heating, Refrigerating and Air-Conditioning Engineers, Inc, 1997.

[19] D. Grabaskas, M. Bucknor, and J. Jerden "Regulatory Technology Development Plan Sodium Fast Reactor Mechanistic Source Term – Metal Fuel Radionuclide Release," ANL-ART-38, Argonne National Laboratory, February 2016.

[20] El-Genk, M. S., and Tournier, J. P., "A Point Kinetics Model for Dynamic Simulations of Next Generation Nuclear Reactor," Progress in Nuclear Energy, Volume 92, September 2016, pp. 91-103.

[21] "Report On The Enrico Fermi - Fuel Melting Incident The Atomic Power Plant On October 5, 1966," Atomic Power Development Associates, Inc., APDA-233, December 15, 1968, https://doi.org/10.2172/4766757.

[22] T. Mason, LANL, ltr. to NIST Director tor J. K. Olthoff, "Unplanned Shutdown of the NIST Reactor, February 3, 2021," DIR 22-035, February 14, 2022, https://www.nist.gov/system/files/documents/2022/08/02/T.%20Mason%20Report%20on%20NCNR_2022.pdf.

[23] M.H.A. Piro, S. Simunovic, and T.M. Besmann, "Thermochimica User Manual v1.0," ORNL/TM-2012/576, Oak Ridge National Laboratory, December 2012.

[24] J. Jerden, D. Grabaskas, M. Bucknor "Development of a Thermochemical Database for Sodium Fast Reactor Mechanistic Source Term Calculations," Argonne National Laboratory, American Nuclear Society Annual Meeting June 9-13, 2019, Minneapolis, MN USA, Conference Paper Manuscript APT 151078, https://www.osti.gov/servlets/purl/1785319.

DISTRIBUTION

Email—Internal

Name	Org.	Sandia Email Address
David Luxat	08852	dlluxat@sandia.gov
Brad Beeny	08852	babeeny@sandia.gov
Technical Library	01911	sanddocs@sandia.gov

Email—External (encrypt for OUO)

Name	Company Email Address	Company Name
Jason Schaperow	jason.schaperow@nrc.gov	NRC
Hossein Esmaili	hossein.esmaili@nrc.gov	NRC
Shawn Campbell	Shawn.campbell@nrc.gov	NRC

Hardcopy—Internal

Number of Copies	Name	Org.	Mailstop

This page left blank

This page left blank

Sandia National Laboratories

Sandia National Laboratories is a multimission laboratory managed and operated by National Technology & Engineering Solutions of Sandia LLC, a wholly owned subsidiary of Honeywell International Inc. for the U.S. Department of Energy's National Nuclear Security Administration under contract DE-NA0003525.